

UNIVERSITÀ DEGLI STUDI DI NAPOLI
FEDERICO II



DOTTORATO DI RICERCA IN FISICA

CICLO XXXI

COORDINATORE: PROF. SALVATORE CAPOZZIELLO

**Innovative detection methods for
radiation hardness**

SETTORE SCIENTIFICO DISCIPLINARE FIS/04

Dottorando:
Pierluigi CASOLARO

Supervisore:
Dr. Luigi CAMPAJOLA

2015/2018

Contents

Introduction	1
1 Radiation hardness	5
1.1 Space radiation environment	6
1.1.1 Trapped particles	6
1.1.2 Galactic cosmic rays	10
1.1.3 Solar cosmic rays and solar particle events	12
1.2 Interaction of radiation with matter	13
1.3 Radiation effects on electronic devices	17
1.3.1 Total ionizing and displacement damage dose	17
1.3.2 Single event effects	22
1.4 Neutron damage	25
2 Radiation sources and dosimetry	29
2.1 International standards	30
2.2 Gamma sources	31
2.3 Dosimetry for gamma and X radiation	32
2.4 Particle accelerators	35
2.5 Charged particles detectors	40
2.6 Techniques of dosimetry monitoring on the DUT	42
2.7 Rutherford Backscattering Spectroscopy	45
2.8 Neutron sources	47
2.9 Neutron detection	52
3 Radiochromic films	58
3.1 Historical background	58
3.2 Operating principle	59
3.3 Dependence on radiation type, energy and dose rate	60
3.4 Types of films and related applications	60
3.5 Film reading and calibration	62
3.6 Response of EBT3 Gafchromic films to more radiation types	64
3.7 Absolute dosimetry with radiochromic films	69
3.8 An innovative radiation source for TID tests	71
4 Real-time dosimetry with radiochromic films	77
4.1 Motivations	77
4.2 Optical-fiber-based setup	78
4.3 Dose calibration	81
4.3.1 Uncertainty analysis	81
4.3.2 EBT3 Gafchromic films	82

4.3.3	XR-QA2 Gafchromic films	84
4.4	Discussion and outlook	85
5	Innovative neutron detector	89
5.1	Introduction	90
5.2	Preliminary characterization and measurements	90
5.3	Characterization with gamma radiation	91
5.4	Calibration of the PS scintillator	94
5.5	Pulse height spectra for charged particles	95
5.6	Charge comparison method	96
5.7	Test with Am-Be neutron source	100
6	Fast neutron production	102
6.1	The ${}^7\text{Li}(p,n){}^7\text{Be}$ reaction	102
6.2	Neutron production at LNS tandem accelerator	105
6.3	Neutron production at IBA 18/18 medical cyclotron	107
	Conclusion	113
	Bibliography	115

Introduction

The interaction of radiation with matter is one of the fields of physics with more implications on both fundamental and applied physics. The understanding of problems of interaction of radiation with matter is on the basis of crucial aspects of nuclear physics, high-energy physics, astrophysics as well as design of new particle detectors, photon and ion therapy, study of radiation damage, among the others. One of these fields where the interaction of radiation with matter is strongly present in many aspects is the radiation hardness. We refer to radiation hardness as the set of studies of radiation-induced damage on electronic devices, definition of risky environments, evaluation of radiation doses to which the electronic devices are exposed and accomplishment of radiation tests for studies of device's response to radiation. It is well known in fact that relatively high levels of radiation affect the properties of electronic devices. As the number of electronic components employed in the applications increase, it is clear that radiation hardness is a field of fundamental importance. As an example, the space radiation environment is a hazard for electronic components and in general for all the equipment travelling in space. The performances of space systems such as electronic units, sensors, communication units and optical and opto-electronic systems are determined by the proper functioning of electronics. Such systems are highly sensitive to space radiation. Moreover, radiation accelerates the aging of devices and materials. Other environments with radiation levels sufficiently high to be a hazard for electronics are the facilities for experiment of nuclear and high-energy physics and irradiation facilities in general such as particle accelerators and nuclear reactors. Radiation hardness studies are crucial also for electronic instrumentation and equipment used in particle and photon accelerators for applications of medical physics such as radiotherapy and hadrontherapy. The damage of electronic components employed in avionic applications is a well-known topic for over twenty years. This damage is induced by neutrons present at flight altitudes. These neutrons are generated by interaction of cosmic rays with neutral atmosphere. Finally, a very recent application concerns the neutron-induced damage at sea level on critical sensitive electronic components such as power-electronics and CMOS in pace-makers applications. Although the flux of such neutrons is less than neutron flux at flight altitudes, it is a concern for such systems. A single interaction of a MeV-energy neutron with electronics can cause the definitive breakdown of the device. An approach to overcome these problematic consists in the employment of more than one electronic component so that if one fails it can substituted by another. Of course this approach (redundancy) is costly and therefore not always acceptable. The electronic components are generally tested to one or more damage induced by radiation including Total Ionizing Dose (TID), Displacement Damage Dose (DDD) and Single Event Effect (SEE). The characterization of radiation hardness properties of such electronic components is performed at irradiation facilities by exposing the device under test to radiation of

well-defined characteristic. For example, for space applications, there are models allowing the prediction of the dose delivered to electronic components during the space mission. Such models can calculate also the concentration of radiation as a function of the incident type. In order to reproduce the effects of radiation on electronics, the tests at irradiation facilities are performed with radiation of different characteristics in terms of type, dose, energy etc. This poses the problem that it is not possible to use standard methods for ensuring the delivery of the correct radiation on the device. In order to setting up reliable radiation detection techniques each situation must be analyzed in detail. This work collects these demands by proposing the design, development and accomplishment of cutting-edge technologies of radiation detection for radiation hardness applications. In particular, a significant part of this work focuses on radiochromic films. These dosimeters, intensively employed in medical physics, find application in radiation hardness for their appealing properties. In particular, radiochromic films are sensitive to X, gamma and charged particles with doses in the range from 10^{-3} Gy to 10^5 Gy; other important properties are the excellent spatial resolution, the easy-handling and data analysis, the sub-millimetre dimensions, the absence of electronics sensitive to radiation and the low cost. Radiochromic films are radiation-sensitive materials showing increasing darkness with increasing radiation dose. The level of darkness of the films is quantified by means of suited physical quantities and a calibration can be established. We studied in depth the properties of radiochromic films and more specifically we studied the response of a set of films to many radiation types of interest in radiation hardness. To do this we exposed a set of films to 250 KV_p X-, ⁶⁰Co gamma- and ⁹⁰Sr/⁹⁰Y beta-rays, 1 MeV electrons and 23, 50 and 200 MeV protons. For each exposure we carried out cross-checking dosimetry measurements. We found that the response of radiochromic films to radiation is independent of the incident radiation type, energy and dose rate. This result, published in a dedicated paper and discussed in chapter 3, is very important for applications such as the radiation hardness. It allows the use of the same type of films for exposures to radiation of different characteristics. Moreover, we carried out the calibration of the films with the law that describe the phenomenon of the kinetics of chemical reactions and more specifically the phenomenon of film darkening. We found the fundamental result that dosimetry with radiochromic film is absolute dosimetry. This result is definitely new, to our knowledge, compared to the extensive literature on radiochromic films. It is noteworthy that the calibrations are usually reported as polynomial fits functions. These characteristics, together with all the well-established characteristics of radiochromic films, made this dosimeter a perfect tool for accurate dose assessment in many radiation hardness tests. An intrinsic limitation of radiochromic films consists in the impossibility of performing real-time dosimetry with standard reading methods, namely commercial scanners and densitometers. For this reason we designed and developed a new radiochromic films real-time method based on opto-electronic instrumentation. This method allows also the exploitation of all the potential of radiochromic films. In fact it was demonstrated that, by using the innovative reading method, it is possible to extend the dynamic range of some types of radiochromic films by more than one order of magnitude. Owing to the wide employment of radiochromic films in the applications, to the potential diffusion on the market, this invention was patented with a National Patent filed in January 2018.

As above mentioned, the irradiations performed for radiation hardness are specific ones (cannot be standardized) and in many cases the demanded information is got by means of more than one detection method. In this thesis we discuss techniques designed and set-up by our research group. One of these has been accomplished for the first time at tandem accelerator of University of Napoli. This high-precision technique is based on the *Rutherford Backscattering Spectroscopy* (RBS) and allows real-time monitoring of the fluence on the device under test. The mentioned detection techniques are to X, gamma and charged particle radiation. The development of new detection systems for fast neutrons represents a separate chapter for the intrinsic difficulties of the interaction of neutron with matter. Moreover, the problem of neutron detection, differently from other radiation types, is strictly related to that of neutron production. The neutron-induced-damage on electronics is well-established. Nowadays the interest of scientific community to neutrons is aimed at many fields of applied and fundamental physics. These necessities prompted the researchers in the last few years to study and develop new kinds of neutron detectors and in particular detectors sensitive to fast neutrons. Polysiloxane-based scintillators, belonging to the class of plastic scintillators such as polyviniltoluene and polystyrene, are promising for work in harsh environment. These detectors have the advantage over the traditional plastics of the non-toxicity and of an enhanced resistance to radiation. We studied in depth the properties of a sample of polysiloxane-based neutron scintillator, by carrying out a full characterization of this detector. Since the detector is new, the gamma calibration was carried out by comparing the response of the detector to that of a well-known inorganic scintillator such as the NaI scintillator. The characterization in laboratory was completed by studying the response to charged particles and by performing Pulse Shape Discrimination (PSD). Finally a first evaluation of the detector efficiency with an Am-Be radioactive source was done. After these preliminary and necessary operations, the new scintillator was used for the characterization of neutron beams generated at two charged particles accelerator, namely the tandem accelerator of Laboratori Nazionali del Sud (LNS) in Catania and the IBA 18/18 medical cyclotron of university of Bern. It has to be said that, owing to the increasing demand in neutron applications, it is of great interest to exploit the existing particle beam facilities to accelerator-based neutron sources. On this line we are currently working at neutron production at these facilities with the aim of producing well-characterized quasi-monoenergetic and atmospheric-like fast neutron beams. The first result of neutron production will be reported in this thesis. The technique that we have studied and designed uses a lithium target and exploits the reaction ${}^7\text{Li}(p,n){}^7\text{Be}$. In order to predict the neutron spectra, we made FLUKA simulations which indicate that quasi-mono-energetic MeV neutron spectra can be accomplished by exposing a few mm thick lithium target to incident protons of energy from tens to hundreds of MeV. The output neutron spectrum involves a well-defined peak near the energy of the incident beam, other peaks corresponding to excited states of ${}^7\text{Be}$ and the contribution due to break-up reactions such as ${}^7\text{Li}(p,n){}^3\text{He}{}^4\text{He}$. The most interesting feature of this method relies in performing precise measurements of the forward neutron flux. This last can be measured from the decay of ${}^7\text{Be}$ (53 d) that emits a gamma-ray of 477 keV (easily measured by means of e.g. a HPGe detector). The characterized poly-siloxane detector is used as on-line cross-check detector. Future studies are devoted to the

determination of the efficiency of the scintillator at different energies by means of the associated-particle-technique (APT). It consists in performing a reaction like the ${}^2\text{H}({}^2\text{H},n){}^3\text{He}$ at different energies. Since the energy of produced neutrons is determined by kinematics as a function of the angle, the APT uses the counts recorded by a silicon detector in backscattering for measuring the scintillator efficiency.

Chapter 1 is meant as review of some aspects of radiation hardness. Since in this thesis the interest focuses on development of detection technologies mainly for spatial and atmospheric radiation hardness, these environments are briefly discussed. Simulations of typical spatial missions were performed with the aim of showing typical requirements for radiation tests, in terms of radiation types and values of integrated fluences. Controversies in the models due to the lack of a vast set of experimental data are highlighted. As a result, it is clear that there is need for new measurements. The interaction of radiation with matter is critically analyzed from the point of view of fundamental physics. These knowledge are the basis for the understanding of basic mechanisms of radiation damage on devices. The last section of the first chapter deals with the damage to electronic devices due to atmospheric neutrons both at flight altitudes and sea level.

Chapter 2 presents the aspects related to radiation tests, by discussing in first section the requirements (radiation type, dose, field uniformity) from International Standards. Successively the commonly employed techniques and radiation sources are shown for X/gamma and charged particle radiation. The detection techniques developed and employed by our research group for dose assessment in radiation hardness tests are discussed by focusing on the new dosimetry method based on RBS. Finally the methods used for production of neutrons (from radioactive sources, reactors and charged-particle-based facilities) are discussed. It is clear that in order to meet the requirements from neutron radiation hardness, further well-characterized neutron sources providing mono- quasi-monoenergetic and atmospheric-like neutron spectra are needed.

Chapter 3 and 4 present the above-discussed dosimetry with radiochromic films, by focusing on the works and results that we have obtained: independence of radiation type, energy and dose-rate of a type of film; determination of the equation that describe the phenomenon of radiation-induced darkening of the film, namely the absolute dosimetry with radiochromic films. These results were of crucial importance for performing a full dosimetry characterization of a ${}^{90}\text{Sr}/{}^{90}\text{Y}$ beta source. This source was recently proposed as irradiation source for TID tests alternative to the standard ${}^{60}\text{Co}$ source. It has several important advantages. Finally the real-time reading system with radiochromic films is discussed in depth.

Chapter 5 presents in detail the characterization of the new neutron scintillator in terms of calibration to gamma radiation, response to charged particle and PSD capabilities.

Chapter 1

Radiation hardness

In the last years the intense employment of critical electronic components in many fields of research, industry and medicine, among the others, pushed physicists and engineers to study in detail the radiation damage on materials and more specifically on electronics. The performances of detectors and electronics employed in basic research, of satellites and spacecrafts for space applications as well as of instrumentation for patients irradiation in cancer therapy are determined by the correct operation of electronic sensitive components. The properties of such components are affected by radiation. The interaction of ionizing radiation with the atoms of the crystal lattice of an electronic circuit can lead to several unwanted effects such as electronic noise, signal spikes, failure of electronic devices and ultimately total breakdown. In order to limit or at least to keep as much as possible under control the radiation damages on such sensitive systems, these components must be characterized as radiation hardened or radiation tolerant. In order to reproduce the effects of the actual space and atmosphere radiation environment, electronic devices are tested at radiation facilities to one or more possible effects caused by radiation. These effects are the Total Ionizing Dose (TID), Displacement Damage Dose (DDD) and Single Event Effect (SEE).

The sources of ionizing radiation that can cause damage on electronics are manifold. Since we focus on the radiation environment of space and atmosphere, the first section of this chapter is meant to give a brief overview of these environments, while more details can be found in the referenced works. The complexity of the problem is highlighted by means of practical examples (e.g. simulations of typical spatial missions) which show the variety of the characteristics of radiation in such environments in terms of flux, energy and radiation type. It is noteworthy that the prediction models typically employed for determining the amount and type of radiation in space are in some cases affected by significantly high uncertainties. As a result, there is a strong need for experimental data in the field of space radiation.

Section 1.2 discusses the interaction of radiation with matter in terms of the effects of radiation on silicon devices. Fundamental physical quantities such as the stopping power and the non-ionizing energy loss (NIEL) are introduced by pointing out to unsolved problems and to the lack of experimental measurements that imply further scientific insights. The knowledge of the basics of interaction radiation-matter is necessary for the understanding of the radiation effects (TID, DDD and SEE) on electronic devices. These aspects are discussed in section 1.3. Finally, section 1.4 presents the neutron-induced effects on electronics. Neutrons are created by interaction of cosmic rays with the Earth atmosphere. Although the neutron flux at commercial flight altitudes and at sea level is less than the flux of radiation in space,

recently it was ascertained that neutrons are a concern for electronics employed in avionics applications and even for critical electronic components at sea level.

1.1 Space radiation environment

The space environment is made of several radiation types, energies and dose rates. Protons, electrons, gamma rays and heavy ions, each one with a broad energy spectrum are the main types in the space around Earth. Such radiation is not homogeneously distributed in space. In fact the concentration and type of radiation in space strongly depends on the space location and on the duration of the space mission. For a spacecraft or satellite in a particular orbit, characteristics of the orbit such as altitude, latitude, longitude and angle of inclination as well as the shielding employed are parameters that must be taken into account for a correct evaluation of the dose. Moreover, external space environmental conditions like magnetic storms and recent solar activities have a significant impact on the variation of concentration of radiation levels. The main components of radiation in the space are classified as follows:

- Particles trapped in the Van Allen belts
- Galactic (and extra-galactic) cosmic rays
- Solar cosmic rays.

These components are briefly discussed in the next subsections.

1.1.1 Trapped particles

Charged particles such as electrons and protons travelling close to Earth can be trapped by the Earth magnetic field. Most of these particles originate from the solar wind and other from the decay of neutrons produced by cosmic ray interactions with the neutral atmosphere. The motion of particles trapped by the Earth magnetic field lines leads to the formation of two main toroidal-shape belts (inner and outer belts). These belts were first discovered by Van Allen and colleagues in 1958 and for this reason they are called Van Allen Belts (Allen, 1958). Figure 1.1 shows the Van Allen Belts with the field lines of magnetosphere, the last approximated by a giant magnetic dipole located in the centre of Earth and inclined of 11.3 degrees with respect to the rotation axis.

Sometimes other belts can be temporarily formed.

The inner belt

The inner radiation belt extends from about 1000 to 6000 km, although the inner boundary can extend up to 200 km when the solar activity is significantly strong. This belt is populated by protons of energy up to some hundreds of MeV and electrons from tens of keV to some MeV. The spectrum of these particles strongly depends on several factors including the altitude and inclination of the orbit. For example,

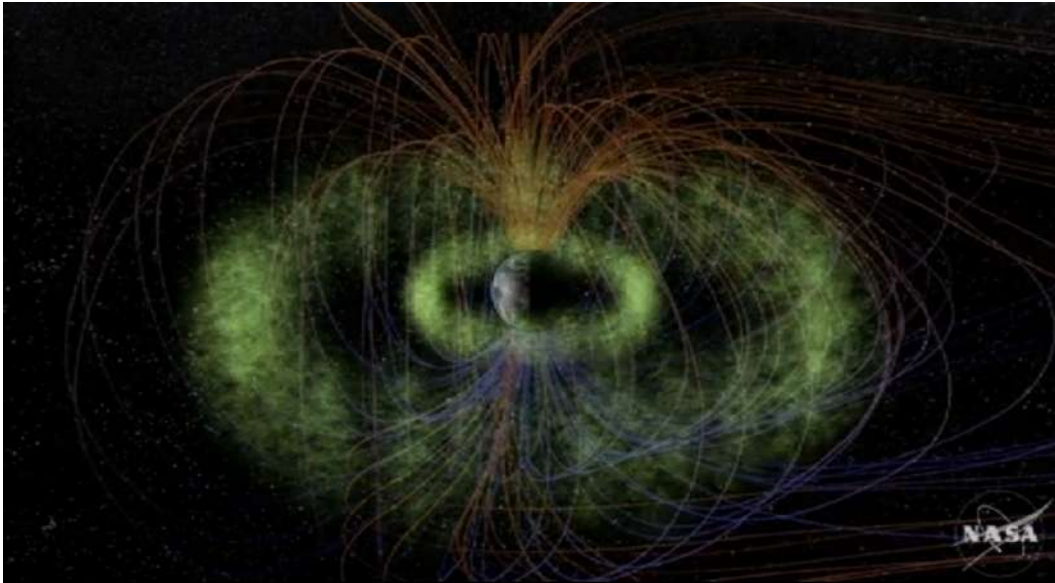


FIGURE 1.1: Screen capture from NASA web site showing a graphic animation of the Van Allen Radiation Belts. The Earth's magnetic field lines and the location of radiation belts are highlighted in figure.

figure 1.2 and 1.3 show the spectra of protons and electrons respectively for a 10-years mission in a 560 km altitude and 26 degrees inclination angle Low Earth Orbit (LEO).

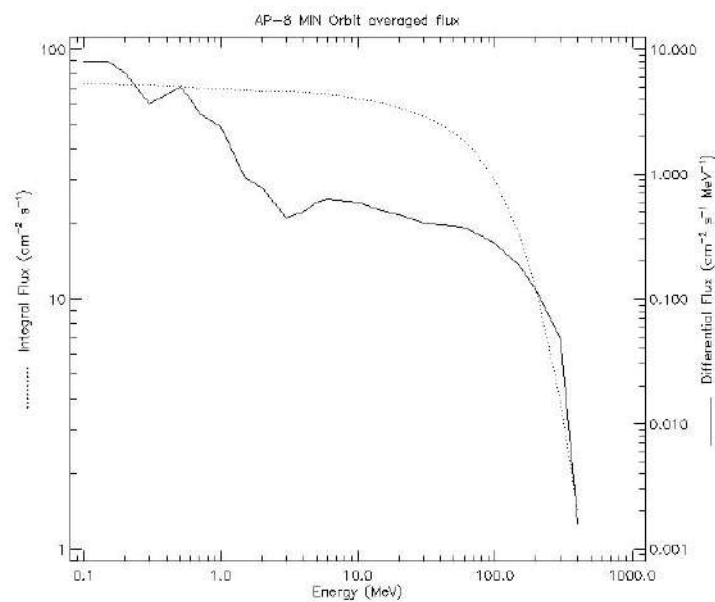


FIGURE 1.2: Trapped proton spectrum for a 560 km altitude and 26 degrees inclination angle orbit. The duration of the simulated mission is 10 years.

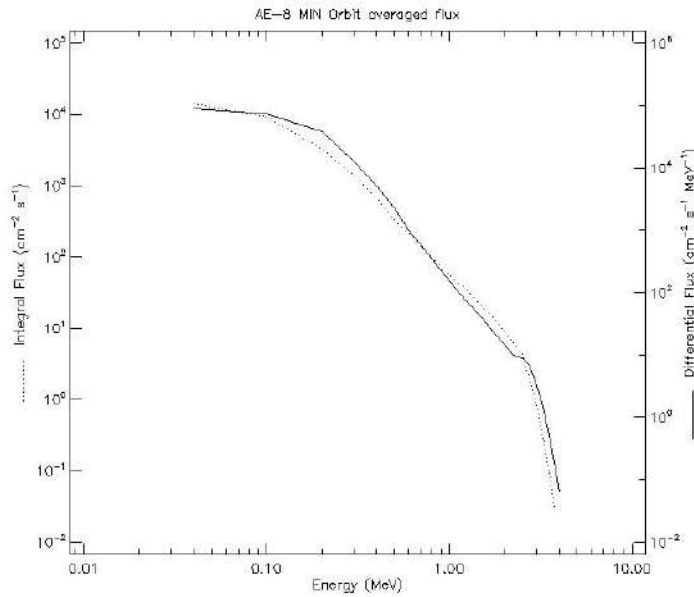


FIGURE 1.3: Trapped electron spectrum for a 560 km altitude and 26 degrees inclination angle orbit. The duration of the simulated mission is 10 years.

Electrons up to few MeV and mainly protons up to 300 MeV represent a hazard that must be taken into account for space missions in the orbit considered in this simulation.

The outer belt

The outer belt is more dynamic than the inner belt, being much more influenced by solar activity and geomagnetic storms. It is mainly populated by electrons in the energy range 0.1-10 MeV and extends from about 13000 to 60000 km altitudes. Figure 1.4 and 1.5 show the spectra of protons and electrons respectively for a 10-years mission in a 36000 km altitude and 0 degrees inclination angle geostationary orbit (GEO).

In this simulation, the proton contribution is dominant in the range from 100 keV up to 2 MeV with a relatively high flux of electrons in the range from 10 keV to few MeV.

Trapped radiation models

The previous trapped particle energy spectra were obtained by means of the simulation tool SPENVIS (Space Environment and Information System), a web interface by ESA allowing the modeling of the space radiation environment (trapped particles, cosmic rays and solar particle events) and its effects. The standard models used for trapped proton and electron spectra are the NASA AP-8 and AE-8 respectively (Sawyer and Vette, 1976; Vette, 1991). These models provide omni-directional (differential and integral) fluxes as a function of the trapped particle energy in the range

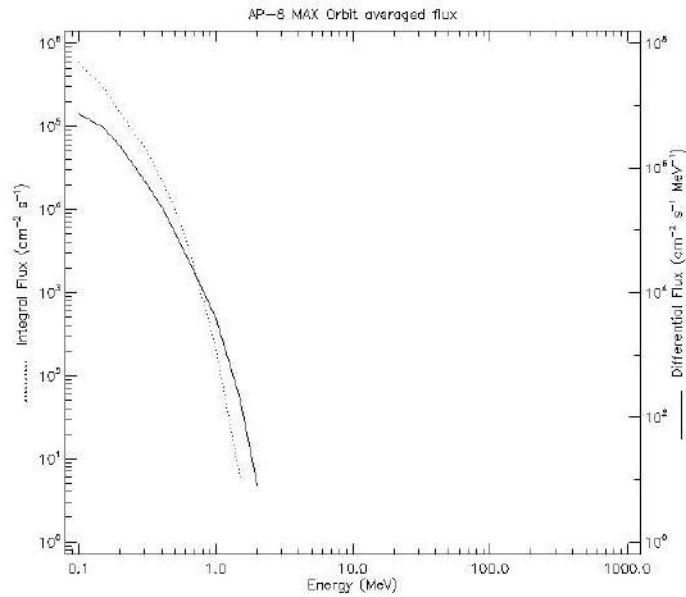


FIGURE 1.4: Trapped proton spectrum for a 36000 km altitude and 0 degrees inclination angle orbit. The duration of the simulated mission is 10 years.

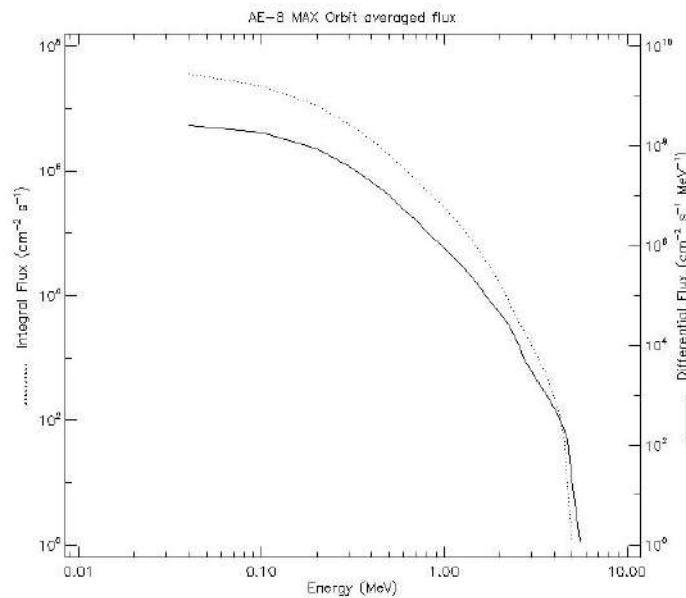


FIGURE 1.5: Trapped electron spectrum for a 36000 km altitude and 0 degrees inclination angle orbit. The duration of the simulated mission is 10 years.

0.1-400 MeV (protons) and 0.04-7 MeV (electrons). In reality the hypothesis of omnidirectionality is not always verified as the experimental data suggest strong angular (as well as temporal) dependence. It is noteworthy that, for altitude less than 1000 km, the measurements of trapped proton fluxes differ from AP-8 predictions from

60 to 500 (Daly et al., 1996). These models take into account also the solar activity (the term "AP/E-8 max" refers to solar maxima and "AP/E-8 min" to solar minima). The simulation of figure 1.2 and 1.3 is during a minimum of the solar activity, while that of figure 1.4 and 1.5 during a maximum of the solar activity.

The South Atlantic Anomaly

In addition to all the above-mentioned parameters affecting the concentration of radiation around Earth, high levels of radiation are found in the South Atlantic area and the consequent anomaly is known as South Atlantic Anomaly (SAA). This asymmetry is due to the different locations of geographical and magnetic poles. As a result, the Van Allen belts are closer to Earth to the side of SAA. The effect on proton concentration can be observed in figure 1.6.

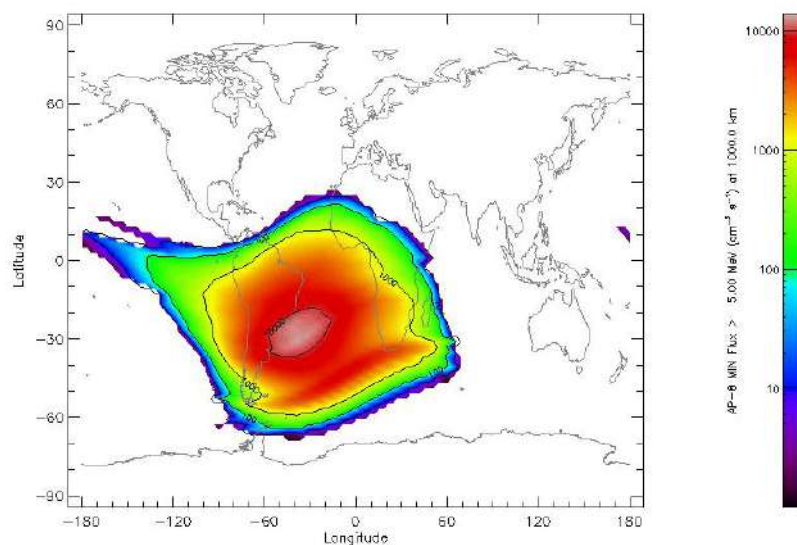


FIGURE 1.6: Trapped proton flux at 1000 km altitude.

It shows the concentration of trapped protons at 1000 km altitude as a function of latitude and longitude. This simulation was performed with SPENVIS and the world-map was generated with AP-8min model. The SAA is clearly visible in figure 1.6. It is located in a region in the Atlantic Ocean close to the south-east coast of Brazil.

1.1.2 Galactic cosmic rays

A significant contribution to the radiation in space comes from Galactic Cosmic Rays (GCRs). GCRs originate outside the solar system and are a background radiation omnipresent in space. GCRs have been accelerated in the last few million years at huge energies, likely following the explosion of a supernova and, owing to the effects of galactic magnetic field, have traveled many times across the galaxy. The interaction of these particles with the gas of interstellar space may lead to gamma

rays emission. The detection of such gamma rays represents the information of the crossing of cosmic rays through the Milky Way and other galaxies. GCRs consist predominantly of protons (about 85 %) with a flux of about 1 to 10 particles per cm^2 per second. Helium nuclei contribute to GCRs (about 14%) and the remaining 1% is distributed to heavy ions, also referred to as HZE ions (Durante and Cucinotta, 2011). The energies of GCRs are very broadly distributed over a spectrum ranging from energies of primary importance for space applications (10 MeV/u to 50 GeV/u) to the ultra-high energies up to 10^{20} eV (Xapsos, 2018). Figure 1.7 shows the relative abundance of the elements of energy 2 GeV/u. Although the abundance of

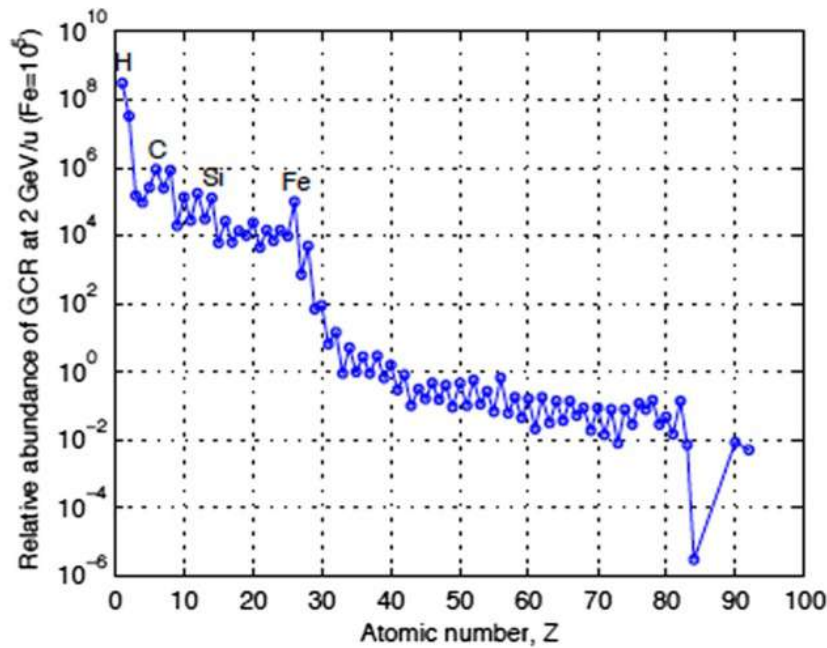


FIGURE 1.7: Relative abundance of Galactic Cosmic Rays of energy 2 GeV/u as a function of the atomic number Z .

HZE ions decreases as the atomic number Z increases, their contribution to the dose of GCRs is higher compared to that of protons because of the dependence of dose from Linear Energy Transfer (LET) which in turns is proportional to the square of Z (Durante and Cucinotta, 2011). The interaction of primary cosmic rays with the atmosphere generates a cascade effect in which new particles are produced. These particles are called secondary cosmic rays and include neutrons, pions, muons and positrons together with gamma rays and electrons. The flux of secondary cosmic rays has a maximum at the altitude of 18 km and then slowly drops down to the sea level (Campajola and Di Capua, 2017). The concentration of GCRs in the proximity of Earth depends on solar activity. The Sun emits a continuous wind of particles in the state of plasma. This phenomenon is periodic with a period of about 11 years and we are currently experiencing a minimum phase of the solar cycle. The strength of the solar wind influences the flux of cosmic rays. Figure 1.8 shows the Sun Spot Number (SSN), the flux of cosmic rays, the X-rays emitted from Sun, the flux of protons and the magnetic field strength during 20 years acquisition from 1983 to 2003. These data are from different detection stations. The solar activity is anti-correlated with the flux of cosmic rays.

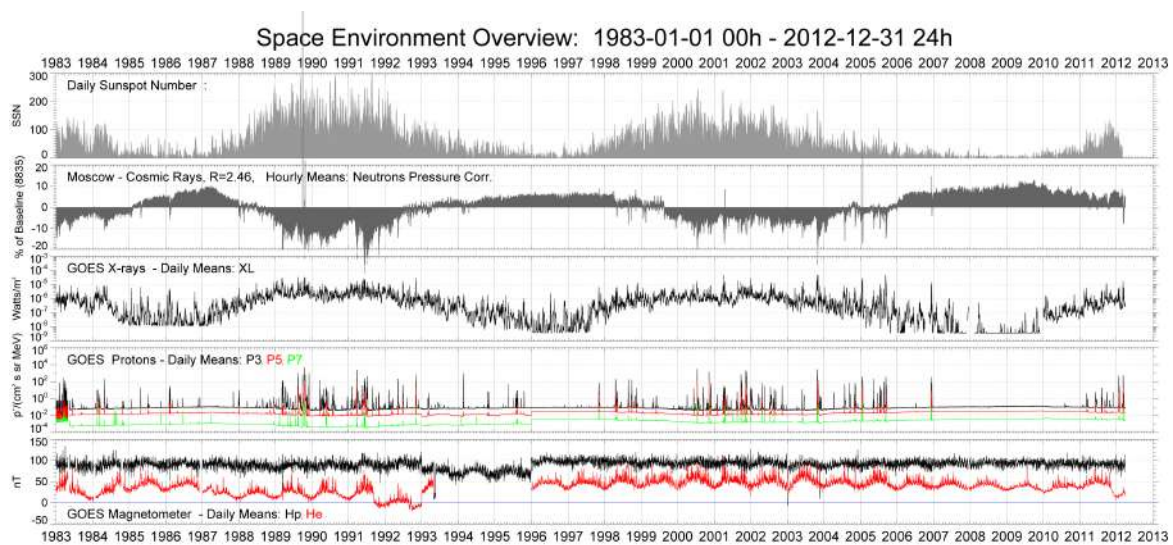


FIGURE 1.8: Image from ESA website showing the anti-correlation between the solar activity and the flux of cosmic rays.

1.1.3 Solar cosmic rays and solar particle events

The solar activity affects the radiation dose of a space mission in terms of particles emitted of different LET and fluxes. The solar wind consists in the emission from the corona of the Sun of fully ionized (plasma) particles including electrons, protons, alpha particles and HZE ions of low energy from 0.1 to 10 keV. Strong heating in the corona of the Sun, due to the solar magnetic field, leads to the formation of sources of intense solar flares where huge amounts of plasma are ejected. The massive events that usually follow the solar flares are called coronal mass ejections (CMEs). The Sun produces about three CMEs every day during a solar maximum and about one every five days during a solar minimum. Solar particle events (SPEs) are unpredictable events occurring when radiation emitted by Sun undergoes acceleration either close to Sun during a flare or in interplanetary space by CMEs. During a large SPE the fluences of protons of energy greater than 30 MeV can exceed 10^{10}cm^{-2} in several hours or days. SPEs as well as GCRs represent therefore a serious hazard for electronics and astronauts. Figure 1.9 shows the proton flux in the worst day (maximum solar emission) as a function of the proton energy for a space mission of 20 years in a 36000 km altitude and 37.8 degrees inclination angle orbit.

In this simulated space mission, the solar fluence of protons of energy greater than 20 MeV is around 10^{11}cm^{-2} and that of alpha and HZE ions of energy greater than 20 MeV/u is 10^7cm^{-2} . This simulation was performed with SPENVIS, that uses several models of calculation of SPEs. In this case the Emission of Solar Proton (ESP) model was used to estimate the solar heavy ion fluence (Xapsos et al., 2000), while for individual proton events the standard CREME-96 model was used (Weller et al., 2010). The last is based on the usage of data recorded during the last two important SPEs for representing the worst case proton event in the simulated space mission. The August 1972 event produced a flux of protons of energy greater than 10 MeV near Earth of about $10^6\text{cm}^{-2}\text{s}^{-1}$, while the October 1989 a peak flux of about

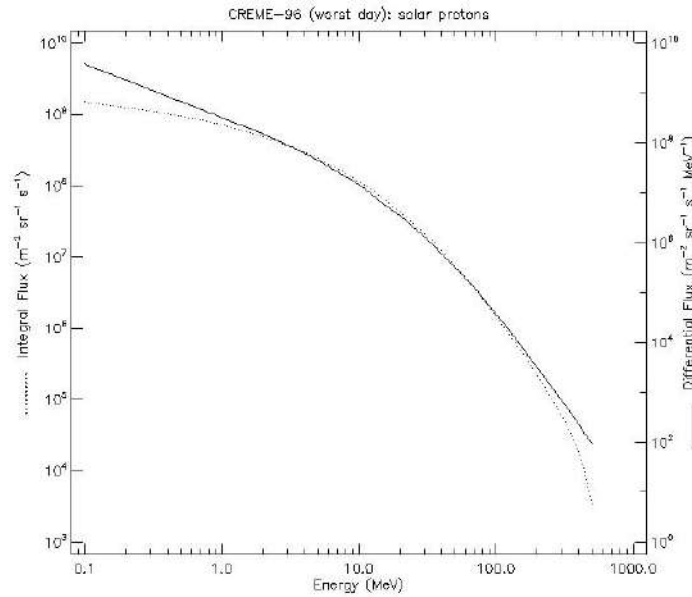


FIGURE 1.9: Solar proton flux for a 36000 km altitude and 37.8 degrees inclination angle orbit in the worst day of a mission of 20 years.

$10^5 \text{cm}^{-2}\text{s}^{-1}$ (Poivey and Day, 2002). The CREME-96 model is the standard model also for the calculation of GCR spectra.

1.2 Interaction of radiation with matter

The understanding of the effects of radiation on silicon devices requires the knowledge of physical processes of the interaction of radiation with matter. The main physical processes discussed in this section are ionization and atomic displacement. The physical quantities describing these phenomena are the stopping power and the non-ionizing energy loss (NIEL).

Ionization

An energetic charged particle interacting with matter loses its energy by collisions with atomic electrons. Ionization occurs when the collision is such that the electron is ejected from its orbit. Charged particles as protons, helium and HZE ions, electrons and positrons are direct ionizing particles, while neutral particles as photons or neutrons are indirect ionizing particles. An indirect ionizing particle delivers energy to the medium in a two-step process: set in motion of charged secondaries and their subsequent energy transfer to the medium. Ionizing radiation creates free charge in the matter. This affects the properties of the material and, for electronic devices, their performances. The physical quantity that describe the energy loss by a charged particle is the stopping power. In particular, the differential rate of energy loss by a charged particle per unit path length is expressed by the stopping power dE/dx (measured in MeVcm^2/mg or in $\text{keV}/\mu\text{m}$). In the classical theory it is given by the well known *Bethe and Bloch* formula. Since the stopping power

refers to the energy loss by a charged particle and not to the energy transferred to matter, it takes into account also the fraction of energy that is transformed into *Bremsstrahlung*. This amount of energy will presumably be stored far away from the primary ionization site, namely the track described by the particle. LET measures the energy transferred to the material net of this contribution. Stopping power data are available from several database (measurements) and calculation tools (models and simulations) (Ziegler, Ziegler, and Biersack, 2010; Berger, 1992). Often the codes and database show relevant discrepancies (in some case greater than 30%) between stopping power values from different codes and from experimental measurements (Paul and Schinner, 2004). This results in a relatively high uncertainty on LET and dose values, whose knowledge is essential for radiation hardness applications. For example, discrepancies as large as 30% have been observed for 4–5 MeV/u heavy ions such as ^{16}O , ^{40}Ar , ^{63}Cu and ^{84}Kr in light media as carbon and aluminum (Bimbot et al., 1978). The discrepancies are more evident in the Bragg peak region. This issue particularly concerns with the hadrontherapy applications where the importance of accurate and precise knowledge of the Bragg peak as well as of the range position is crucial for results of the treatment (Durante and Paganetti, 2016). As far as the medical applications, stopping power of liquid water for MeV energy protons has been recently measured and results are in contrast with the simulation tools and database (Paul and Sánchez-Parcerisa, 2013). Figure 1.10 shows discrepancies for recent measurements performed on a liquid water target.

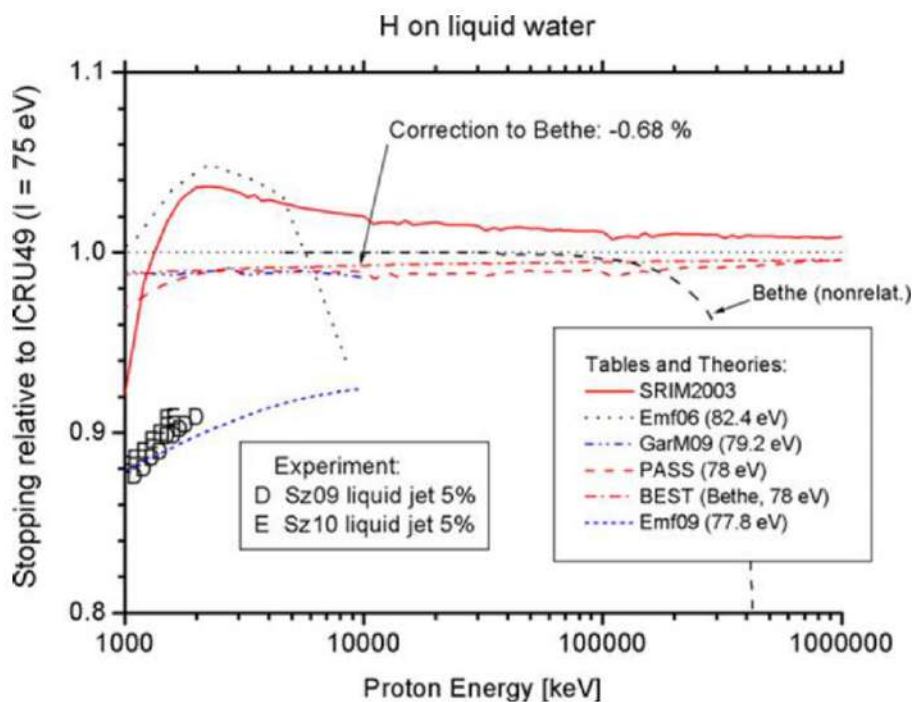


FIGURE 1.10: Stopping power of liquid water as a function of the proton energy for several codes and measurements. Significant discrepancies for MeV energy protons have been recently observed. This image is from (Paul, 2010).

It plots the stopping power of water relative to the reference curve ICRU49 as a function of the proton energy for several codes with the recent measurements.

Atomic displacement

In addition to the effect of ionization, particles such as neutrons, pions, protons, HZE ions and even high-energy electrons can displace atoms from their lattice sites producing bulk damage effects on electronic devices. These phenomena are referred to as non-ionizing processes in which the energy delivered by incident radiation results either in atomic displacements or in collisions in which the target atom doesn't move from its original position and the energy excess is released in form of lattice vibration at atomic level. In order to evaluate the amount of dose delivered by incident radiation that goes into displacement damage, it is useful to introduce the concept of non-ionizing energy loss (NIEL). The stopping power is in fact incomplete for a full description of such phenomenon. The two components of stopping power are the electronic and nuclear stopping power. The first considers processes of ionization only and the second refers the rate of energy loss by an incident directly ionizing particle by scattering with the atomic nuclei. The evaluation of this contribution is difficult because it requires the knowledge of the repulsive potential energy between the two atoms. Despite this quantity is difficult to evaluate in most experimental cases, the values of nuclear stopping power are tabulated on the basis of the *Bethe and Bloch* formula. The nuclear stopping power is often negligible with respect to the electronic stopping power. However, for low energies (\sim keV) and if the masses of the incident ion and that of the target are similar, the nuclear stopping power can no longer be neglected. As an example, figure 1.11 shows the SRIM data of $\text{Fe}^{56} + \text{Al}^{27}$.

The electronic, nuclear and total stopping power of aluminum are plotted in figure 1.11 as a function of the iron energy. In this case the nuclear stopping power is greater than the electronic stopping power by more than one order of magnitude up to about 100 keV; at 450 keV they have the same value and for higher energies the electronic stopping power dominates. These relative differences increase as the mass difference between projectile and target increases. Neither one nor the other contribution of the stopping power takes into account for the overall amount of energy loss that goes into displacement atom. The introduction of the concept of NIEL is therefore necessary. Since per definition nuclear stopping power does not involve electronic excitations, but only ionization processes, NIEL and nuclear stopping power can be considered the same quantity in absence of nuclear reactions. Non-ionizing energy is the part of incident energy delivered via both Coulomb (elastic) and nuclear (elastics and inelastic) interactions with the atomic nuclei which produces vacancy-interstitial pairs and phonons. At proton energies above about 10 MeV, nuclear inelastic interactions become significant, so the association of nuclear energy loss with elastically deposited energy and of ionization energy loss with inelastically deposited energy, is not appropriate (Dale et al., 1989). Analytic expressions of the NIEL have been derived in the years. Here the derivation by *Akkerman*

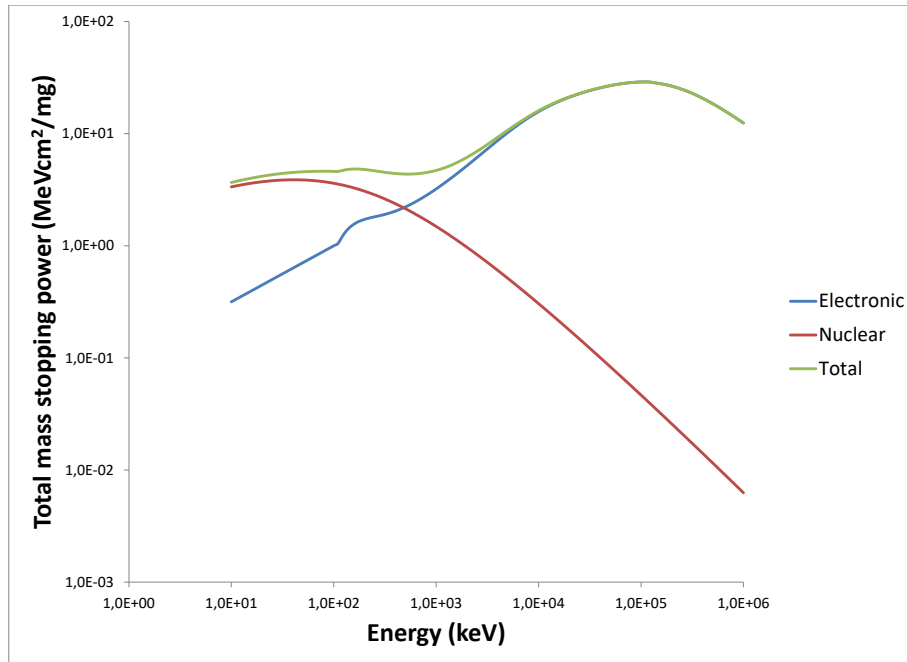


FIGURE 1.11: Stopping power of the aluminum as a function of the incident iron energy. The nuclear stopping power

et al. (which is employed in most of simulation tools) is presented (Akkerman et al., 2001). Let consider a primary particle of energy T_0 interacting with a lattice of atoms of atomic number A to emit a spectrum of recoils (of atomic mass A_1 and energies T) which in turn produce displacement damage. The NIEL parameter is defined as the portion of T_0 per unit travelling length which turns into displacement damage. The NIEL expression is:

$$NIEL = \frac{N_A}{A} \int_{T_{MIN}}^{T_{MAX}} dT Q(T) \left(\frac{d\sigma}{dT} \right)_{T_0} \quad (1.1)$$

The quantity $\left(\frac{d\sigma}{dT} \right)_{T_0}$ is the differential cross section of production of a given recoil of energy T at the incident energy T_0 ; $Q(T)$ is the partition factor. It gives the fraction of incident energy T lost by NIEL. The lower limit of integration is $T_{MIN} = 2T_d$ where T_d is the displacement damage energy threshold ($T_d = 21eV$ for silicon and $T_d = 10eV$ for GaAs). The upper integration limit is the maximum energy transferred by NIEL that is $T_{MAX} = 4T_0 A A_1 / (A + A_1)^2$. Several expressions have been proposed for the partition factor $Q(T)$. The accepted method is based on the *Lindhard's* approach, which enables the calculations of Q for various combinations of the primary particle (or recoil) and target atoms (Akkerman et al., 2001). Figure 1.12 shows the NIEL factor as a function of the incident radiation energy for protons,

neutrons and electrons (Poivey and Hopkinson, 2009). The data are from the following references (Dale et al., 1989; Summers et al., 1993; Akkerman et al., 2001; Jun et al., 2003; Vasilescu and Lindström, 2000).

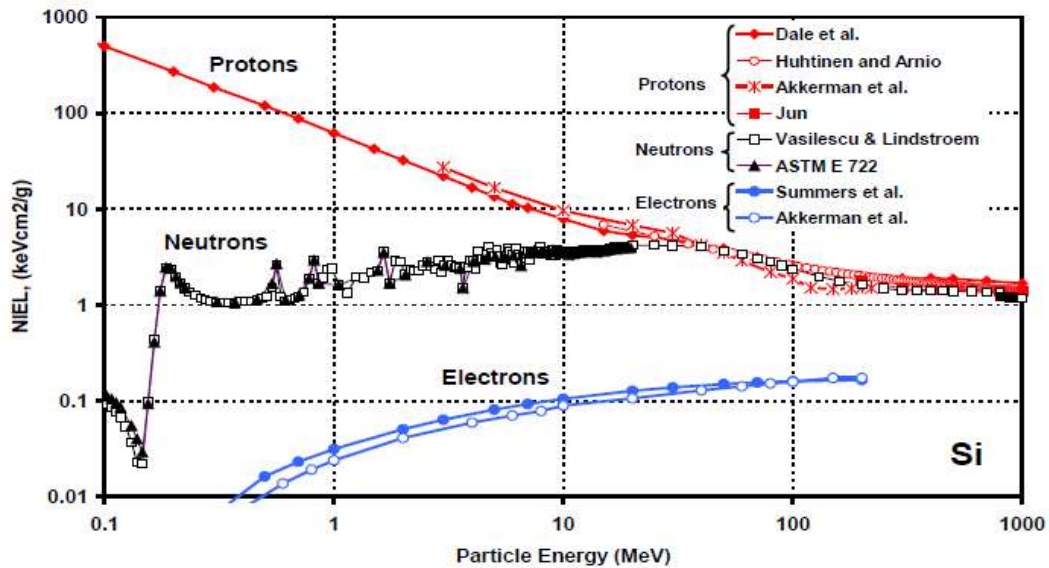


FIGURE 1.12: NIEL factor of Silicon as a function of the energy for incident protons, neutrons and electrons. The references are reported in the captions.

The NIEL factor of protons is higher to that of neutrons up to ~10 MeV. From tens of MeV on-wards the NIEL factor of neutrons and protons become approximately the same. The NIEL factor of electrons is lower than that of neutrons and protons by several order of magnitude. It increases with energy by remaining always lower to that of neutrons and protons.

1.3 Radiation effects on electronic devices

The effects of radiation on silicon devices can be classified in long-term, short-term and random effects. The first are Total Ionizing Dose (TID) and Displacement Damage Dose (DDD), the second Single Event Effects (SEEs). TID and DDD imply progressive degradation of the performances of the device that can be revealed also after months or years following the irradiation, while SEE, mainly dependent on the LET of the incident radiation, can be even destructive in the worst case. These effects are discussed in the next two subsections.

1.3.1 Total ionizing and displacement damage dose

TID effects are based on ionization of the atoms of the device exposed to radiation. TID is evaluated, for a mono-energetic charged particle, accordingly to the following formula:

$$TID [rad] = 1.6 \cdot 10^{-8} \times LET \left[\frac{MeVcm^2}{g} \right] \times \Phi [cm^{-2}] \quad (1.2)$$

In this formula the LET has to be evaluated at the right depth in the medium. Both LET and consequently TID are expressed with respect to a reference material (e.g. silicon). For a poly-energetic spectrum that is the more realistic situation, TID is given by the integral over energy of equation 1.2. TID consists in a long-term degradation of the performances of the device owing to cumulative charge deposited in SiO₂ or other dielectrics. Ionization creates electron-ion pairs in the material. The number of pairs (N_{pairs}) created per cubic centimeter and per 1 rad incident radiation for a material of density ρ and ionization potential ϵ can be easily calculated as follows (F is the conversion factor from eV to J) :

$$N_{pairs} \left[rad^{-1} cm^{-3} \right] = \frac{D \left[10^{-2} \frac{J}{Kg} \right] \times F \left[\frac{eV}{1.6 \cdot 10^{-19} J} \right] \times \rho \left[\frac{g}{cm^3} \right]}{\epsilon [eV]}$$

N_{pairs} for silicon ($\rho = 2.3g/cm^3$) is approximately equal to $2 \times 10^{13} rad^{-1} cm^{-2}$ and for silicon dioxide ($\rho = 2.2g/cm^3$) is $8 \times 10^{12} rad^{-1} cm^{-2}$.

Basic mechanism of total ionizing dose

In order to discuss the effects of ionizing radiation on electronic devices, we refer to figure 1.13 (Poizat, 2009).

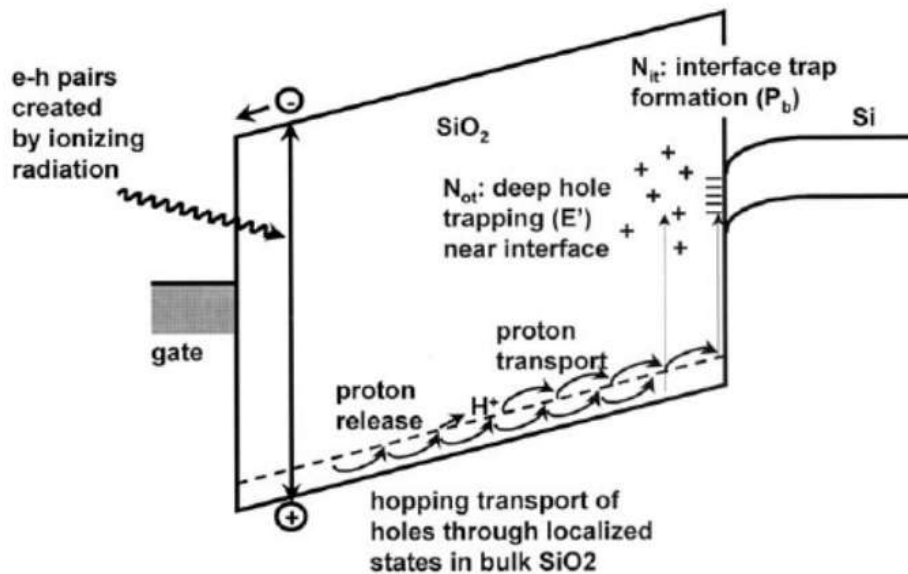


FIGURE 1.13: Schematic of TID damage (Poizat, 2009).

When ionizing radiation interact with an electronic device such as a Field Effect Transistor (FET), a high number of electron-ion pairs is created. There are recombination effects depending on the type of incident radiation and on the electric field. The electrons (high mobility) quickly drift away, while positive ions of lower mobility slowly drift towards the interface with silicon by hopping throughout a trap-to-trap mechanism. The positive ions can be trapped near the interface with silicon,

resulting in a positive charge build-up. This turns to the malfunction of the electronic device. A second ionizing-radiation-induced mechanism that causes serious issues in semiconductor devices is the proton release. The fabrication processes of semiconductors cannot avoid the presence of traces of hydrogen. This amount of hydrogen is mainly located in the gate-oxide traps. The motion of positive ions can displace protons from their trap by triggering therefore a proton motion towards the interface. The total trapped charge in the oxide can invert the channel interface, causing a lowering of the leakage current, creating a persistent gate biasing and influencing the transistors threshold voltage. This leads to the malfunction of semiconductors and in particular bipolar transistors.

Enhanced low dose rate sensitivity

It is noteworthy that bipolar devices show a typical behaviour with TID exposure. It was demonstrated that these devices have a more significant degradation when exposed at low dose rates (LDR) (Johnston, Swift, and Rax, 1994). Most of spacecrafts and satellites operate in LDR environment. This effect is referred to as Enhanced Low Dose Rate Sensitivity (ELDRS). The standard TID dose rate for ground testing is generally ~ 50 rad(Si)/s, whereas typical ELDRS testing is performed with dose rate of only 10–100 mrad(Si)/s. This implies that ELDRS testing is time-consuming and costly.

TID damage in space

Significant contributions to TID exposure in space environment include trapped electrons and protons and solar protons. Figure 1.14 is the output of a SPENVIS simulation (space mission of 1 year on a 300 km altitude and 51.6 degrees inclination angle orbit) that shows the different contributions to TID as a function of the aluminum shielding thickness. The main contribution to TID in this simulated orbit is from trapped electrons, following by trapped protons and solar protons. A significant part to TID in the first few millimeters of the aluminum shielding is also due to *Bremsstrahlung* emission.

Basic mechanisms of displacement damage dose

Although the long-term degradation effects of electronic devices due to TID are similar to that of displacement damage dose (DDD), the physical mechanisms are different (section 1.2). Technologies that are TID-tolerant are not necessarily DDD-tolerant. DDD effects basically consist in cumulative degradation of the device caused by displacement of atoms from their original sites in the crystalline lattice. Defects induced by the interaction of radiation with semiconductors are primary point defects including vacancies and interstitials (Poivey and Hopkinson, 2009). Clusters of defects are generated when the incident particle, such as a fast neutron or protons, transfers enough energy to the recoil atoms to allow large cascades of displacements. The incident radiation can displace an atom creating an interstitial-vacancy couple as well as stable defects. Figure 1.15 describes these two kinds of defect.

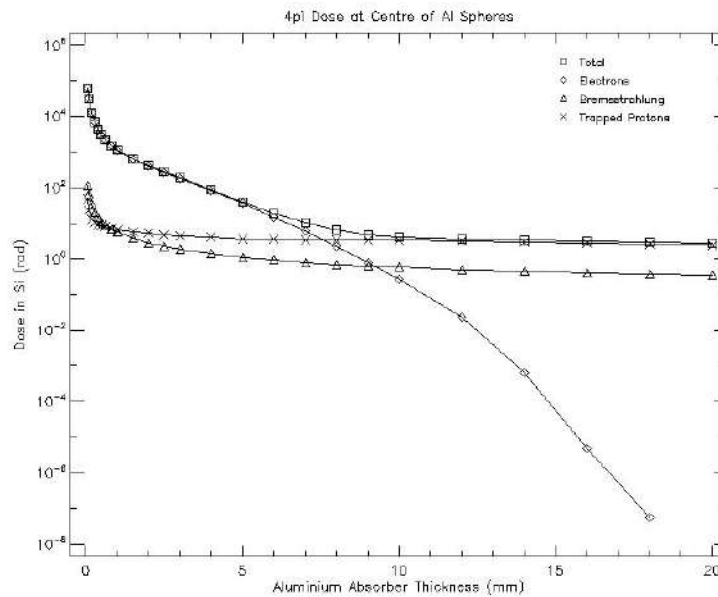


FIGURE 1.14: Contributions to TID as a function of the aluminum shielding thickness for a 300 km altitude and 51.6 degrees inclination angle orbit.

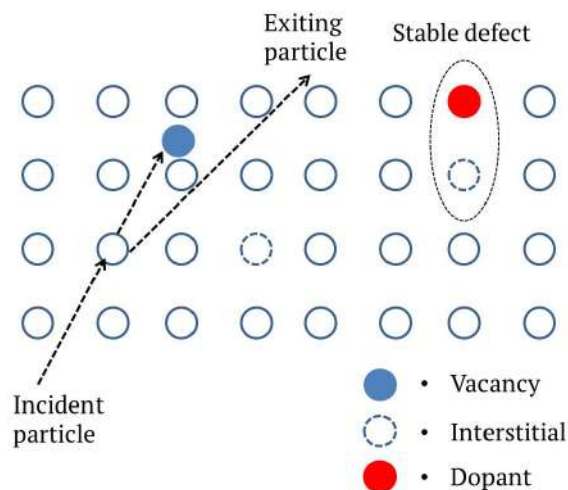


FIGURE 1.15: Schematic description of the displacement damage.

The incident radiation displaces the atoms locally, modifying the material structure and affecting fundamental semiconductor properties. The evaluation of DDD for an incident radiation that produces displacement damage is based on a calculation similar to that of TID, that is:

$$DDD [MeV/g] = NIEL \left[\frac{MeVcm^2}{g} \right] \times \Phi [cm^{-2}] \quad (1.3)$$

In the case of a poly-energetic spectrum, that is the more realistic situation, DDD is given by the integral over energy of the equation 1.3 in which the NIEL has to be evaluated for each specific component of the fluence spectrum.

Devices affected by DDD

Devices such as solar cells, particle detectors and image sensors depend on crystalline bulk structure for their correct operation. For example, the output power of a spacecraft solar array degrades during the space mission because of the displacement damage effects. The depletion area of silicon detectors shows displacement damage effects such as the increase of recombination centres in silicon. This lead to malfunction of the device in fundamental detector properties such as the energy resolution. These devices have shown high sensitivity to DDD (Srouf, Marshall, and Marshall, 2003). Displacement damage is also important for opto-electronic integrated circuits, such as charge-coupled devices (CCD). The defects produced lead to corrupting states in band gaps and therefore increased dark current and reducing gain and charge transfer efficiency.

DDD in space

Typical sources of DDD exposure in space environment include trapped protons, solar protons and less trapped electrons. Figure 1.16 shows the output of SPENVIS simulation for 10 years long space mission in which NIEL values are plotted versus the aluminum shielding thickness.

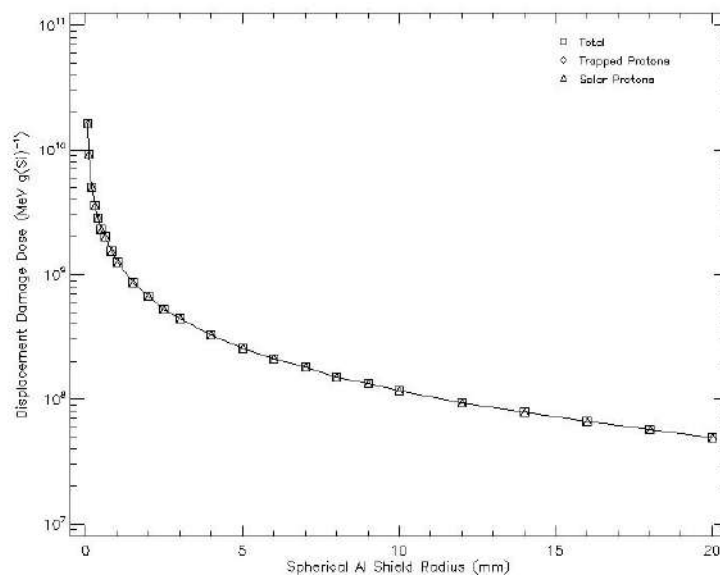


FIGURE 1.16: Contributions to NIEL as a function of the aluminum shielding thickness for a 36000 km altitude and 0 degrees inclination angle orbit.

In this space mission the main contribution to NIEL is from solar protons, while the low-energy trapped protons are stopped in the aluminum shielding. The DDD contribution at the aluminum surface is 10^{10} MeV/g, corresponding to a dose of 160 rad.

1.3.2 Single event effects

Single Event Effects (SEEs) are short-term effects caused by interaction of a single energetic particle with an electronic device. GCRs, SPEs and high energy trapped particles (protons, electron and heavy ions) can be the cause of SEEs. These effects are induced by ionization of primary particles or by ionization of the charged secondaries.

Basic mechanism of SEE

The incident radiation in electronic devices generates a localized ionization path which can induce a SEE if the charge delivered is greater than a charge threshold Q_{tr} . The charge collection mechanisms is very complex and often redefined in literature. A prompt component due to the drift or funnelling of electron-ion pairs generated and a delayed component due to their diffusion in regions of lower electric field are the main mechanisms (Sturesson, 2009). Finally the charge generated by a SEE interaction is collected by the device, producing a spurious voltage signal on a sensitive node that causes malfunction of the electronic circuit. SEE probability is in fact a function of the track structure of the incident radiation and therefore of the radiation LET. SEE probability σ (in cm^2) is defined as the ratio of the number of SEEs (N_{SEE}) over the fluence of particles impinging the electronic device

$$\sigma [cm^2] = \frac{N_{SEE}}{\Phi [cm^{-2}]}$$

Figure 1.17 shows the SEE cross section as function of the radiation LET.

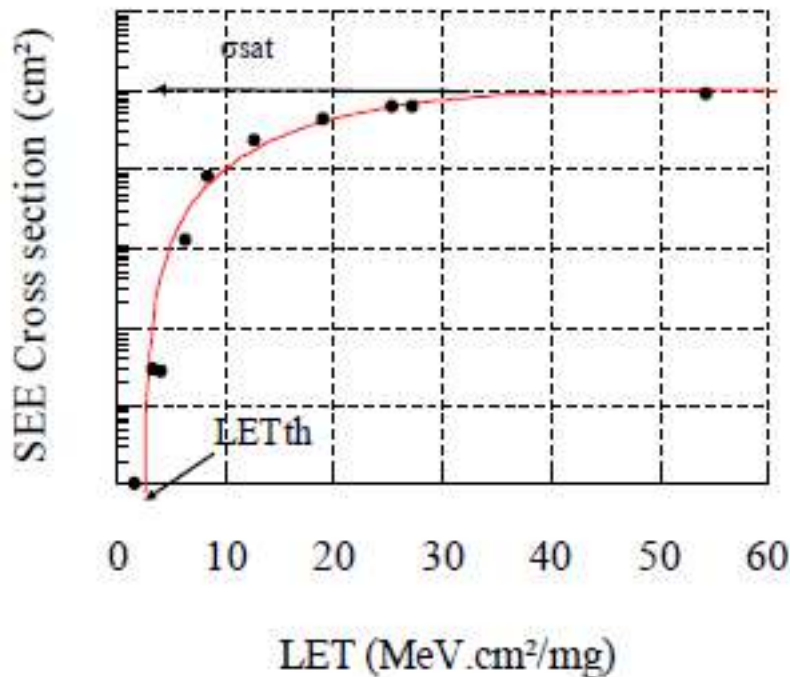


FIGURE 1.17: SEE cross section as a function of the radiation LET (Sturesson, 2009).

Particles with LET values less than LET_{th} cannot trigger a SEE because the deposited charge is less than Q_{crit} . Viceversa, particles with LET values greater than LET_{th} induce a SEE because the charge collected by the device is greater than Q_{crit} . SEE cross section rapidly grows as the LET increases up to a saturation level σ_{sat} for which the SEE probability remains constant as the LET increases.

Main typologies of SEEs

Depending on the typology of error induced by a SEE, these are classified in many ways. SEEs can induce non-destructive soft errors such as bit flips in memory cells (or in registers) or multiple bits upsets. This class of effects is referred to as single event upset (SEU) and usually a reset of the device is enough for restoring the normal behavior. Events leading to temporary loss of device functionality are soft errors known as single event functional interrupts (SEFI) which mainly affect memories or microprocessors or single event transient (SET) when ions strike e.g. a comparator leading to transients in the signals. The restore of the correct device's performances is also in this case possible by reset or power cycle. Hard errors caused by events which interrupt device function or permanently damage the device are single event latch-up (SEL) (high-current conditions such as short circuits on CMOS devices), single event burn-out (SEB) (high-current conditions leading to definitive device rupture), single event gate rupture (SEGR) (gate dielectric rupture due to high current conditions on e.g. power MOSFET) and single event hard errors (SEE) (permanent change of state of a memory).

SEEs testing

Primary sources of SEEs in the space around Earth are high-energy GCRs, SPEs and trapped protons in radiation belts Figure 1.18 shows the output of a SPENVIS simulation for a 10 years space mission on a 20000 km altitude and 51.6 degrees inclination angle orbit. The plot shows the radiation flux as a function of the LET. The fluxes are calculated taking into account the spacecraft shielding and the dimensions of the device to be tested. A SEE test of a device for this simulated space mission need to be performed with high LET values. SEE ground-tests are therefore performed with particle accelerators capable of providing the required LET. The exposure of the device under test (DUT) to several radiation types can be also carried out by varying the tilt angle of the DUT so that to increase the path of particles striking the DUT and consequently the LET values. Usually the devices to be tested have a lid and/or a package that must be accurately removed before the exposure. An alternative consists in considering these elements during the exposure. This can be done only if the dimensions and composition of the package are known. Unfortunately these information are not provided by the manufacturers. Figure 1.19 is a schematic that shows the effects of materials such as lid, package or absorbers to the correct evaluation of the radiation parameters. These effects are progressively important as the energy loss of the incident radiation in the material increases. For example, an incident 16 MeV proton beam has a LET of $22 \text{ MeVcm}^2/\text{g}$ and of $31 \text{ MeVcm}^2/\text{g}$ after 2 mm PMMA on the DUT position (figure 1.19.a). If the complex absorber-DUT is tilted by 45 degrees angle with respect to the beam axis (figure 1.19.b), a LET of $40 \text{ MeVcm}^2/\text{g}$ on the DUT must be considered. The total charge

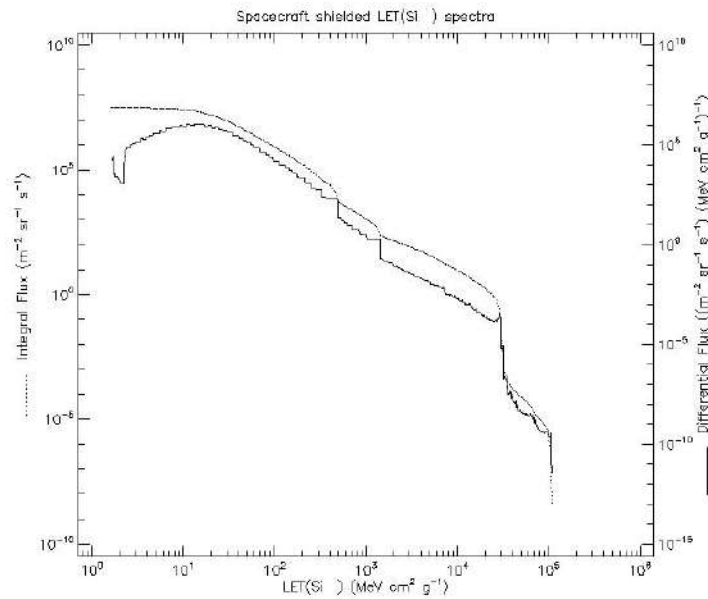


FIGURE 1.18: Flux for a 20000 km altitude and 56.2 degrees inclination angle orbit.

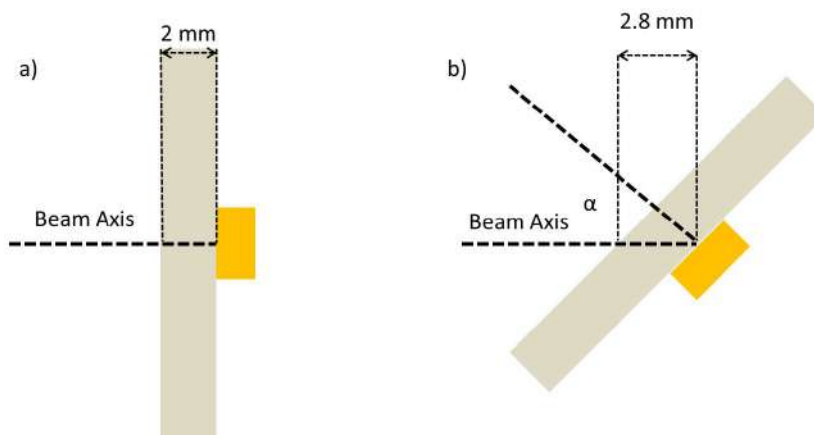


FIGURE 1.19: Effects of materials (absorbers, lid or package) for the correct evaluation of LET on an electronic device.

delivered to the DUT is proportional to the total energy loss E_{loss} in the DUT that is:

$$E_{loss} = \int_{t_{DUT}} LET(E) dt$$

where the integral is all over the DUT thickness t_{DUT} . Figure 1.20 shows a picture of an image under optical microscope of an integrated circuit permanently damaged by a destructive SEE caused by a high energy HZE ion.

The picture and exposure were carried out by our group during campaigns of exposure of electronic devices for space applications. In this case the SEE led to the total breaking of the device.

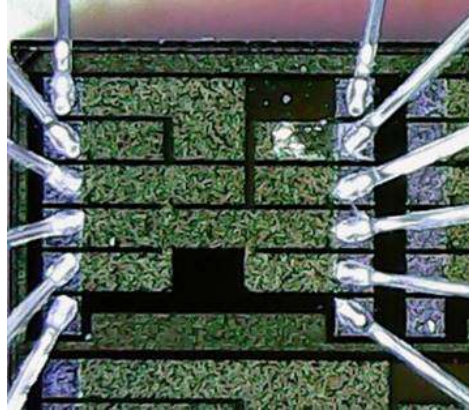


FIGURE 1.20: Magnification with an optical microscope of an integrated circuit damaged by a high energy HZE ion causing a destructive SEE.

1.4 Neutron damage

The interaction of energetic cosmic rays with the Earth's atmosphere generates a cascade process in which many secondary particles are created including photons, muons, protons, alpha particles, HZE ions and neutrons. Figure 1.21 shows the simulated flux of particles produced by cosmic rays as a function of the energy.

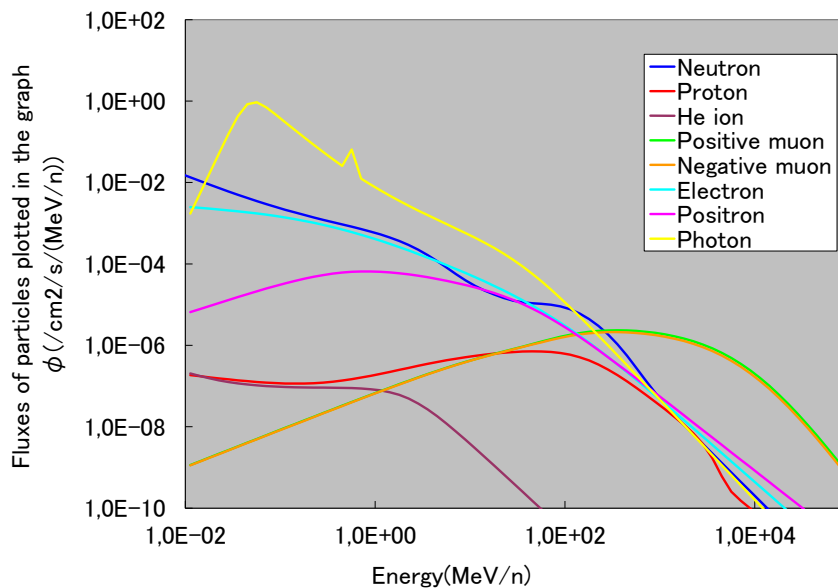


FIGURE 1.21: Spectra at sea level of particles produced for interaction of cosmic rays with the earth's atmosphere.

These spectra are obtained with the EXPACS program (Sato, 2015). It allows

calculations of terrestrial cosmic ray fluxes of secondary particles anytime and anywhere in the Earth's atmosphere. In particular, the spectrum of figure 1.21 represents secondary particle fluxes in Napoli. The dominant contributions to flux up to 200 MeV come from photons, neutrons and electrons while for higher energies (greater than 700 MeV - 1 GeV) positive and negative muons are mainly present. As a result the main component to the effective dose from cosmic rays at sea level is from muons (0.2 mSv/year) while neutrons contribute to a lesser extent (0.05 mSv/year). The neutron component increases rapidly with the altitude and at typical commercial flight altitudes (11000 meters) the neutron dose is 11 mSv/year while that of muons is relatively decreased to 1.7 mSv/year. Proton dose at 11000 meters significantly increase to 5 mSv/year for a total dose (sum of all the contributions) of 27 mSv/year with respect to 0.3 mSv/year at sea level. This poses serious problems of radiation protection of flight crew (Nicholas et al., 1998). Figure 1.22 summarizes the dose data in a histogram showing the effective dose of secondary particles produced by interaction of cosmic rays with atmosphere at sea level (total dose from cosmic rays: 0.3 mSv/year) and at 11 km altitude.

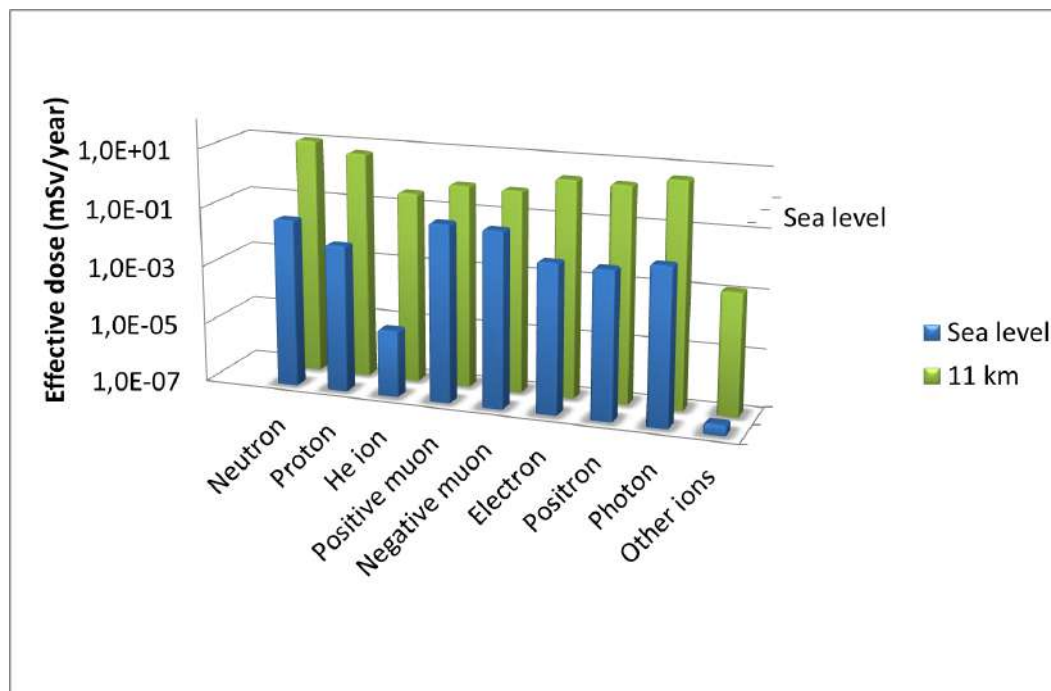


FIGURE 1.22: Histogram of effective dose for several secondary particles produced by cosmic rays at sea level and at 11000 meters altitude.

This radiation is an issue not only for humans but also for electronics, both at flight altitude and terrestrial level. Failures of semiconductor devices caused by cosmic radiation exposure is well known in space and avionics applications and recently it has been confirmed also for terrestrial applications (Davidson, Blackmore, and Hess, 2004). In fact under 20 km altitude the main contribution to SEE in avionic systems is due to neutrons. Atmospheric neutrons can penetrate the natural shielding of buildings, equipment and circuit package by inducing soft errors in integrated circuits and in the worst case breakdown of power devices (Leray, 2007) even at sea

TABLE 1.1: Main nuclear reaction induced by neutrons that can lead to damage in silicon-based devices.

Reaction	$E_{th,^{28}\text{Si}}(\text{MeV})$	$E_{th,^{16}\text{O}}(\text{MeV})$
Elastic	0	0
Inelastic	1.78	6.06
(n, α)	2.76	2.35
(n, p)	4.00	10.24
(n, d)	9.70	10.52
$(n, n + \alpha)$	10.35	7.61

level. This radiation is a concern for fundamental electronic circuits in critical applications such as power devices for locomotives and pace-makers in CMOS electronics. Data in figure 1.21 show that the flux of neutrons at sea level with energy above 1 MeV which may cause SEE in modern electronics is 70 neutrons/(cm²hour) while that of energy greater than 10 MeV is 44 neutrons/(cm²hour). This means that the 37 % of fast neutrons which can affect electronics with SEEs is in the range 1-10 MeV. As for the SEEs caused by all particles, neutron-induced SEEs strongly depends on the energy of neutrons being also threshold effects and the rate of effects depends on the flux. A single fast neutron interacting with matter may produce a variety of secondary particles including protons, neutrons, alpha particles and even HZE recoils. These high energy secondaries interact in the silicon matrix by producing current spikes that can alter data. Since the flux of these neutrons is not high compared to other kind of radiation, no TID and DDD are observed for atmospheric neutrons, but only SEEs. This is not the case of environments in which the neutron dose is significantly high such as in the energy physics experiments where e.g. silicon vertex and tracking detectors are exposed to high fluences of neutrons up to 10¹²-10¹³neutrons/cm² (Hartmann, 2011). The mechanisms leading to an atmospheric neutron SEE must be sought in the basic interactions of neutron with matter. As far as silicon and oxygen the main interactions are reported in table 1.1 where the data of energy thresholds E_{th} for ²⁸Si and ¹⁶O are from National Nuclear Data Center (NNDC) database (Chadwick et al., 2011).

Despite the neutron induced SEEs occur for incident energies greater than 10 MeV and the range of recoils produced by these reactions is in many cases of few microns, SEEs can be triggered also by neutrons of energy of few MeV. This is due to the fact that the active volumes of electronics is often very small (the new technologies have devices of some tens of nm). Technological developments bring smaller and faster devices that operate at reduced bias voltages, but they then present an increased susceptibility to neutrons in the range 1-10 MeV. Thermal neutron may induce SEE when the concentration of elements with high cross-section of charged-particle production are present such as when boron becomes significantly high. For example, the consequences of these interactions on the soft-error rate of 40 nm SRAM at ground level have been investigated in depth ((Autran et al., 2012)). The reaction $n + ^{10}\text{B} \rightarrow \alpha + ^7\text{Li}$ has in fact a very high cross section of 10³ - 10⁴ barns for

incident thermal energies. Baumann *et. al.* found that BPSG (Boron Phosphor Silicate Glass) films, which are used for smoothing the surface of semiconductor wafer for precise lithography, are particularly sensitive to soft errors induced by thermal neutrons (Baumann and Smith, 2000). In conclusion, since neutrons induce damage in electronics, there is a high requirement in having well characterized neutron beams of different energy range and fluxes.

Chapter 2

Radiation sources and dosimetry

Radiation Hardness Assurance (RHA) include all tests and activities to verify the proper operation of electronic components to be employed in harsh radiation environment. The definition of the environment, selection of parts, design and implementation of radiation tests and design of radiation tolerant systems are the main activities of RHA tests. In this thesis we focus on the implementation of radiation tests and more specifically on the methods and techniques to measure the dose on electronic devices. Furthermore, in order to develop and setting-up innovative techniques of radiation detection for X-, gamma-, charged particle- and neutron-radiation, the understanding of the state of the art dosimetry techniques is necessary. This chapter begins with the presentation of the demands (in terms of radiation field characteristics) by International Standards for RHA tests. Successively the standard radiation sources and dosimetry methods are discussed for X-, gamma- and charged particle radiation respectively (sections 2.2, 2.3, 2.4 and 2.5). The radiation sources and detection systems discussed in these sections have been used for the testing and dosimetry cross-checking of new detection techniques developed within the framework of this thesis. In particular, the Gammacell of ISOF-CNR at Bologna, the ILU-6 electron LINAC at Warsaw, the Proton Irradiation Facility (PIF) at PSI and the 18/9 IBA cyclotron at Sevilla were used for the works with radiochromic films, namely the absolute calibration and real-time reading discussed in Chapter 3 and Chapter 4. The tandem accelerator at Catania was used both for the mentioned works with radiochromic films, for the testing of the innovative neutron detector, discussed in Chapter 5, and for the characterization of neutron beams presented in Chapter 5.7. As far as the radiation detection methods, new techniques developed by our research group are presented in section 2.6 and 2.7. In particular, section 2.7 discusses a powerful innovative method, based on *Rutherford Backscattering Spectroscopy* (RBS), for accurate and real-time measurements of important physical quantities such as flux, fluence and dose on the device position. This method has been designed and implemented at the tandem accelerator of University of Napoli Federico II. Section 2.8 discusses the methods of neutron production by focusing in the demands for radiation hardness applications. The number of facilities providing neutron beams with particular characteristics (e.g. white spectrum and/or mono-energetic neutrons) is limited with respect to the demand. This pushes to the development of neutron sources with well-characterized neutron beams. Finally, the basic principles of neutron detection are given in section 2.9 where the attention is given mainly on fast neutron detection for their importance in radiation hardness applications.

2.1 International standards

International protocols and standards contain the guidelines for the tests of Electrical, Electronic and Electro-mechanical (EEE) components for applications of RHA. The main standards adopted by the scientific community are the European Space Components Coordination (ESCC) by ESA and the United States military standard MIL-STD. ESA standard guidelines ESCC/22900 for TID tests and ESCC/25100 for SEE tests are meant for irradiation testing of integrated circuits and semiconductors for space applications, while MIL-STD-883 specifications were initially written for military applications only, but nowadays are applied also in the field of space applications. Other reference documents, recalled by ESCC and MIL-STD, are the ASTM (American Society for Testing Materials) standards containing specific indications on several topics including dosimetry methods for calculation of absorbed dose (ASTM E 666), application of Thermo luminescence Dosimetry (TLD) systems for determining absorbed dose in radiation-hardness testing of electronic devices (ASTM E-668), minimization of dosimetry errors in testing of electronic devices (ASTM E 1249), methods for application of ionization chambers to assess the low energy gamma component of ^{60}Co irradiators (ASTM E 1250) and standard practice for use of a radiochromic film dosimetry system (ASTM E 1275). The knowledge of these demands in terms of radiation sources, dose uncertainties, radiation field uncertainties and dose rate windows are fundamental for developing new reliable dosimeters and radiation detection techniques. Both the standards allow irradiations for TID tests with gamma rays from ^{60}Co . ESCC/22900 proposes also irradiations with an electron accelerator beam. Furthermore, alternative sources that can be correlated to these sources may be used. The field uniformity and dosimetry must be affected to less than 10% uncertainty for ESCC/22900 and less than $\pm 10\%$ for MIL-STD-883E. The dose rate windows for TID tests are divided in a standard dose rate in the range 0.1-50 rad(Si)/s and a low dose rate (LDR) in the range 0.01-0.1 rad(Si)/s for ESCC/22900, while the MIL-STD-883E states that acceptance tests must be carried out in a wider range from 50 to 300 rad(Si)/s. However, if the maximum dose rate is < 50 rads(Si)/s in the intended application, the parties to the test may agree to perform the test at a dose rate less than the maximum dose rate of the intended application. These dosimetry requirements are summarized in table 2.1.

TABLE 2.1: Dosimetry requirements for TID tests by International Standards.

	ESCC22900	MIL-STD-883E
Source	^{60}Co ; e ⁻ accelerator	^{60}Co
Dose uncertainty	<10%	< $\pm 10\%$
Field uniformity	<10%	< $\pm 10\%$
Dose rate	0.1-50 rad/s; 0.01-0.1 rad/s	50-300 rad/s

Although the ionizing dose in space is mainly due to electrons and protons and the dose rates in space are of the order of 10^{-2} - 10^{-4} rad/s (very far from the dose rates of radiation facilities), the criteria adopted by the standards aim at reproducing the

effects of radiation on electronics and not the environment itself. For this reason, for example, X-ray tubes are also employed for TID tests. X-rays irradiations are also implemented at wafer level testing for high dose-rates up to 2000 rad(Si)/s, providing a fast feedback of the radiation tolerance performances during the device fabrication. In some cases protons from accelerators are in some cases considered for TID tests.

2.2 Gamma sources

^{60}Co gamma sources are standard sources for TID tests. The radioisotope ^{60}Co (half life: 5.3 years) undergoes a β^- decay (99% branching ratio) to the second excited level of ^{60}Ni which emits a gamma ray of 1.17 MeV to the first excited state of ^{60}Ni which in turns goes to the ground level throughout emission of a 1.33 MeV gamma ray. Figure 2.1 shows the scheme of decay of ^{60}Co .

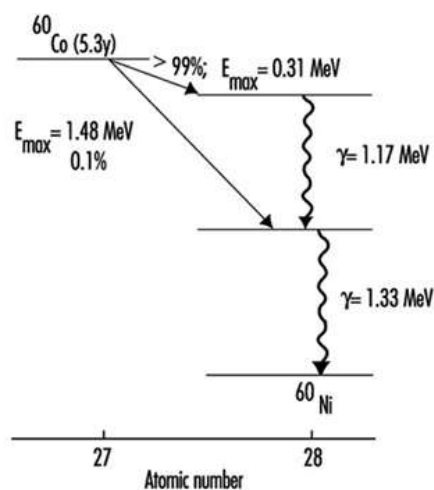


FIGURE 2.1: Scheme of decay of ^{60}Co .

The facilities of ^{60}Co gamma sources can be designed in different ways. It is possible to distinguish three main categories: gamma cell, gamma camera and panoramic irradiators.

Gamma cell consist in self-shielded vertical cylinders with the centre surrounded by ^{60}Co vertical rods. The dose-rate of these irradiators is determined by the activity of the ^{60}Co rods and is uniform within the irradiation area. The uniformity should be measured and verified periodically for a correct operation of the gamma cell. An opening allows the positioning of the specimens to be irradiated. The ISOF-CNR (Institute of Organic Synthesis and Photoreactivity of Consiglio Nazionale delle Ricerche) at Bologna is equipped with two Gammacell220. Figure 2.2 shows a picture of the Gammacell220 irradiator at ISOF-CNR.

These units basically consist of annular source permanently enclosed within a lead shield, a cylindrical drawer and a drive mechanism to move the drawer up or down along the source centre-line.

A second type of gamma irradiator is the gamma camera consisting in an irradiation area, for example a shielded room in which the ^{60}Co rods can be inserted (radiation on) and withdrawn (radiation off) by means of a remote controller outside the room.



FIGURE 2.2: Picture of a Gammacell220 irradiator.

The specimens can be manipulated, if necessary, during irradiation with suited mechanical arms. The specimens are putted in fixed positions where the dose rate is known (iso-dose curves). The ESA-ESTEC (European Space Research and Technology Center) hosts such a gamma irradiator of activity (in 2016) of 2000 Ci (74 TBq). This source is suited for TID tests at several dose rates in the range specified by the standards.

The field of a panoramic gamma irradiator is point-like. The source is shielded by a lead casing and gamma rays exit from a dedicated window. The radiation field has conical shape and iso-dose curves allow irradiations of specimens at several dose rates depending on the activity of the ^{60}Co source. The National Accelerator Center (CNA) of Sevilla has such a typology of ^{60}Co irradiator with a high activity (in 2014) of 331 TBq (Morilla et al., 2014).

2.3 Dosimetry for gamma and X radiation

Gamma and X-radiation fields are usually characterized by means of one or more active or passive dosimeters. The most used are discussed in the following.

Ionization chambers

As far as the active dosimeters, ionization chambers are the most employed for these applications because of their reliability, wide sensitivity range, accuracy and precision. Ionization chambers are gas filled detectors with two electrodes to which a potential difference is applied. The chambers may have the electrodes in the form of parallel plates or in the form of a cylinder arrangement with a coaxially located internal anode wire. The incident radiation ionizes the gas creating electron-ion pairs. The electrode collect the charge created which is measured by e.g. an electrometer. Ionization chambers are even nowadays the dosimetry standard in many laboratories and clinics for applications in radiation hardness and medical physics. Several types of ionization chambers are available on the market to meet requirements in terms of dynamic range, sensitivity and geometries. As an example, Farmer ionization chambers (0.6 cm^3) are thimble chambers for measuring high-energy photon and electron radiation in air or in tissue-equivalent material. These instruments are

sensitive for photon and electron incident energies ranging from 30 keV to 50 MeV; the response is energy-independent within few points percent. The read-out is very easy being made by means of electrometers. These chambers are intensively used in medical physics for measurements of percentage depth dose curve (PDD) and dose to phantom. Furthermore, ionization chambers are extensively used for reliable characterization of irradiation facilities. As an example figure 2.3 shows the dose rate as a function of distance of a 38 MBq $^{90}\text{Sr}/^{90}\text{Y}$ beta source of University of Napoli Federico II. This source is proposed for TID tests as alternative to stan-

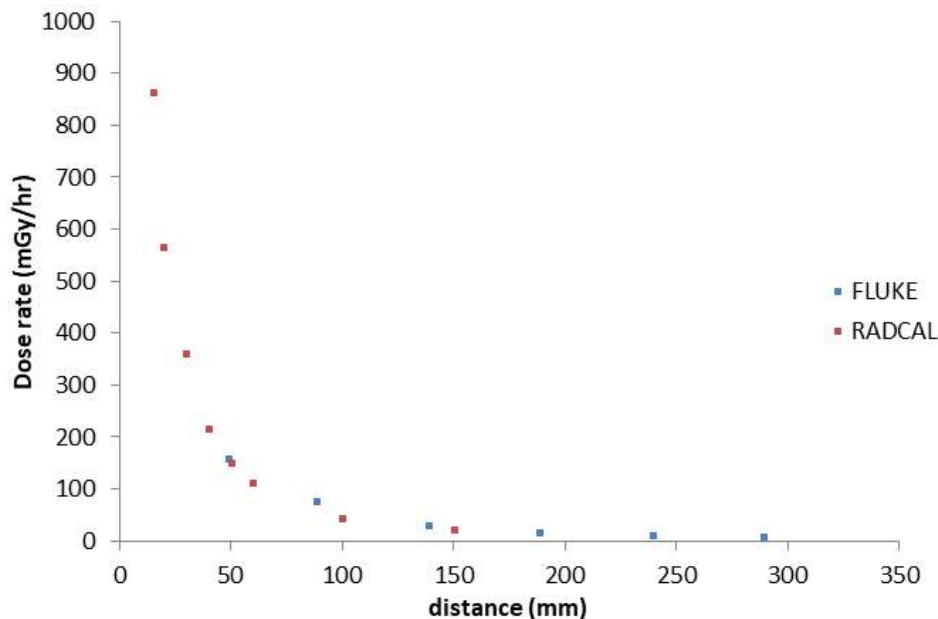


FIGURE 2.3: Dose rate of the $^{90}\text{Sr}/^{90}\text{Y}$ measured with FLUKE and RADCAL ionization chambers.

dard ^{60}Co gamma sources. This topic is discussed in detail in the next chapter. This radiation source was completely characterized by means of a general purpose Radcal Ionization Chamber (6 cm^3) and a Fluke Biomedical 451B Ion Chamber Survey Meter (349 cm^3). It is noticeable the agreement between ionization chambers with different characteristics and performances. Commercial ionization chambers are calibrated with respect to a reference radiation source (e.g. ^{60}Co and ^{137}Cs). If ionization chambers are employed for measurements of radiation types and energies other than the reference type, this must be taken into account. Usually the correction factors as a function of the energy and radiation type are provided by data sheets, such as for the case of FLUKE and Radcal Ionization Chamber.

Thermoluminescent dosimeters

Thermoluminescent dosimeters (TLD) are based on the ability of some crystals such as doped calcium (CaF_2) or lithium fluorides (LiF) or alumina (Al_2O_3) of trapping excited electrons at intermediate energy levels between the valence and conduction band. The traps in the crystal are created by pristine or artificial structural defects such as chemical impurities or doping agents. During irradiation, the energy is transferred to the electrons in the valence band with subsequent shift of some of

them to the conduction band and creation of electron-holes pairs. Some pairs recombine immediately and other remain trapped in the intermediate levels for relatively long times. The heating of the crystal provides enough energy to the electrons for decay to the valence band. This process is characterized by emission of light. The emitted light as a function of the heating temperature or the time is known as glow curve. It has characteristic peaks which integral is proportional to the dose. The setup for determination of glow-curves consists in a heater, a photo-multiplier-tube (PMT) for detection of luminescent light and a read-out system allowing the observation of the glow-curves. The read-out and the evaluation of dose are carried out after the irradiation and therefore TLDs cannot provide real-time dosimetry. Owing to the wide dynamic range (10^{-5} to 10^3 Gy), low dimensions and weight, TLDs are mainly employed for radiation protection, although they are used also for dosimetry verification of irradiation facilities. Commercial TLDs are not capable of detecting neutrons. However, lithium fluoride TLDs enriched with ^6Li have shown a very good sensitivity to thermal neutrons and for this reason, these dosimeters have been recently employed for neutron/gamma discrimination in mixed neutron/gamma fields such as that of reactors.

Chemical dosimeters

Fricke and alanine dosimeters are chemical dosimeters. Fricke dosimeters consist in a water solution of ferrous ions (Fe^{2+}). The ionizing radiation triggers the reaction of oxidation of ferrous ions in ferric ions (Fe^{3+}) which number is proportional to the absorbed dose. The number of ferric ions is determined by spectrophotometric methods throughout absorption of light of fixed wavelength (typically 304 nm). The absorbed dose D is proportional to the difference of absorbances before (A_0) and after (A) irradiation in accordance with the following relation:

$$D = N_A \frac{(A - A_0)}{\rho G l \epsilon_m} \quad (2.1)$$

where ρ is the density of solution, l is the light path in the light detector, G is the number of ferric ions produced and ϵ_m is the molar extinction coefficient of ferric ions. The sensitivity range of Fricke dosimeters is in the range 40-500 Gy. Fricke dosimeters provide absolute and very precise dosimetry. As an example, a gamma irradiation facility using Fricke dosimeters for precise and reliable dose rate verification (the dose is cross-checked also with radiochromic films and alanine dosimeters) is the ISOF-CNR in Bologna where many irradiations functional to the development of new detectors and dosimeters presented in this thesis were performed. Figure 2.4 shows the dose evaluated with Fricke dosimeters accordingly to eq. 2.1 as a function of the measurement time. The evaluated dose rate of the high dose rate (HDR) irradiator was 3.33 Gy/min (5.55 rad/s).

Alanine dosimeters are another kind of chemical passive dosimeters. The basic principle consists in the production of free radicals induced by radiation in the alanine (amino acid structure). The concentration of free radicals is proportional to the absorbed dose and it can be measured by a spectroscopic technique known as electron paramagnetic resonance (EPR). The chemical structure of these dosimeters is 90%

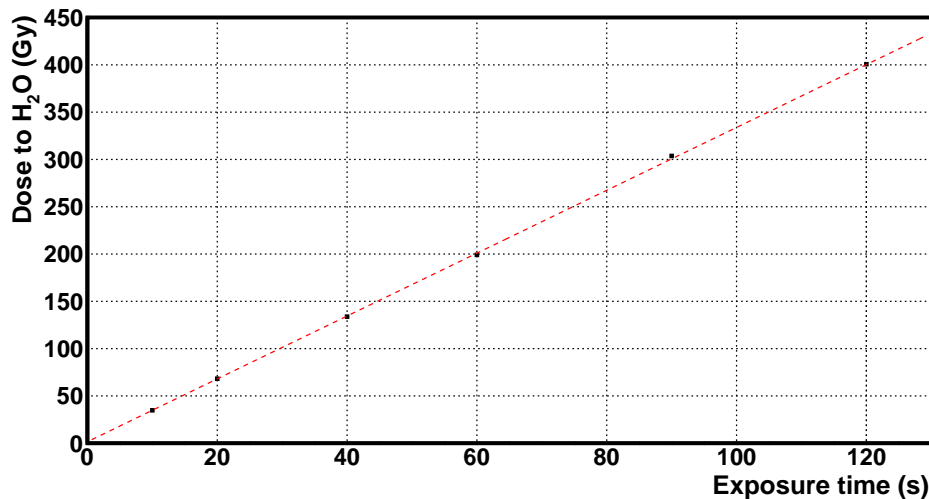


FIGURE 2.4: Determination of the dose rate of the HDR irradiator at ISOF-CNR-Bologna.

alanine and 10% paraffine wax; they are traded in small pellets of about 5 mm diameter, 2.5 mm thickness and 55 mg mass. The main application is the radiation processing, although in some cases are used, like the Fricke dosimeters, for certified dosimetry at irradiation facilities.

Radiochromic films

Radiochromic films (RCFs) are a kind of dosimeter employed in many areas of radiation physics, but their wide spread is found in medical physics. They consist in single or double layer radiation sensitive material (active layer) on one or more transparent coating. The active layer exhibit an increasing darkness with the increase of the absorbed dose. The main characteristics of commercial RCFs are discussed in detail in the next chapter, being one of the main object of studies of this thesis. RCFs are trade in the form of large size sheets (A4-like), but they can be cut, if necessary, in small pieces. The change of darkness can be related to the radiation dose by scanning the film and by evaluating the darkness. This can be done by means of commercial scanners and software of image analysis or with densitometers. The darkness can be quantified with the optical density and therefore a calibration with an a-priori known radiation field can be done. Once a set of film is calibrated, another film can be used as dosimeter and by the measurement of the optical density one can evaluate the dose. The main advantages of these dosimeters rely in the ease of handling and data analysis as well as on the the sensitivity of these films to many radiation types, energies and dose rates. Another important point is that RCFs don't need additional electronics that can be damaged in the irradiation sites.

2.4 Particle accelerators

DDD and SEE testing of electronic components is carried out at particle accelerators. Radiation induced DD in space is in fact mainly due to protons in radiation belts

and protons from solar flares. Since the DD is characterized by the NIEL (and it strongly depends on the energy of the incident particle), the DD effect on devices can be simulated by mono-energetic protons or by neutrons. In Europe there are many facilities which can provide stable proton beams. As an example, facilities supported by ESA are the *Université catholique de Louvain* (UCL) and *Paul Scherrer Institut* (PSI). Protons induce both DD and TID damage. A pure DD irradiation can be done with neutrons. However, since the amount of gamma produced in neutron facilities (e.g. reactors) is very high, the TID component due to gamma rays must be correctly evaluated. As far as SEEs, they are due mainly to protons (SPEs and GCRs), alpha particles and HZE ions (GCRs). In atmosphere, both at commercial flight altitude (11000 meters) and at sea level, SEEs are due to MeV-energy neutrons generated by interaction of cosmic rays with the atmospheric particulate (mainly reactions with nitrogen and oxygen). Since radiation inducing SEEs is a function of the LET, the available beams at particle accelerators must satisfy two conditions:

- LET values required for the intended application. In order to have more than one LET values the device can be tilted.
- The range of incident ions must be high enough to allow the interaction of particles with the device.

Figure 2.5 shows integrated circuits delided (without package) ready for irradiation with heavy ions.

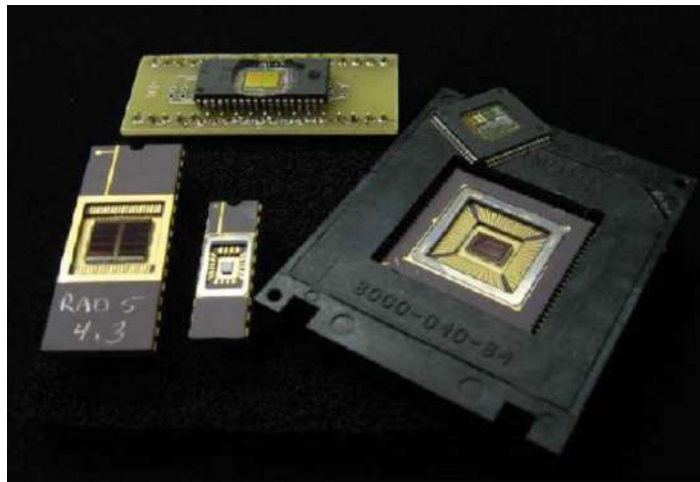


FIGURE 2.5: Integrated circuits delided (without package) ready for SEE testing with heavy ions.

UCL can provide ion beams for SEE testing as well as the RADEF facility at University of *Jyvaskyla* in Finland. These facilities are sponsored by ESA, but there are also other facilities in Europe that can accelerate ions providing a broad spectrum of LET values. Particle accelerators are of different typologies. A classification can be done in electrostatic and electrodynamic accelerators.

Electrostatic accelerators

Belong to this category the *Cockroft-Walton* and *Van de Graff* accelerators in which the accelerating electric field is provided by the high voltage stage. These accelerators can operate in tandem mode by reaching the energy according to the following formula:

$$(E = eV_{extr} + eV_t + eV_tq = e [V_{extr} + V_t(q + 1)]) \quad (2.2)$$

where V_{extr} and V_t are the extraction and terminal voltages respectively. The charge of the electron and charge state of the accelerated particles are termed in eq. 2.2 as e and q respectively. The change of charge state be achieved with a thin foil of e.g. carbon acting as a stripper. It changes the charge of the accelerated atoms from negative to positive, allowing therefore two acceleration stages. Tandem accelerators are used for applications of radiation hardness. The *Van de Graff*-tandem accelerator of Laboratori Nazionali del Sud (LNS) in Catania (figure 2.6) accelerate ions from protons to gold with intensities in the beam line from few particles per second to tens of nA.



FIGURE 2.6: Picture of the 14 MV tandem accelerator at INFN-LNS in Catania.

The maximum energy reached is limited by the maximum terminal voltage, namely $V_t=14$ MV accordingly to eq. 2.2. Some applications of radiation hardness among which the irradiation of solar cells and optical lens may be performed with proton energies of some MeV. The motivation relies in the fact that the optical instrumentation for space applications may have very sensitive surface layers, coatings or cover glasses of thickness of few microns. The influence of Earth's radiation belts on satellite solar cells is mainly determined by protons and electrons of energy approximately 1 MeV. Furthermore for some orbits the cells are exposed to integrated fluences of up to about 10^{15} electrons/cm² with energy of 1 MeV and 10^{13} protons/cm² with energies between 1 and 80 MeV (Campajola and Di Capua, 2017). The performances of these objects must be tested therefore to low energy incident radiation. As an example, the Laboratory of Accelerator of University of Napoli Federico II is equipped with a 3MV tandem accelerator. Figure 2.7 shows a picture of the 3MV tandem accelerator of University of Napoli Federico II.



FIGURE 2.7: Picture of the 3 MV tandem accelerator of University of Napoli Federico II.

It provides stable beams of light projectile particles from hydrogen up to aluminium (Campajola et al., 2005; Campajola and Brondi, 2013). The high voltage stage at the centre of the accelerating path can reach 3 MV. The ion beam intensity can reach several hundred of nA. Finally another type of low energy electrostatic accelerator which has the advantage of operating with high currents is the dynamitron. The high voltage is provided by a complex system based on solid-state power supply and radio-frequency-electrodes. Dynamitron accelerators for electrons are used also for radiation processing applications, as intense neutron source (Bannach et al., 1987) and MeV-implantation facility (Brand, 1995). These activities have been conducted at the Bochum dynamitron-tandem accelerator.

Electrodynamics accelerators

Differently from electrostatic accelerators, for which the acceleration of the particles is provided by a static element such as the high voltage terminal, electrodynamic accelerators provide the required energy to the particles in many steps. For example, a cyclotron accelerates the particles produced in the ion source (usually located in the center of the cyclotron), by means of an alternating current (radio-frequency) applied to two electrodes (dees). In the region between the dees, the particles travel circular trajectories owing to the action of a strong magnetic field. A thin carbon foil (stripper) or an electrostatic deflector allows the extraction of the energetic beam into the beam-line. The maximum energy reached by these kind of accelerators is higher with respect to that of electrostatic ones. As an example, the superconducting cyclotron of INFN-LNS in Catania can accelerate ions up to uranium of energies up to 80 MeV/u; the Proton Irradiation Facility (PIF), the PSI beam-line dedicated to irradiation of electronic devices, provides protons of initial energies of 230, 200, 150, 100 and 74 MeV. However, if a reduced energy is needed, absorber materials of suitable thickness may be used. Compact medical cyclotrons for radioisotope production are generally limited in maximum energy by the specific applications. For

example, the Bern medical cyclotron, an IBA 18/9 cyclotron (Braccini, 2017), delivers protons of 18 MeV energy and deuteron of 9 MeV for the production of the isotope ^{18}F for Positron Emission Therapy (PET) imaging. Since a significant part of the experimental activities (mainly that related to neutron production) discussed in this thesis were performed at the Bern medical cyclotron, it is considered appropriate to present the physical principles of cyclotrons by taking it as example.

The Bern medical cyclotron

The cyclotron facility of the University of Bern is equipped with an IBA 18/18 Cyclone. It can accelerate H⁻ ions of energy 18 MeV (Braccini, 2017). Figure 2.8 shows a picture of the cyclotron during a maintenance session. The picture points out the

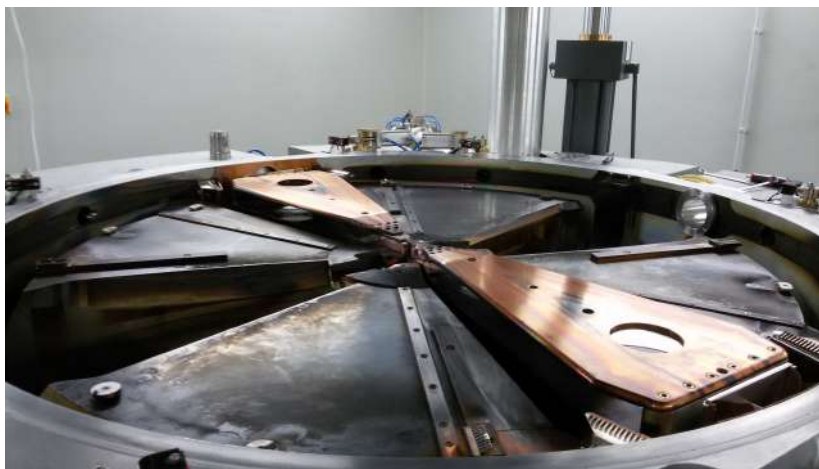


FIGURE 2.8: The 18/9 IBA Cyclone of University of Bern.

detail of the two dees connected to an alternating current source consisting in a 42 MHz radio-frequency (RF) generator. This frequency corresponds to the second harmonic for protons and the fourth for deuterons. The negative ions are generated in a Penning Ionization Gauge (PIG) source placed in the center of the cyclotron. The ions extracted from the source by an electric field connected to the RF of the cyclotron are so accelerated towards the dees. Once the ions of mass m , charge q and velocity v enter the region between the dees at a radius ρ , they experience only the magnetic field B according to the formula:

$$\rho B = \frac{mv}{q} \quad (2.3)$$

When the ions leave the dees, their polarity reverse so that the ions are accelerated again. Since the orbit radius is proportional to the speed of the ion (eq. 2.3), the ions spiral outward towards the border of the magnetic field. The ion gets a final energy which is equal to the sum of all individual accelerations in the gaps between the dees. The extraction is obtained by stripping the negative ions with a $5 \mu\text{m}$ thick pyrolytic carbon foil with an high efficiency of about 100%. The radial position of the stripper determines the extraction energy. The Bern cyclotron is the central component of the SWAN project, a combined centre both for ^{18}F -production

and research studies (Auger et al., 2016b). In particular, the night activity of the cyclotron consists in the production of ^{18}F -isotope, necessary for the synthesis of fluorodeoxyglucose to be used in positron emission therapy (PET) imaging. During the day, different research activities are carried on, among which the production of new radioisotopes for medical applications (Carzaniga et al., 2017), the development of new beam diagnostic apparatuses (Auger et al., 2016a; Nesteruk et al., 2018) and detection techniques (Anders et al., 2018). To make this possible, an external 6.5 m long beam transport line (BTL) was installed with two quadrupole doublets, two beam stoppers, a neutron shutter, a collimator and X/Y steerers. Some of such compact medical cyclotrons have installed a beam-line dedicated to research studies and irradiations for radiation hardness applications. In addition to the Bern cyclotron, another IBA 18/9 cyclotron operating for these purposes is the cyclotron in CNA in Sevilla. The IBA company produces also cyclotrons for proton-therapy applications. It is an example the Trento Proton Therapy facility which can accelerate protons up to a maximum energy of 228 MeV. All these accelerators can be exploited for irradiation of materials and electronics.

Accelerators for industrial irradiation

Finally, accelerators used mainly for industrial irradiation (radiation processing, sterilization and flue gas treatment) are the high-power LINAC ILU series accelerators. Figure 2.9 shows a picture of the terminating part of the ILU-6 LINAC accelerator of Warsaw. This 20 kW-127 MHz accelerator provides few MeV electrons



FIGURE 2.9: Picture of the ILU-6 LINAC accelerator in Warsaw.

with very high dose-rate up to about 10^6 Gy/s.

2.5 Charged particles detectors

In this section the main detectors and dosimeters commonly employed at charged-particle facilities are discussed.

Parallel plate ionization chambers

Parallel plate gas-filled Ionization Chambers (ICs) used in transmission mode are commonly used at particle accelerators. The high voltage electrode of these chambers is usually made of thin plastics such as kapton or mylar with a metallic coatings. The polarization voltage depends on the reduced field (i.e. the ratio of electrical field and pressure E/p) and it is usually of the order of hundreds of volt. The acquisition of electrical signals produced within the sensitive volumes of ICs by the particle beam allows, after proper calibration and analysis, measurements of flux in real-time and therefore integral measurements of fluence and dose.

Faraday cup

A Faraday cup (FC), which a picture is shown in figure 2.10 is a metallic cup of thickness designed for stopping the incident energetic charged particles.



FIGURE 2.10: Picture of a Faraday cup (a), a Bicon scintillator (b) and parallel plate avalanche counter (c) used for the evaluation of fluence in irradiations with charged particles.

The FC is connected to a sensitive ammeter (such as a pico-ammeter) and therefore the charge accumulated gives a measurement of the fluence rate. Such a measurement is more accurate as the better the FC is designed. In fact current from external secondary electrons or secondary electrons generated within the cup can distort the measurement. As a result, electrostatic and magnetic fields are often used to suppress these contributions. Faraday cups do not provide absolute real-time monitoring of the fluence rate being invasive instruments; they are usually remotely controlled and inserted in position with the beam for performing the measurements. Once the measure is done, they are removed from the beam-line. FCs are intensively employed for beam diagnostics and also for reference measurements before the irradiation. FCs usually operate in vacuum although FCs to be used for irradiation in air can be designed. For instance, the FC shown in figure 2.10 works in air.

Scintillators

In addition to ionization chambers, thin plastic scintillators are employed as particle counting monitors. These instruments can be put either in the position of the DUT for calibrating other detectors such as ICs (the last to be used during DUT irradiation) or can provide real-time fluence rate monitoring during the actual DUT irradiation. The excellent timing performances allow particle detection within few ns

(signal fall time). The read-out of these detectors is generally carried out by means of photomultiplier tubes (PMTs), avalanche photodiodes or silicon photomultiplier (SiPM). Figure 2.10 shows a picture of Bicron plastic scintillator employed for the monitoring of flux for irradiations of electronic devices.

Parallel plate avalanche counters

For very low dose rate tests (up to 10^6 - 10^7 particles/s) both specific designed ICs and position-sensitive Parallel Plate Avalanche Counters (PPACs) can be used. The latter provide a response which is similar to that of ICs in pulsed mode with a better spatial resolution. Like ICs, the PPAC detector consists of two parallel thin electrode films filled with a proper gas such as isobutene (C_4H_{10}) and perfluoropropane (C_3F_8). The interaction of ionizing radiation with the gas triggers a *Townsend* electron avalanche. Owing to the high mobility of electrons, to the reduce field applied and to the low dimensions of the PPAC, the resulting signals have excellent timing properties (with fall times of a few nanoseconds). This increases the sensitivity of PPACs to low intensities. The information on the position of the particles interacting with the PPAC, can be evaluated by reading the signals on the strips. Figure 2.10 shows a picture of PPAC used for determining the flux and position of heavy ions for low-intense irradiation for studying SEEs.

Films and phosphor screens

RCFs are considered a suitable tool for radiation hardness and industrial applications (McLaughlin et al., 1988; Butson, Cheung, and Yu, 2004). They are reliable and non-invasive dosimeters. RCFs can be easily positioned in front of (or in the very proximity) of the DUT during an irradiation with a particle beam providing therefore the knowledge of dose directly on the DUT. In many applications RCFs are used also for centering the beam. This operation is necessary for a correct irradiation and can be done also by means of other kinds of detectors that change color with ionizing radiation. In alternative phosphor screens can be used. Being fluorescent materials, phosphor screens exhibit an immediate effect which is interrupted once the beam is stopped. Contrariwise, RCFs show permanent coloration after irradiation. This aspect is an advantage for certify the dosimetry.

2.6 Techniques of dosimetry monitoring on the DUT

The precise monitoring of the dose on a device under test (DUT) exposed to charged particle radiation is a quite complex issue. In order to ensure the demanded characteristics in terms of e.g. of LET, flux, fluence, spatial uniformity and resolution accurate measurements must be performed. To achieve this purpose, in many cases, more than one detector is needed. This section discusses the radiation detection techniques designed and implemented by our research group for accurate dose measurement on the DUT. As example, the detection techniques set-up for irradiations of devices at *Paul Scherrer Institute* (PSI) and CNA-Sevilla are discussed.

Irradiation at Paul Scherrer Institute

Figure 2.11 shows the beam line of the Proton Irradiation Facility (PIF) at PSI. In this

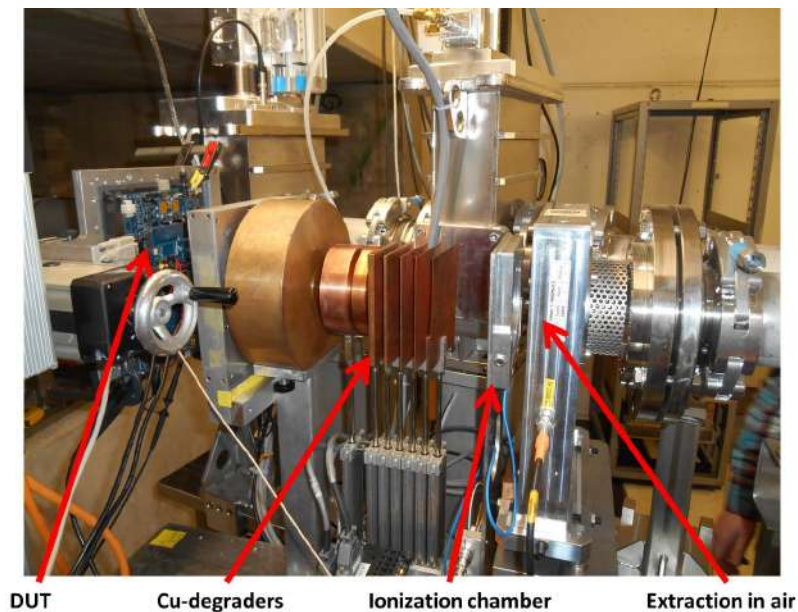


FIGURE 2.11: Irradiation of an electronic device at Proton Irradiation Facility of PSI in Switzerland.

irradiation the beam was extracted in air. An ionization chamber, shown in figure 2.11, provided measurements of the beam flux. It should be noticed that, for some specific irradiations, the initial energy was reduced by copper degraders. This was done because the energy needed for that specific irradiation was 15 MeV (less than the minimum energy available at PSI). In addition of the slowing down of the incident proton energy, the effect of air and copper degraders consist in the spreading of the beam (energetic and spatial straggling). The characteristics of the original beam are definitely modified and the definition of relevant physical quantities like energy and fluence on the device position is lost. This ultimately affects the evaluation of dose. The technique employed for assessment of dose on the DUT consisted in performing a previous irradiation with a Bicron scintillator placed in the position of the DUT. As a consequence, the ionization chamber was calibrated with the counts recorded by the scintillator. As further control, a RCF was used for centering the beam and measuring the dose profile.

Irradiation at CNA-Sevilla

Irradiation of devices were performed at the IBA 18/9 cyclotron of CNA at Sevilla. Figure 2.12 shows the irradiation room of CNA in Sevilla.

The beam was extracted in air. Since the energy required on the device was 10 MeV, the initial 18 MeV energy was reduced by means of an extraction window and by a further 500 μm aluminum degrader. After extraction in air, the proton energy was 14.2 MeV with an energy straggling of 100 keV and a lateral spread of 2.6 mm. Figure 2.13 shows the output of a TRIM simulation of an incident 14.2 MeV interacting with 1 meter air.



FIGURE 2.12: Irradiation of an electronic device at the IBA 18/9 cyclotron of CNA in Sevilla.

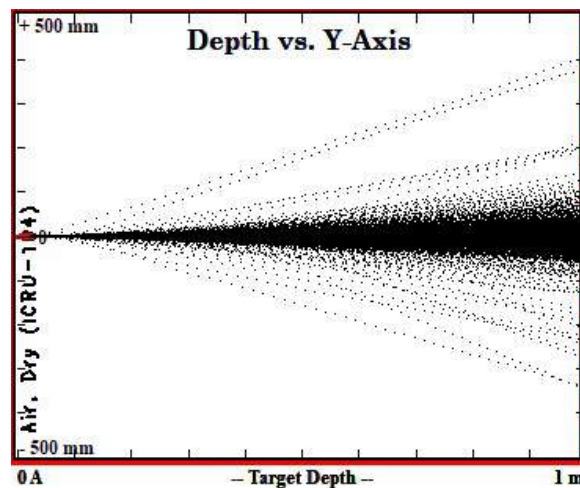


FIGURE 2.13: TRIM simulation of an incident 14.2 MeV proton beam interacting with 1 meter air. The lateral spread is 2.6 mm with an energy straggling of 300keV.

The technique used in this irradiation for the evaluation of the fluence (and therefore of the dose) on the device used the reading of the current on collimators. A first irradiation was performed with a FC in the position of the DUT. The ratio $R = \frac{I_1}{I_2}$ of the currents I_1 and I_2 measured on two collimators is proportional to the FC current. So it is possible to establish a calibration of R vs. I_{FC} . Once the DUT is placed in the same position of the FC with the two collimators in-line, the evaluation of the ratio R allows precise evaluation of the dose on the DUT. A conceptually similar method, more compact, was recently developed for radiation hardness applications at the 18/18 IBA cyclotron of University of Bern (Anders et al., 2018).

2.7 Rutherford Backscattering Spectroscopy

An innovative powerful method for the monitoring of the dose on DUT was recently designed and implemented by our research group for a series of irradiations of devices at the tandem accelerator of University of Napoli Federico II. The accelerator laboratory (Campajola and Brondi, 2013) is equipped with several beam lines including one for educational activities and nuclear physics (Casolaro et al., 2018), one for radiobiology applications (Manti et al., 2012), one for neutron experiments (Vardaci et al., 2016) and one dedicated to ionic implantation and irradiation of devices. *Rutherford Backscattering Spectroscopy* (RBS) activities were carried out at the tandem accelerator both for research purposes (Raulo et al., 2012) and for educational ones (Casolaro et al., 2018). High precision irradiation of devices were carried out by extracting the ion beam in air across a $5\ \mu\text{m}$ mylar window. As an example of the innovative detection technique, we report here the case of implantation of 6 MeV ^4He ions in silicon wafers. The Si-wafer was mounted on a metallic frame controlled by a X-Y-Z stepper motor, ensuring sub-millimeter precision in the positioning and centering of the wafer. Figure 2.14 shows the implantation beam line with a scattering chamber, the frame for devices irradiation and a FC.

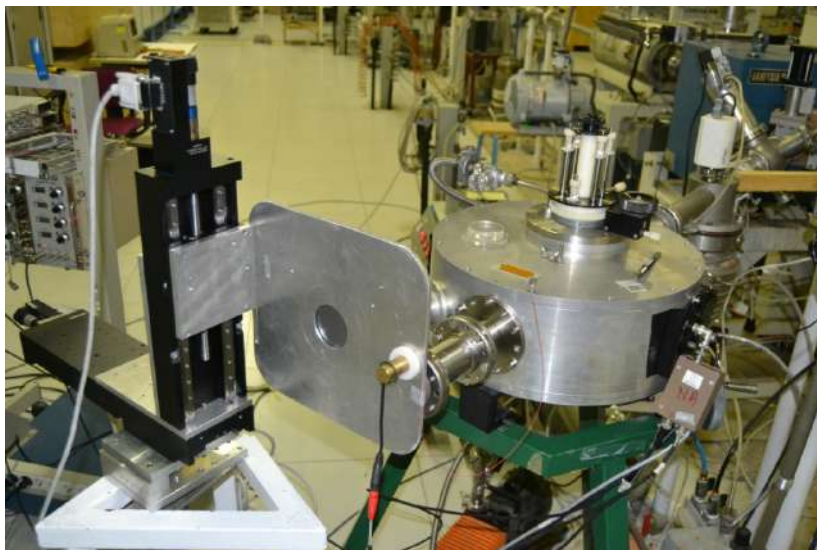


FIGURE 2.14: Beam line of the tandem accelerator of University of Napoli Federico II dedicated to implantation and irradiation of devices. it is equipped with a scattering chamber and a frame for devices.

As discussed in the previous section, the FC measure gives the reference value for other dosimeters and detectors. The new technique of dosimetry monitoring uses:

- The X-Y-Z stepper motor for sub-millimeter control of the position of the device.
- A thin foil of a pure element placed in the center of the scattering chamber.
- A silicon surface barrier detector (SSD).

- A tungsten wire.
- The Faraday Cup.
- Radiochromic films.

Figure 2.15 shows the schematic of the monitoring system employed for implantation of 6 MeV ^4He ions in silicon wafers.

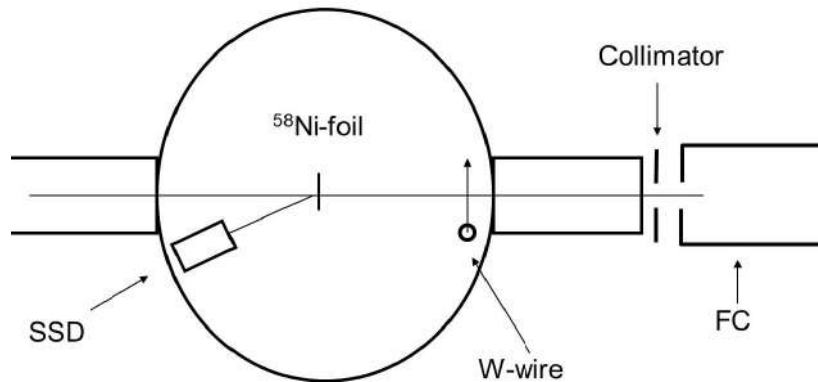


FIGURE 2.15: Schematic of the dosimetry technique employed at University of Napoli for the on-line monitoring of the dose in the experimental position

A $500 \mu\text{g}/\text{cm}^2$ ^{58}Ni foil is placed in the center of the scattering chamber, kept under vacuum (10^{-5} mbar). The energy lost by ^4He ions in the foil is 400 keV. After crossing the ^{58}Ni -foil, a moving tungsten wire provides measurements of beam current and profile. After extraction in air, the beam defined by a collimator, enters in the FC which gives the reference current. The SSD was positioned at a backward angle (in this case 160 degrees) with respect to the ^{58}Ni -foil. The ^4He ions backscattered by the ^{58}Ni -foil have 4.4 MeV-energy. The SSD detector shows a peak in the spectrum corresponding to this energy. The evaluation of the integral of the peak gives precise measurement of the flux of particles. The RBS counting and the X-Y-Z values of the position of the DUT (provided by the stepper motor), are acquired in real-time during the irradiation. A computer provided the report of these information giving as result the imposed fluence as a function of the position. In case of beam instabilities such as black-out or shut-down, this system allows corrections of the fluence delivered to the device. Further measurements of the beam uniformity were carried out by means of a RCF. Figure 2.16 shows the terminating part of the beam-line with the frame for device irradiations and the RCF for uniformity checking.

The uniformity was verified in X and Y axis and found to be better than 1%. Figure 2.17 shows the darkening profiles of RCF in X and Y axis.

This method allows high precision (overall uncertainty less than 1%) assessment of dose with four independent measurements (SSD in backscattering, tungsten wire, FC and RCFs) and a X-Y-Z stepper motor for the positioning of the device. Since the efficiency of the SSD detectors is 100% and its response is independent of the incident ion, this method results reliable and useful beyond that accurate and precise for many applications. This method will be discussed in detail in a separate publication.



FIGURE 2.16: Picture showing a RCF for measurements of the beam uniformity.

Discussion

Dosimetry for proton and heavy ions irradiations of electronic devices is not an easy task. In this and previous section of this chapter it was emphasized that in many cases one or more detectors, a dosimeter or a current monitor is used for the evaluation of the dose delivered on the DUT. There is no standard dosimetry procedure and each single test must be studied in detail for setting-up reliable dosimetry apparatuses. The lack of standard procedures relies also in the fact that RHA tests require radiation of different type, energy and dose range.

2.8 Neutron sources

The study of neutron damage of electronic devices require tests with well characterized neutron sources. The study of neutron-induced SEEs (avionic and terrestrial applications) and displacement damage effects (mainly space applications) can be accomplished by performing tests with fast neutron, although also thermal neutrons are a concern. A continuous neutron spectrum (white spectrum) with shape similar to the atmospheric one well reproduce the actual neutron environment. On the other hand, mono-energetic neutrons are fundamental for detailed studies of the energy dependence of the neutron damage mechanism. The availability of such neutron sources is limited. In the following a brief review of the main neutron sources is given.

Neutron production from reactors and radioactive nuclei

Thermal neutrons (0.025-1 eV) can be produced either from nuclear fission reactors by moderation of fast neutrons with low-Z materials such as polyethylene, water, paraffin, etc . The neutron flux in the proximity of the fission reactor nucleus reaches values of 10^{14} neutrons/($cm^2 \cdot s$). Fast neutrons can be produced by means of either

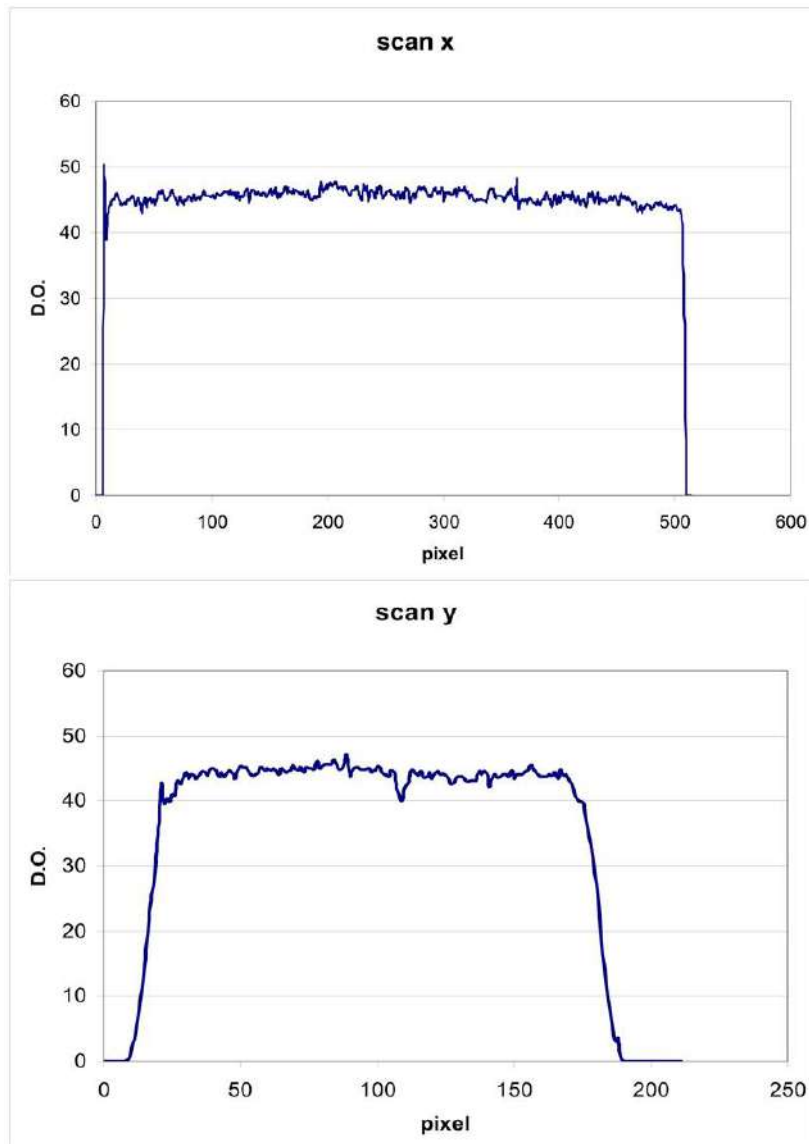
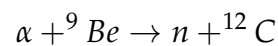


FIGURE 2.17: Uniformity profiles in X and Y axis measured with radiochromic films.

radioactive α -emitters or charged-particle accelerators by bombarding suited materials. For example, the reaction



has high neutron production cross-section (488 mbarn) for 5 MeV α -particles. This is due to the relatively low binding energy of 1.65 MeV of the less bound neutron of the ${}^9\text{Be}$. As a result, long half-life α -emitters such as ${}^{241}\text{Am}$ (43 2.2 y), ${}^{239}\text{Pu}$ (24.1 y) and ${}^{226}\text{Ra}$ (1600 y) can be used for generation of neutrons with a steady production rate of about $2\text{-}3 \cdot 10^6$ neutrons/(Ci·s). The resulting energy spectrum is not monoenergetic because of the energy loss by α -particles in the radioactive matrix and excitation of the residual nucleus ${}^{12}\text{C}^*$. Fissile elements such as ${}^{252}\text{Cf}$ (2.6 y) produce MeV-energy neutrons. The energy spectra of the ${}^{241}\text{Am}$ - ${}^9\text{Be}$, ${}^{239}\text{Pu}$ - ${}^9\text{Be}$ and

^{252}Cf neutron sources are reported in figure 2.18 (Baumann and Smith, 2000).

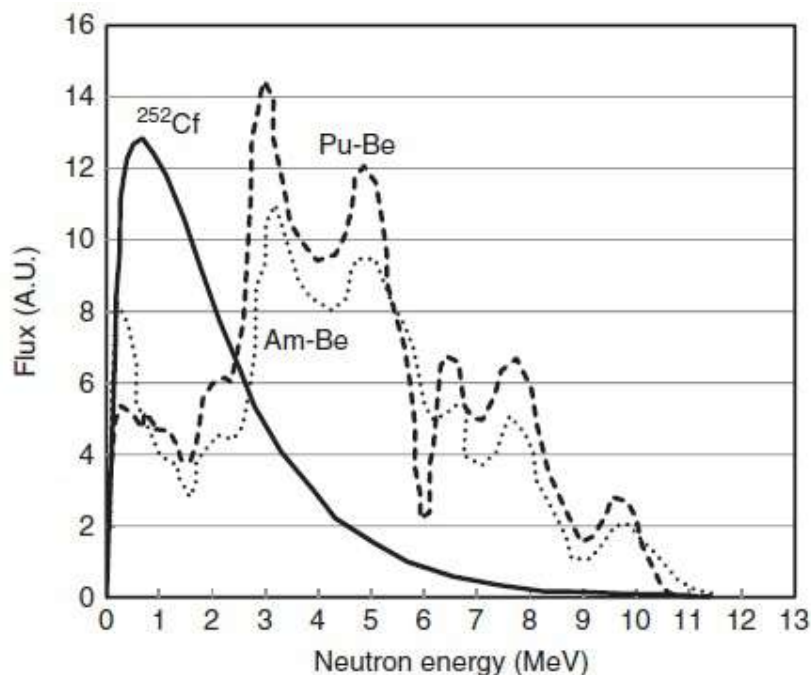


FIGURE 2.18: Energy spectra of the most common radioactive materials.

Since the energy of α -particles emitted from the ^{241}Am and ^{239}Pu isotopes is ~ 5 MeV, the corresponding neutron energy spectra have similar shapes with peaks of 3 and 5 MeV. The ^{252}Cf neutron spectrum has the typical *Maxwell-Boltzmann* trend with a main peak of 1 MeV and a tail up to 11 MeV. The fission is always accompanied by emission of HZE fission-fragments, α -particles and γ -rays. The production rate is $4 \cdot 10^9$ neutrons/(Ci·s). Neutron photo-production can be achieved with gamma rays of energy greater than the binding energy of the less bound neutron of the target material. As far as (γ, n) reactions, the corresponding neutron energy is more defined (near to monoenergetic) compared to that of α -emitters. For example, the ^{24}Na isotope (15.0 h) emits a gamma ray of 2.8 MeV and produce a neutron energy peak of 1 MeV after interaction with ^9Be .

Atmospheric-like neutron spectra

Particle accelerators are a powerful instrument for production of neutrons. The most common nuclear processes employed for neutron production are spallation and binary reactions. When a high energy incident particle, such as proton of 1 GeV, collides with a heavy nucleus (e.g. tungsten), a strong nuclear reaction takes place with emission of 20-30 neutrons/proton. The theoretical model for the spallation represents this process in two steps: first projectile-nucleons collision with overall excitation of the compound nucleus, then its de-excitation with emission of light particles (protons, deuterons, gamma rays and α particles). Neutrons produced by spallation are often driven by a pulsed proton accelerator. As a result, the measurements of neutron spectra can be achieved by means of time of flight (TOF) detection

technique. Otherwise accurate measurements of neutron spectra are very difficult to perform. Spallation-based neutron sources provide atmospheric-like (or $1/E$) neutron spectra with fluxes up to 10^6 - 10^7 neutrons/($cm^2 \cdot s$) higher than the flux of the cosmic-ray-induced neutrons, allowing therefore device testing at accelerated rates. The number of such facilities in the world equipped for device testing is very limited compared to the requirements from industry and research. Figure 2.19 shows the sites of these facilities.

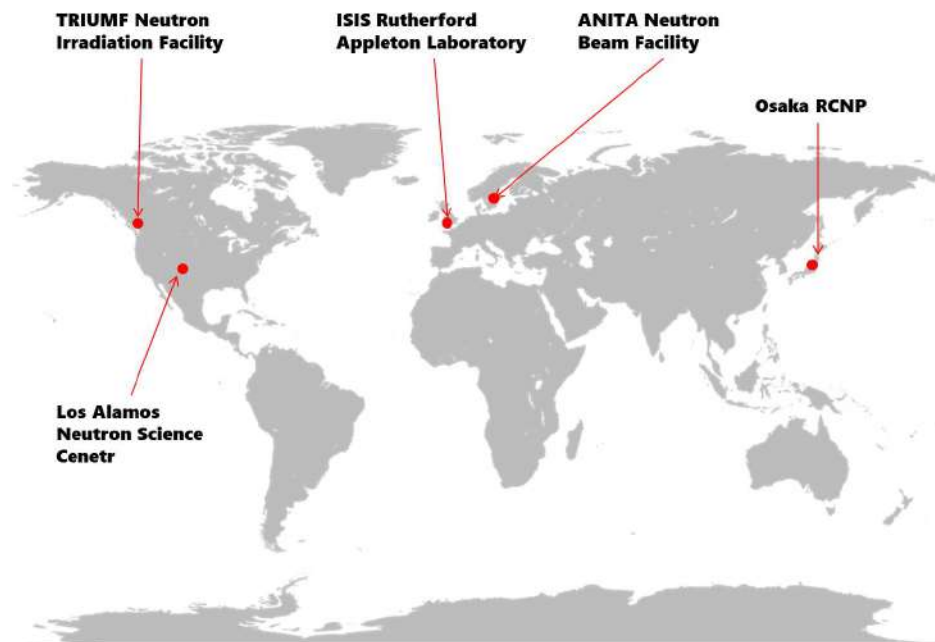


FIGURE 2.19: Neutron induced SEE testing facilities.

For example, the *Los Alamos Neutron Science Center* (LANSCE) provides a high-energy and a low-energy neutron source for semiconductor testing (Nowicki, Wender, and Mocko, 2017). The high-energy neutron source uses an 800 MeV pulsed proton beam with current up to some μA on tungsten target (spallation). The corresponding atmospheric-like neutron spectrum span over a wide range from hundreds of keV to the incident proton energy (800 MeV). A viable alternative to the testing of devices with a white spectrum relies in performing the tests with mono-energetic neutrons, allowing also to fix any issues of energy dependence.

Mono-energetic neutrons

A convenient and powerful way to produce mono-energetic neutrons consist of using two-body reactions induced by accelerated charged particles. A pure mono-energetic field consists of a single-line spectrum with an energy width much less than the energy itself. In the practice such a field is difficult to obtain and is limited in energy up to some MeV. Most of the two-body reactions are in fact purely mono-energetic in the range from tens to hundreds of keV (Drosg, 1999). Furthermore, in many applications such a spectrum with one single energy line is not fundamental. The term "quasi-monoenergetic" is used for more realistic cases where the neutron spectrum includes a second discrete group of neutrons resulting from

TABLE 2.2: Q-values and threshold energies of most important two-body reactions for mono-energetic neutron production.

Reaction	Q-value (MeV)	E_t (MeV)
$D(d,n)^3He$	3.269	0.
$D(d,n)^3He$	17.589	0.
$T(p,n)^3He$	-0.763	1.018
$^7Li(p,n)^7Be$	-1.644	1.810

break-up reactions or from neutron emission via excited states (Nolte and Thomas, 2011). There are many two-body reactions that can be used for the production of mono-energetic neutrons. The choice of one rather than another depends on several factors including the incident particle, its energy, the availability of the targets and nevertheless the production rate. The four most important two-body reactions for mono-energetic and quasi-mono-energetic neutron-production involve light projectiles and light targets. These reaction, their Q-values and energy threshold E_t (MeV) are summarized in table 2.2.

The excitation functions (cross section as a function of the energy) are shown in figure 2.20.

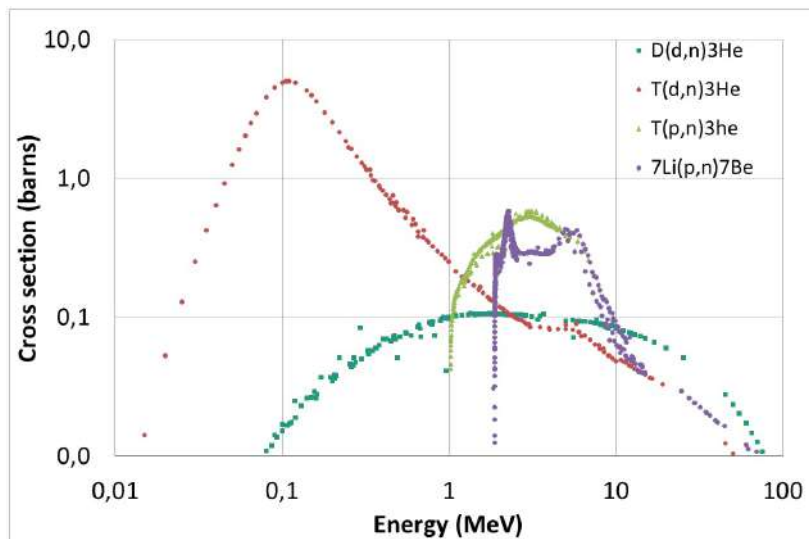


FIGURE 2.20: Excitation function of the most important two-body reactions for the production of mono-energetic neutrons. Data are

The measured data are taken from the *National Nuclear Data Center* (NNDC) database (Tuli, 1996). The facilities that produce mono-energetic and quasi-mono-energetic neutrons are based on these reactions. For example, in Italy the *Frascati Neutron Generator* (FNG) uses tritium as target for production of 14 MeV neutrons with a rate of 10^{11} neutrons/s (Martone, Angelone, and Pillon, 1994). It uses also deuterium for the production of less energetic neutrons of 2.5 MeV. However, the tritium-based neutron facilities are limited in number because of the availability of tritium. Particle accelerators for mono-energetic neutron production are mainly

based on $D(d,n)^3\text{He}$ and $^7\text{Li}(p,n)^7\text{Be}$ reactions. In addition to the employment of particle accelerators, there is also a portable neutron generator based on deuterium-deuterium plasma which produce mono-energetic neutrons.

2.9 Neutron detection

Neutrons interact with matter only with the atomic nucleus which linear dimensions are of the order of $\sim 10^{-15}$ cm. As a result, the neutron detection is possible if neutron-induced nuclear interactions take place. The main physical processes on which neutron detectors are based are the following:

- (n,n) elastic scattering
- (n,γ) radiative capture
- (n,n') inelastic scattering
- (n,α) , (n,p) , (n,d) ... two-body reactions with emission of light particles
- (n,f) fission

Depending on the incident neutron energy, one or more of these physical processes is dominant and can be exploited for the detection.

Thermal neutrons

As an example, isotopes such as ^3He , ^{10}B and ^6Li have high cross section of production of charged particles by two-body reactions for incident thermal energies. Figure 2.21 shows the cross section of some physical processes used for neutron detection as a function of the neutron energy.

In particular, reactions as

- $^{10}\text{B}(n,\alpha)^7\text{Li}$ ($Q=2.8$ MeV)
- $^{10}\text{B}(n,\alpha)^7\text{Li}^*$ ($Q=2.3$ MeV)
- $^6\text{Li}(n,\alpha)^3\text{H}$ ($Q=4.8$ MeV)
- $^3\text{He}(n,p)^3\text{H}$ ($Q=9.8$ MeV)

have cross section of the order of 10^3 barn for incident thermal energies (figure 2.21). The ejectiles of these reactions can be detected providing the signals of neutron interaction. The ^3He proportional counters have the special feature that gas and converter are the same material. Moreover, the signals are due by keV proton recoils, allowing neutron spectroscopy. The BF_3 neutron detectors are proportional counters filled with the gas BF_3 . The energy of the neutron reaction with BF_3 is higher than for ^3He , allowing better discrimination against gamma radiation. However these detectors are less sensitive than ^3He . BF_3 -based neutron detectors can be designed as proportional counters with Boron in the form of a solid coating on the inner walls of the tube. This allows the filling of the detector with a standard gas, a mixture or

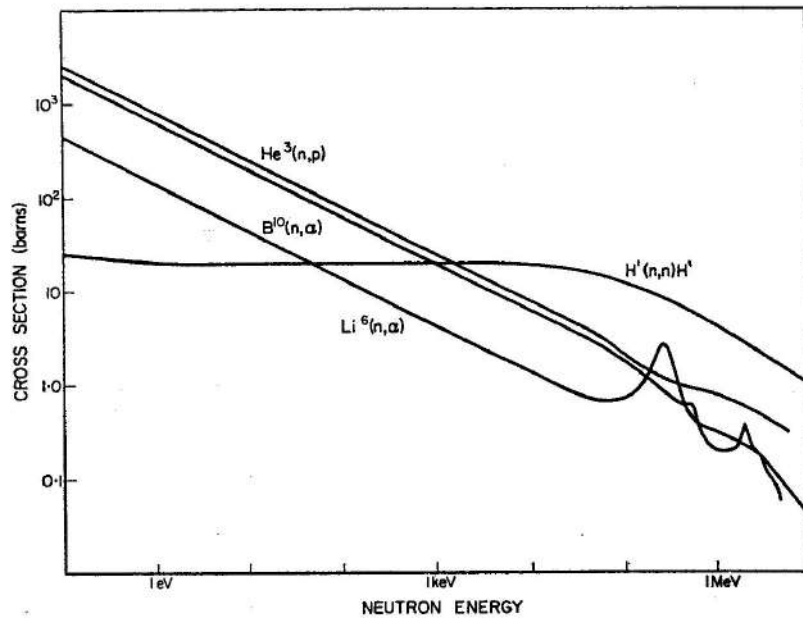


FIGURE 2.21: Comparison between cross section of reaction producing charged particles and (n,p)

a noble gas, able to detect the alpha particles emitted by Boron. These detectors are commonly used in many applications such as thermal neutron diffraction, neutron spectroscopy, mixed waste monitoring, soil moisture detection and monitoring of nuclear reactors (operating at low power).

Fast neutrons

The detection of fast neutrons can be achieved by slowing-down the fast neutron flux up to thermal and epi-thermal energies and by detecting the moderated neutrons with the techniques described above. The drawback of this method relies in the lost of any spectroscopic information of the original neutron field. Many detectors and dosimeters for fast neutrons are based on the moderation of the original beam. An example are spherical dosimeters and long-counters using BF_3 or ^3He as sensitive element surrounded by large volumes of moderating material. Figure 2.21 shows also the cross section of the elastic scattering $^1\text{H}(n,n)^1\text{H}$ which is significantly high from some keV on wards compared to other reactions used for neutron detection. Considering an elastic collision between a neutron of energy E and a target nucleus (at rest) of atomic number A , the conservation of energy and momentum gives the energy E' of the neutron after the elastic scattering:

$$\frac{E'(\vartheta)}{E} = \frac{A^2 + 2A + 1 \cos \vartheta}{(A + 1)^2} \quad (2.4)$$

where ϑ is the scattering angle in center of mass. From eq. 2.4, the condition of central collision ($\vartheta=180$) implies the maximum energy loss, that is:

$$\frac{E'(\vartheta = 0)}{E} = \frac{(A - 1)^2}{(A + 1)^2} = \alpha \quad (2.5)$$

The energy loss by an incident neutron is maximum for hydrogen ($E'=0$) and decreases as the atomic number decrease. As a result, materials rich of hydrogen and low-Z elements such as polyethylene, paraffin, water and concrete, among the others are commonly employed for the design of shielding for fast neutrons. Based on the same principle, organic scintillators are used for design of fast neutron detection. These detectors have high cross-section for (n,p) elastic scattering, high counting rate and can be made in large volumes allowing good detection efficiency. The output pulse is generally fast resulting in high resolution for time-of-flight (TOF) detection technique. The gamma-neutron discrimination with organic scintillators can be made by means of Pulse Shape Discrimination (PSD) techniques. Since the main physical process of interaction of fast neutrons with hydrogenate materials is the (n,p) scattering, the theoretical response of an organic scintillator (due to the signals of recoil protons) is rectangular in energy (eq. 2.4 and 2.5). However, the actual response has not rectangular-shape because the light output H of charged particles is not linear with respect to the energy deposited in the scintillator, being approximately proportional to (Knoll, 2010):

$$H \propto E^{3/2} \quad (2.6)$$

The derivative of eq. 2.6 with respect to the energy gives:

$$dH/dE \propto E^{1/2}$$

Therefore the rectangular theoretical spectrum changes being proportional to $H^{-1/3}$:

$$dN/dH \propto H^{-1/3}$$

These results are shown in the plots of figure 2.22.

If the range of the recoil protons is large compared with the detector dimensions, some recoil protons can escape from the surface of the scintillator. Such an event is not lost, resulting in a shift to the lower energies. Finally, the detector resolution affects the tail of high energy of the spectrum. The typical experimental spectrum obtained for fast neutron detection with organic scintillators is shown in figure 2.23.

For these reasons, the neutron spectroscopy is particularly difficult to perform with a neutron scintillator. Excellent spectroscopy information are usually provided with TOF apparatus, in which the start signal can be given e.g. by the beam (if pulsed) and the stop by a neutron scintillator. The TOFs are related to the energy of the particles and therefore energy spectra can be easily obtained by TOF spectra. Moreover, the neutron-gamma discrimination is ensured with TOF detection technique. However, since the TOF apparatus require long distances between start and stop detectors (several meters for MeV energy neutrons) these are not always easily installed in beam facilities. As a consequence, organic scintillators are used also as neutron counters, once their efficiency is known.

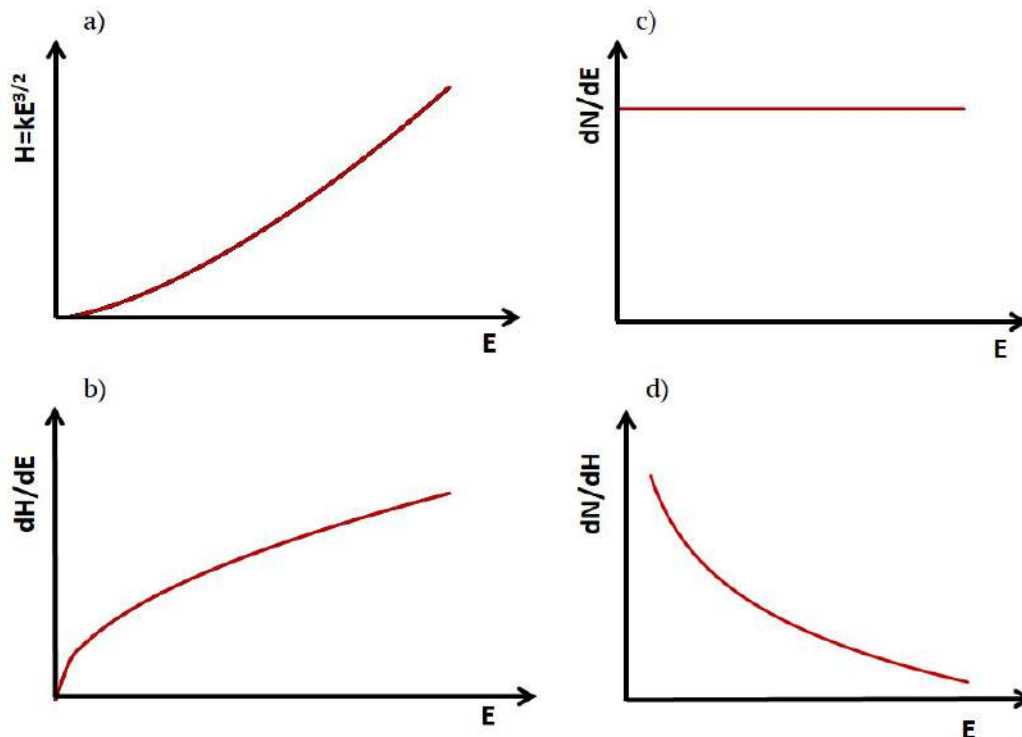


FIGURE 2.22: The light output of an organic scintillator is given by eq. 2.6 which curve is shown (a). The calculation of its derivative with respect to the energy (b) allows to predict the theoretical shape of the light output. The figure show the distortion from the rectangular spectrum (c) into that shown in (d).

Pulse shape discrimination

Pulse shape discrimination (PSD) techniques allow the identification of the particle incident on a neutron detector from the analysis of the shape of signals. The difference in the shape relies in the nature of the interaction processes of neutrons and gamma with scintillators. The signals produced by neutrons are due to the recoil protons that excite the molecules in the scintillators, which decay by fluorescence. Gamma ray interactions in organic scintillators produce Compton electrons. The scatter recoil protons have a short range, a high LET, and generate a high concentration of triplet molecular states. By contrast, electrons have a longer range than protons (their track is less localized compared to protons) and generate a lower concentration of triplet states and a higher of singlet states. The last decay by prompt fluorescence with decay time of some ns. Triplet states decay by delayed fluorescence with decay time of hundreds of ns. The variation in the amount of light produced by delayed fluorescence can be used to identify the incident particles (Zaitseva et al., 2011). Figure 2.24 shows the different light pulses produced by neutrons, gamma rays and alpha particles in a organic scintillator.

Several analog PSD methods have been developed in the years The most often used for neutron-gamma discrimination are the rise time method, the zero-crossing method and charge comparison method (Ranucci, 1995). Digital methods such as the patten recognition method are also employed (Takaku, Oishi, and Baba, 2011). In

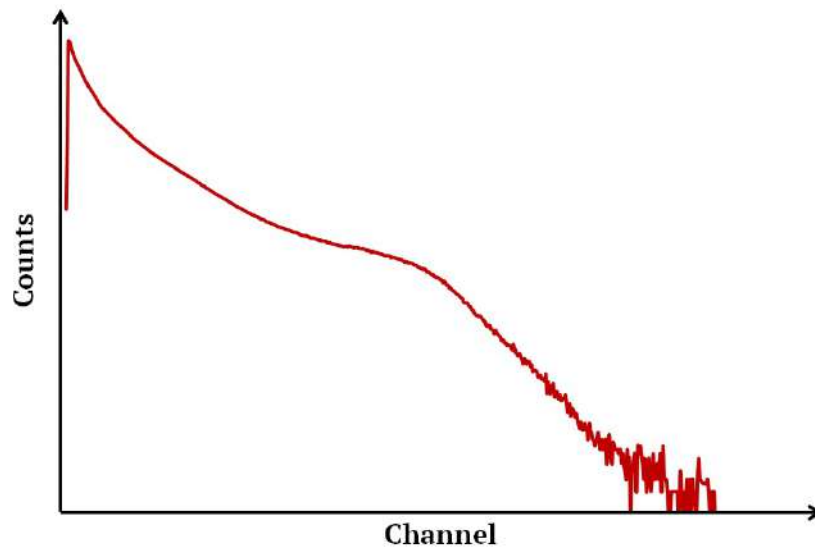


FIGURE 2.23: Experimental neutron spectrum measured with an organic scintillator.

this thesis the charge comparison method was used for PSD of neutron and gamma signals obtained with the polysiloxane neutron scintillator. This topic is discussed in chapter 5.

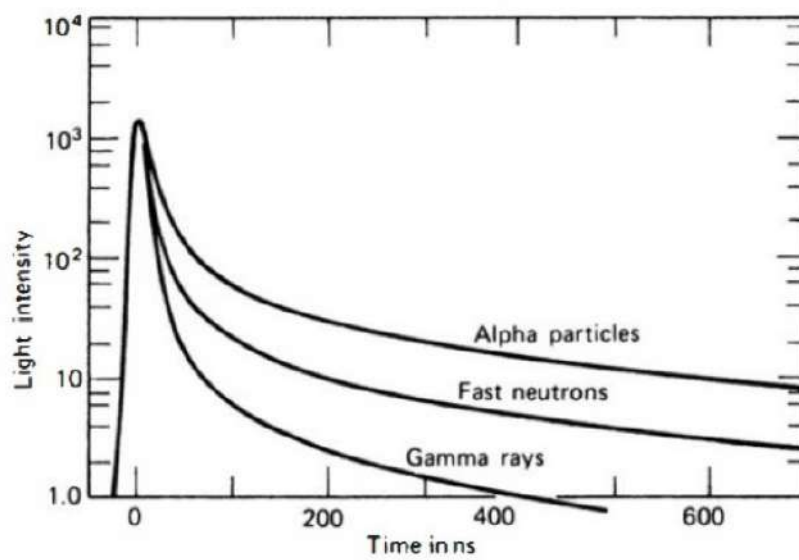


FIGURE 2.24: Different response of organic scintillators to gamma rays, neutrons and alpha particles.

Chapter 3

Radiochromic films

Radiochromic (RCFs), based on the property of modifying the structural characteristics of their crystalline sensitive element when exposed to ionizing radiation, have been already introduced in chapter 2. Although their first application is in medical physics, they are used for beam centering, measurements of field profile and dosimetry for X, gamma and charged particles in radiation tests of devices. Since RCFs are object of this chapter and chapter 4, it is considered appropriate to discuss extensively the properties of RCFs in this chapter. Sections 3.1, 3.2, 3.3 and 3.4 are meant as review of the properties, operating principle, types and related application of current RCFs. Since we developed a new RCF real-time reading method, discussed in chapter 4, the standard RCF reading methods (scanners and densitometers) are presented in section 3.5. Moreover, the understanding of RCFs chemical mechanisms of color changes and of how to quantify such changes, allowed us to carry out the absolute dosimetry with RCFs. This work, recently published (Campajola, Casolaro, and Di Capua, 2017) and presented in section 3.6 was carried out with the aim of comparing the response of a kind of film (EBT3 Gafchromic model) to several radiation types and energies (250 kV_p X-, ⁶⁰Co gamma-, ⁹⁰Sr/⁹⁰Y beta-rays, 1MeV electrons and protons of 23, 50 and 200 MeV) of interest in radiation hardness application. The calibration curve of these radiation types was found to be the same within the experimental uncertainties, demonstrating in this way the independence of the radiation type. In addition, this calibration equation belongs to the family of logistic equations. These non-linear equations describe phenomena of growth versus competition such as the kinetics of a chemical reaction that is the phenomenon of the darkening of the RCF. As a result, differently from polynomial fits usually found in RCF literature, the best fit parameters of section 3.6 have an important physical meaning. These aspects are discussed in section 3.7. Finally, the knowledge gained with RCFs allowed their employment for the full dosimetry characterization of the ⁹⁰Sr/⁹⁰Y. The employment of a compact beta source for TID tests has several advantages. For this reason we proposed this beta source for TID tests as alternative to the well-established ⁶⁰Co source. This work, presented at conferences of radiation hardness, is currently under review for publication. The dosimetry methods and results are discussed in section 3.8.

3.1 Historical background

The first work on the employment of solid solutions showing radio-synthesis after the exposure to radiations dates back to 1965 by Mc Laughing *et. al.* McLaughlin and

Chalkley, 1965. The subsequent works on RCFs can be attributed to the National Institute of Standard and Technology (NIST) Williams and Metcalfe, 2011; Humphreys, 1989; McLaughlin and al, 1996. The first prototypes of RCFs were sensitive in the range of dose from a few to hundreds of kGy and therefore these films were employed for high-dose applications only. A kind of radiochromic medium sensitive to lower doses (up to 5 Gy), known as Gafchromic film, was developed in 1986 by the International Speciality Products Inc. (ISP) Williams and Metcalfe, 2011. Nowadays RCF dosimetry is considered as a reliable technique for accurate dose assessment and quality checks in many applications of radiation physics. Several types of films are currently available on the market, covering a very wide range of dose from a few mGy to hundreds of kGy Soares, 2006.

3.2 Operating principle

RCFs consist of a single or double layer of radiation-sensitive material on a thin polyester base with a coating. RCF change their color when exposed to radiation. The radiation-sensitive materials in RCF are diacetylenes, a particular type of crystalline polyacetylenes (McLaughlin and al, 1996). The interaction of ionizing radiation with the film induces polymerization of the diacetylenes monomers (Wegner, 1972). In order to increase the low sensitivity to radiation of diacetylene crystals, these are dissolved in a solvent (e.g. n-butanol), which has also the advantage of improving the light resistance of the diacetylenes monomers Williams and Metcalfe, 2011. The dissolved crystals are dispersed in an aqueous gelatin solution that is coated onto a substrate (in most case it is a polyester substrate). It can be transparent or opaque Soares, 2006. Upon drying process, the crystals become fixed in orientation. Figure 3.1 shows the chemical reaction of the polymerization induced by heat, UV or ionizing radiation. (McLaughlin et al., 1996). This lead to

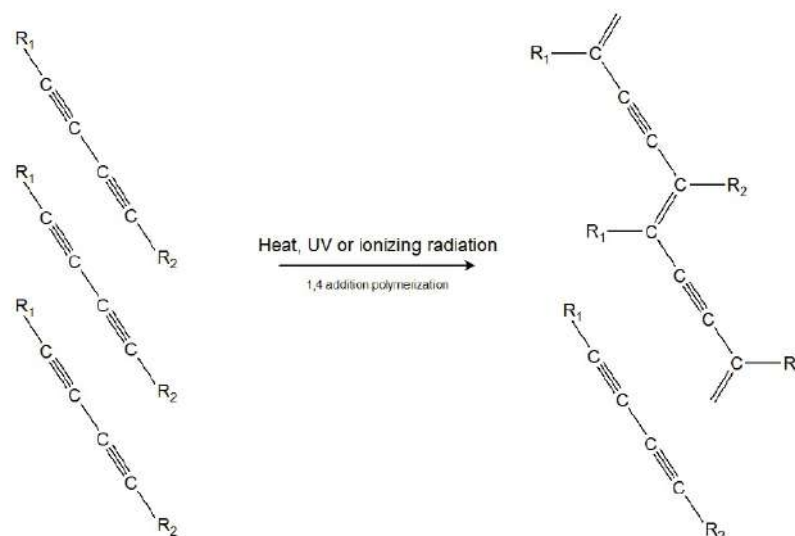


FIGURE 3.1: Polymerization induced by heat UV or ionizing radiation on the monomers of the active material of a radiochromic film (Williams and Metcalfe, 2011).

the production of polymer chains that grow in length with the exposure to radiation (Rink, Vitkin, and Jaffray, 2005). The polymer chains created have a color tending to the shade of blue. The microscopic phenomenon above-described results in a color change at macroscopic level. The level of darkness of a RCF can be related to the radiation dose. Differently from silver halide films, RCFs are self-developing, namely they don't need chemical or physical processing after irradiation Devic, 2011; Devic, Tomic, and Lewis, 2016. The time needed for the stabilization of the polymerization process depends on the type of RCF and for practical reasons, the films are read about 24 hours after the exposure.

3.3 Dependence on radiation type, energy and dose rate

RCFs are sensitive to almost any type of ionizing radiation (photons, electrons and charged particles over a wide range of energy and dose), being at the same time almost totally insensitive to room light. The response of most of RCFs shows very low dependence on the radiation quality, at least for low-LET (Linear Energy Transfer) radiation usually employed in radiotherapy and radiation hardness applications Glaser, Ravotti, and Moll, 2005; Wie et al., 2015. RCFs energy dependence to high-LET radiation is more complicated. Reinhardt *et. al* reported that RCF dosimetry in low-energy ion beams requires a correction of the LET dependent film response (Reinhardt et al., 2015). However, the response of the films to different LET-components of charged particle beams can be taken into account by applying relative effectiveness factors. For example, some types of RCFs, such as EBT2 and EBT3 Gafchromic films, intensively used in radiotherapy with photon, electron and also ion beams, are known for underestimate the dose in the Bragg Peak region. This is known in literature as "quenching effect". However, RCFs are successfully and commonly employed for the determination of percentage depth dose profiles of photon and ion beam in radiotherapy Avila-Rodriguez, Wilson, and McQuarrie, 2009; Kirby et al., 2009; Buenfil et al., 2002; Sorriaux et al., 2013; Castriconi et al., 2016. Concerning RCFs dose-rate dependence, no difference in response has been observed. The sensitivity to neutrons is very low: to date results about RCFs neutron sensitivity are reported by Bazioglou *et. al.* Bazioglou and Kalef-Ezra, 2001. In the practice, RCFs are not used for measuring neutron dose and neutron beam profiles as it is usually done for the other radiations.

3.4 Types of films and related applications

Nowadays RCF dosimetry is considered as a reliable technique for accurate dose assessment and quality checks in many applications of radiation physics. Such a wide use is consequence of the intrinsic characteristics of the films. Today RCFs are reliable, easy to use, cheap, portable and non-invasive instruments, providing accurate and permanent values of dose. Furthermore, they have very high spatial resolution and most of RCFs types are made of tissue-equivalent materials. These characteristics fit perfectly for the medical physics, in particular for the determination of percentage depth-dose curves in radiotherapy with photon and ion beams (Fletcher and Mills, 2008; Butson et al., 2003; Devic, 2011; Vatnitsky, 1997; Bilge et

al., 2009). Figure 3.2 shows the application fields in which RCFs are used as a function of the dose in Gy. All dose values reported from here on out are referred to

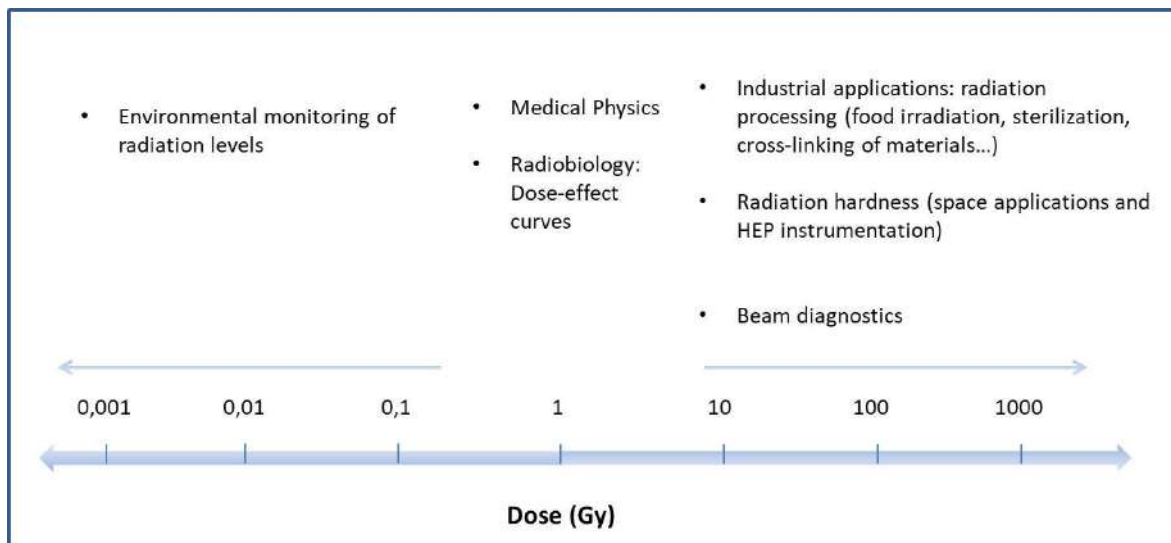


FIGURE 3.2: Applications of the radiation physics in which RCFs are employed.

water, that is the standard for the medical physics. RCFs are sensitive to all kinds of ionizing radiation employed in the applications (photons, electrons, proton and heavy ions). RCFs are used in the dose range from a few tens to hundreds of mGy for quality checks of typical diagnostic instrumentation such as X-ray tube for radiography and Computed Tomography (CT). For these purposes, the ISP provides the Gafchromic series XR. In particular, XR-QA2 films are suited for radiology quality assurance tests, XR-CT2 measure beam slice width in CT scanner, XR-M2 films are dedicated to mammography tests and XR-RV3 are used for peak skin dose measurement Tomic et al., 2014. These films are made of an active layer of about 25 μm between a layer of yellow polyester of 97 μm and a layer of white polyester (opaque layer). RCFs are used in the range from hundreds of mGy to tens of Gy for measuring doses typical of external beam therapy with photon and ion beams. The film dosimetry has been adopted as successful method by several hospitals, clinics and centres for cancer therapy Fiandra et al., 2006. The brachytherapy application deals with doses up to hundreds of Gy and RCFs are employed for dose verification also in this field Palmer, Nisbet, and Bradley, 2013b; Palmer et al., 2013; Palmer, Nisbet, and Bradley, 2013a. EBT3 Gafchromic films are intensively used in the medical physics for the determination of depth-dose curves of photon, electron and ion beams. These films are made of an active layer of about 28 μm sandwiched between two polyester layers of 120 μm ; they are available as sheets of 8x10 inches in order to allow the use when large radiation fields are needed. However, if the determination of dose in small areas is needed, it is possible to cut the films in smaller pieces without losing their characteristics. For very high-dose applications, such as industrial application, radiation processing, beam diagnostics and high energy physics (HEP) application, other kinds of films are available. Gafchromic HDV2 films are sensitive in the dose range from 10 to 1000 Gy. Beyond the kGys, thin foils films (active layer 12 μm and polyester substrate 97 μm) are used. GEX Corporation trades the B3

films (active layer: 18 μm), sensitive in the range 1-150 kGy; the Far West Technology makes available FWT60 films (active layer: 18 μm) for application in the range 0.5-200 kGy Barrett et al., 1990. It is notable that the employment of RCFs as dosimeter in HEP field is a topic under study. Owing to their characteristics, RCFs can be a perfect tool for dosimetry monitoring of such a harsh environment like that of HEP facilities: no electronics typical of other detectors and therefore no interaction with the electric and magnetic fields. However, a mixed radiation field of such facilities is very complicated to study with RCFs, being composed of different radiation types and energies. Figure ?? shows a

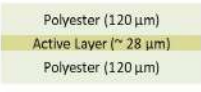
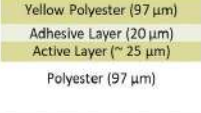
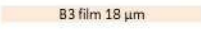
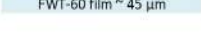
Model	Dynamic range (Gy)	Dynamic range (rad)	Structure
Gafchromic EBT3	1 cGy - 40 Gy	1 rad – 4 krad	
Gafchromic XR-QA2	0.1 cGy - 20 cGy	0.1 rad – 20 rad	
Gafchromic HDV-2	10 Gy-1 kGy	1 krad – 100 krad	
GEX Corp. B3	1 kGy - 150 kGy	0.1 Mrad – 15 Mrad	
FWT-60	0.5 kGy - 200 kGy	50 krad – 20 Mrad	

FIGURE 3.3: Main types of radiochromic films. The dynamic range and the film structure are shown.

3.5 Film reading and calibration

To measure the dose of a RCF, a physical quantity representing the darkening of the film has to be related to the radiation dose. The instruments typically employed for RCFs reading are commercial densitometers and scanners. The choice of one rather than another is due to the level of precision demanded. The densitometers are in fact easier to use but less sensitive. The output variable from densitometers is the optical density OD or absorbance defined as

$$OD = \log \left(\frac{I_0}{I} \right) \quad (3.1)$$

Here I_0 is the light intensity (at fixed wavelength or wavelength band) without the film and I is the intensity (at same wavelengths) of the light after crossing the film. The densitometers are therefore pre-calibrated with respect to a reference radiation light (e.g. 633 nm that is the light of a He-Ne laser). The scanners are more sensitive of densitometers, but more time-consuming. Several commercial software

allow data analysis of digitized images from scanners. In the case of RCF data analysis, *ImageJ* is the most common. The evaluation of the Pixel Values (PVs) of a defined Region of Interest (ROI) of the digitized film allows precise determination of the darkening of the film and ultimately of its dose. The PV represents the level of light intensity of a digitized image. More specifically, for gray-scale images, the PV is a single number stored e.g. as an 8-bit integer giving a range of possible values from 0 to 255. Usually "0" is the black and "255" the white. For RGB color images, separate red, green and blue components are specified for each pixel. These components are stored as separate grayscale-like images, namely one for each channel (red, green and blue). So a 24-bit color acquisition indicates 8 bit per channel. Figure 3.4 shows the typical output from *ImageJ*, consisting in the histogram of the PVs.

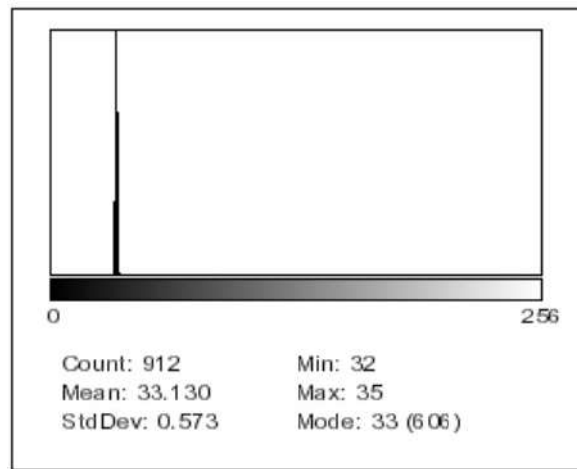


FIGURE 3.4: Output histogram from software ImageJ.

In particular, the histogram of figure 3.4 refers to an acquisition of an EBT3 Gafchromic film with an EPSON V800 scanner. This acquisition as well as all the acquisitions of the films for the absolute calibration discussed in section 3.6, were performed with the scanner in mode 24 bit color and 400 dpi. The analysis of a film by means of a specific channel (red, blue or green) increases the sensitivity in a certain dose range (Micke, Lewis, and Yu, 2011), but get it worst in another. Since we are interested in studying the overall dynamic range, the analysis in greyscale of the digitized image was found the best trade-off. In the typical case of figure 3.4, the mean PV is 33.1 with standard deviation of 0.6 (1.8%). PV can be transformed into OD or OD-related functions such as net-OD (Butson et al., 2003; Williams and Metcalfe, 2011). The last is considered in order to take into account the darkening of unexposed films, called fog. The net-OD is defined as

$$OD = \log \left(\frac{I_{unexp} - I_{bckg}}{I_{exp} - I_{bckg}} \right) \quad (3.2)$$

where I_{unexp} and I_{exp} are the measured intensities of the unexposed and exposed film and I_{bckg} is the light intensity when no light is transmitted. RCFs calibration curves are therefore relations of dose versus OD, net-OD or PV. ion

3.6 Response of EBT3 Gafchromic films to more radiation types

EBT3 Gafchromic films are dosimeters of primary interest in medical applications of therapy with photon and ion beams for precise assessment of dose to the phantom or for measurements of dose profiles and PDD curves. The dynamic range declared by the manufacturer is 1 cGy - 40 Gy. This dose range is of interest also for many RHA tests among which some TID tests in which the total dose is delivered in many steps allowing more than one testing of the device's performances. The full characterization of these films and in particular of their response to several radiation types is fundamental for their employment in this specific application. The study presented here meets these requirement by studying the response of EBT Gafchromic films to 250 kV_p X-, ⁶⁰Co gamma- and ⁹⁰Sr/⁹⁰Y beta-rays as well as to protons of different energies and 1 MeV electrons (Campajola, Casolaro, and Di Capua, 2017), the corresponding dose rates have different values, making possible a quantitative study of dose-rate dependence.

Dosimetry and radiation sources

The response of the films to a single radiation type was characterized respect to surface dose. For charged radiation fields surface dose D was evaluated with the following formula:

$$D [Gy] = 1.6 \cdot 10^{-10} \times \frac{1}{\rho} \frac{dE}{dx} \left[\frac{MeVcm^2}{g} \right] \times \Phi [cm^{-2}] \quad (3.3)$$

where $\frac{1}{\rho} \frac{dE}{dx}$ is the total mass stopping power in $MeVcm^2/g$ of charged particle in water and Φ is the fluence in cm^{-2} . The surface doses of neutral radiation fields (X- and gamma-rays) were evaluated by certified dose. Moreover, during the irradiations, the doses were controlled by means of independent measurements with ionization chambers and Fricke dosimeters (section 2.3). The main characteristics of the radiation sources used for this study, the beam diagnostic methods and independent dose measurements are discussed below.

- X-rays from SIEMENS X-ray tube of Physics Department from University of Napoli Federico II. The X-ray tube was set to 250 kV_p, 15 mA and 1 mm-Cu filter. The X-ray tube is equipped with a system of adjustable collimators and a 10×10 cm² field size on the film position was used. The films were placed at fixed position from the anode position. The dose rate in the film position was measured by means of General Purpose Radcal Ionization Chamber (6 cm³) and found to be 1.21±0.01 Gy/min.
- Gamma-rays from ⁶⁰Co-source of ISOF-CNR at Bologna (section 2.2). The Gammacell was manufactured by Atomic Energy of Canada Ltd for use in an unshielded room. In order to characterize the dose uniformity of the Gammacell active volume, measurements with EBT3 foils of 8×17 cm² were carried out. Results showed uniformity of dose within 0.6% in vertical dimension and

0.4% in horizontal dimension of the Gammacell active volume. The dose rate at irradiation time was measured by means of Fricke dosimeters and found to be 3.33 ± 0.02 Gy/min (figure 2.4). This value is in agreement with the dose rate, scaled by the radioactive decay, obtained with certified dosimetry performed with alanine dosimeters in 2007 by Risø National Laboratory.

- Beta-rays from 38 MBq $^{90}\text{Sr}/^{90}\text{Y}$ radioactive source. The dose rate values were measured as a function of distance by means of a Fluke Biomedical 451B Ion Chamber Survey Meter (349 cm^3) and a cylindrical General Purpose Radcal Ionization Chamber (6 cm^3) (figure 2.3). The source-detector distance was controlled and measured by means of sub-millimeter accurate stepper motor. The extrapolated dose rate at 1 cm from the source was 3.40 ± 0.02 Gy/hour. EBT3 films were positioned at 1 cm from the source.
- 1 MeV electron beam from ILU-6 LINAC accelerator of Institute of Nuclear Chemistry and Technology in Warsaw (figure 2.9). The beam was extracted in air. The films were placed on the surface of an aluminum plate positioned at 72 cm from the output window of the accelerator. The dose in the film position is proportional to the charge delivered on the Al-plate. The scheme of the elements used for the dose calculation is reported in figure 3.5. An ADC was

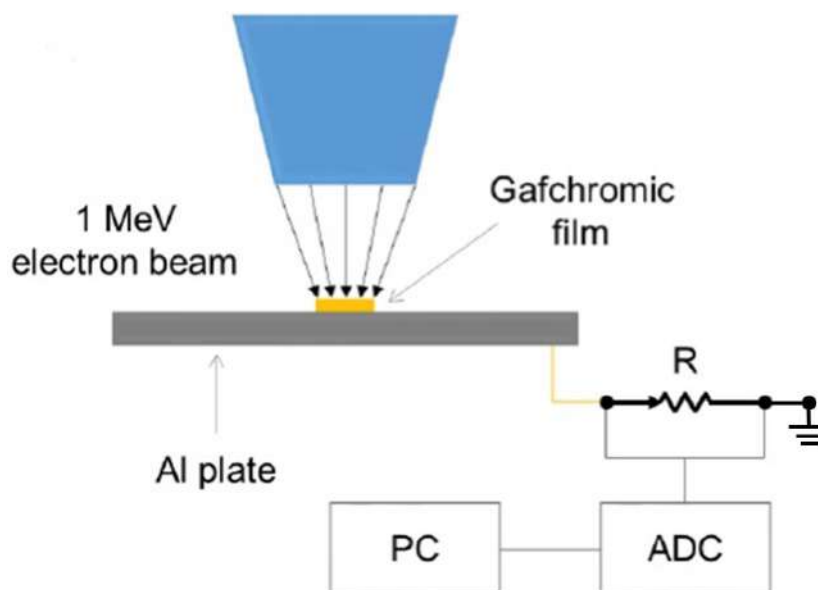


FIGURE 3.5: Experimental setup employed for dosimetry measurements at ILU-6 accelerator in Warsaw.

used to measure the voltage difference across the resistor. The integral over the time gives the value of dose in the film position. The evaluated dose rate in the film position was 23.03 ± 0.07 Gy/min.

- 23 MeV proton beam from tandem accelerator of LNS-INFN at Catania (figure 2.6), proton beams of 50 MeV and 200 MeV from the cyclotron of PSI (figure 2.11). In both experiments, the irradiations were performed by extracting the beam in air. During the irradiations, the proton fluence rate in the film

position was monitored by measuring the current with ionization chambers (section 2.5). For the irradiations performed at LNS-INFN, the monitor chamber employed at CATANA facility for protontherapy was used (Cirrone et al., 2006). Before the films irradiations, preliminary measurements for the calibration of the ionization chamber were performed. In particular, the ionization chamber was calibrated by measuring the current from a Faraday Cup. As far as the irradiations performed at PSI, the calibration of ionization chamber was performed by recording the counts from a Bicron scintillator, placed in the film position. The proton energy on the film was calculated by subtracting the energy loss of the incident beam in all the elements between the output window of the beam line and the RCF.

Calibration of EBT3 Gafchromic films

The calibration of the films was performed as grey PV versus surface dose D . The greyscale analysis was preferred to the RGB scale analysis because it is a good trade-off between film sensitivity and dynamic range (section 3.5). The calibrations were accomplished separately for sets of films exposed to single radiation source (X-, gamma-, beta-rays and 23 MeV protons). The experimental trend of the data (PV- D) of each set of films fit to the Green-Saunders equation (Lee, 2005):

$$PV = PV_{min} + \frac{PV_{max} - PV_{min}}{1 + 10^{\beta(\log D_0 - \log D)}} \quad (3.4)$$

Here PV and D are the dependent and independent variables respectively and are PV_{min} , PV_{max} , β and D_0 fitting parameters. PV_{min} and PV_{max} are the minimum and maximum values of the PV. These fix the PV films dynamics. β is a parameter that determinate the range of grey shades and D_0 is the abscissa of the inflection point of the corresponding sensitometric curve. Section 3.7 discusses in detail the Green-Saunders equation and the mentioned fitting parameters by showing its validity for all RCFs, being the equation that describe the phenomenon of the darkening of the films to incident radiation. The best estimates of the free parameters (PV_{min} , PV_{max} , β and D_0) and values of the reduced chi-square $\tilde{\chi}^2$ of the single calibrations for X, gamma, beta and proton radiation calibrations are summarized in Table 3.1.

TABLE 3.1: Best estimates of the free parameters of the Green-Saunders equation for X-, gamma-, beta-rays and proton radiation. The last column shows the value of the reduced chi-square.

	PV_{min}	PV_{max}	β	D_0	$\tilde{\chi}^2$
X-ray	2.26 ± 1.02	125.10 ± 1.10	-0.85 ± 0.02	7.14 ± 0.20	0.7
Gamma-ray	2.25 ± 1.49	124.40 ± 1.55	-0.86 ± 0.03	7.36 ± 0.27	0.8
Beta-ray	3.87 ± 1.36	125.90 ± 1.22	-0.87 ± 0.03	6.59 ± 0.24	1.2
Proton	0.88 ± 2.11	123.90 ± 1.57	-0.81 ± 0.05	7.36 ± 0.34	2.0

The plot of figure 3.6 shows the absolute calibration of EBT3 Gafchromic films. In this plot there are the data of all films used in this work and the Green-Saunders equation (dotted grey curve) evaluated for X-rays only. The number of exposed

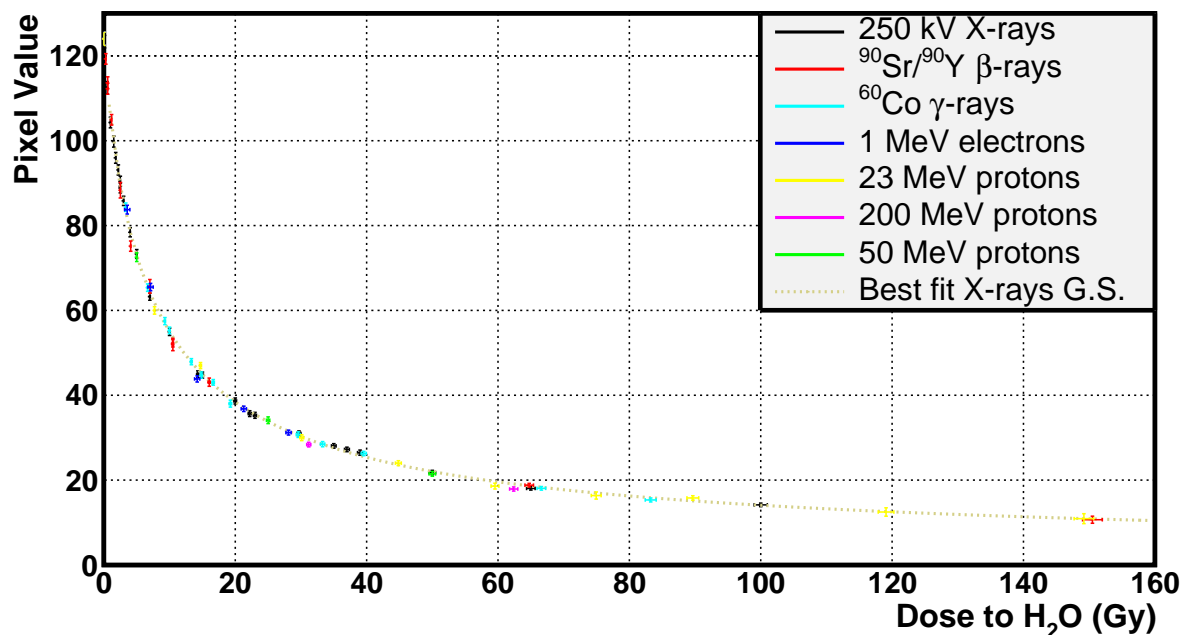


FIGURE 3.6: Absolute calibration of EBT3 films. The grey curve is the Green-Saunders equation evaluated for X-rays.

films, the dose range and the PV average uncertainty for each radiation are summarized in Table 3.2. The overall average uncertainty of the PVs is 2% and the

TABLE 3.2: Main irradiation features of EBT3 films used in this work. For each irradiation, the number of exposed films, the dose range and the average PV uncertainty are reported.

Radiation type	No. of exposed films	Dose range (Gy)	PV uncertainty (%)
X-ray	25	0.1-100	1.6
Gamma-ray	13	3-83	1.8
Beta-ray	12	0.3-150	2.3
Electron	6	3-28	1.5
Proton	14	5-150	2.7

evaluated dose uncertainties are within 1% for all exposed films. Figure 3.7 shows the percent deviation of all experimental data from the Green-Saunders equation evaluated for X-rays. The average deviation of all data respect to the X-rays Green-Saunders equation is 0.3%.

Discussion of the results

The calibration of a lot of EBT3 films can be performed with any a-priori-known radiation field. The only constraint to consider is that the dose rate has to be high enough to cover the range of dose needed for the calibration in a reasonable amount of time. The study of the characteristics of EBT3 Gafchromic films and in particular of their response to many radiation sources commonly employed in RHA tests was carried out. Some of their well-known properties have been confirmed among which the high spatial resolution, easy handling and data analysis. As they can be

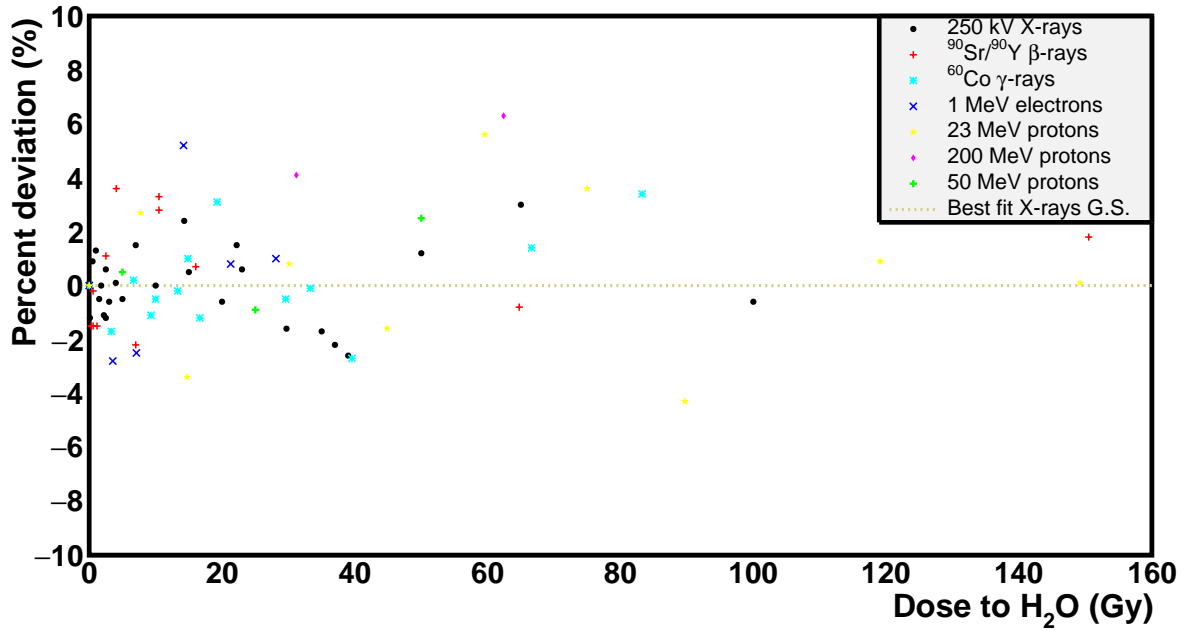


FIGURE 3.7: Percent deviation of experimental data from the best fit equation evaluated for X-rays.

cut in small pieces ($30 \times 30 \text{ mm}^2$) and the thickness is approximately $300 \mu\text{m}$, in most cases these films can be easily put in front (or in the very proximity) of the device for accurate monitoring of irradiation doses. The calibration of 70 films exposed to different radiation sources (LET of few MeVcm^2/g) show that the darkening of the films is independent of the incident radiation type. The best fit of the experimental data (PV, D) is given by the Green-Saunders equation (eq. 3.4). It fits to the experimental data in average within 0.3%. The fitting parameters of calibration curves of films exposed to single radiation fields have the same values within the error bars. As a result, one can perform the calibration of a set of films with e.g. common available X-rays or ^{60}Co -gamma sources. The dose of an unknown film can be evaluated by inverting the Green-Saunders equation:

$$D = D_0 \left(\frac{PV - PV_{min}}{PV_{max} - PV} \right)^{\frac{1}{\beta}} \quad (3.5)$$

Once the calibration of a set of films has been carried out and the fitting parameters of eq. 3.4 have been evaluated, eq. 3.5 gives the absorbed dose of an unknown film. The dynamic range of EBT3 Gafchromic films was found to be higher with respect to what declared by the manufacturer. It goes from few cGy up to more than one hundred Gy or that is the same for charged particle beams, fluences of 10^{11}cm^{-2} . In radiation hardness applications long term irradiation tests are usually performed by means of different radiation sources. The dose can be measured, verified and certified by means of radiochromic films.

3.7 Absolute dosimetry with radiochromic films

In section 3.6 we found that the equation that describe the phenomenon of the darkening of the films is the Green-Saunders equation (eq. 3.4) that rewrite here for simplicity in the general form:

$$y = y_{min} + \frac{y_{max} - y_{min}}{1 + 10^{\beta(\log x_0 - \log x)}} \quad (3.6)$$

This equation belongs to the class of logistic functions describing growth versus competition models. The basic model of growth versus competition is known as logistic equation:

$$dy/dt = cy - by^2 \quad (3.7)$$

Examples of growth versus competition models are the phenomena of population growth and kinetics of chemical reaction. In these phenomena, belonging to different domains, there is a term responsible for the growth and a term responsible for the competition. A solution of eq. 3.7 is the S-curve (eq. 3.6). Figure 3.8 shows the graphical trend of eq. 3.6 as $y(x)$ (a) and $y(\log(x))$ (b).

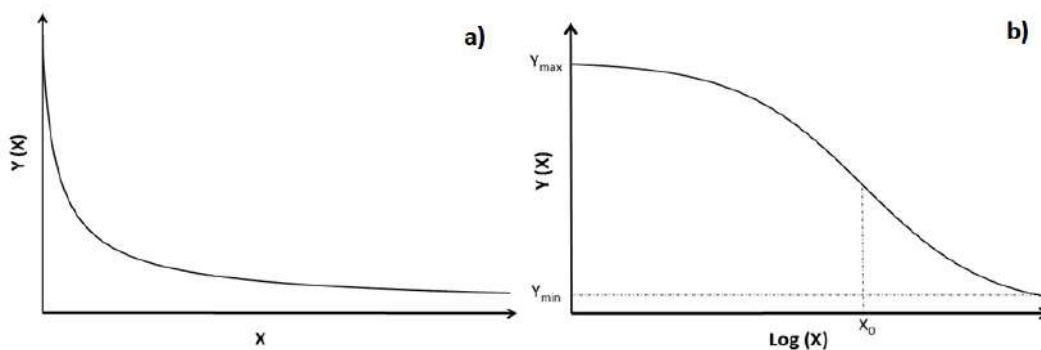


FIGURE 3.8: Graphical trend of eq. 3.6 as a function of x (up) and $\log(x)$ (down).

The plot in the figure 3.8 (a) is that of the absolute calibration of figure 3.6. The plot in the figure 3.8 (b) is the sensitometric curve, also referred to as characteristic curve or *Hurter–Driffel* curve. This curve is well known in scientific studies of light-sensitive materials and especially photographic film. The graphical interpretation of the free parameters y_{min} , y_{max} and x_0 is shown in figure 3.8 (b). It is clear that PV_{min} and PV_{max} fix the film dynamics and D_0 is the inflection point of the sensitometric curve. In order to explain the meaning of the fourth free parameter, i.e. β , let consider the Green-Saunders equation found in section 3.6 in which we fix the free parameters PV_{min} , PV_{max} , D_0 with β varying. Figure 3.9 shows different Green-Saunders equation with the change in β .

The sensitivity of a set of films decrease with increasing β , which represent the range of the possible grey shades or grey tones. Since the Green-Saunders equation describe the phenomenon of film darkening, it is valid for all types of RCFs. As an example, figure 3.10 shows the calibration of a set of B3 films exposed to 1 MeV electrons from ILU-6 LINAC accelerator at doses from some kGy to hundreds of kGy.

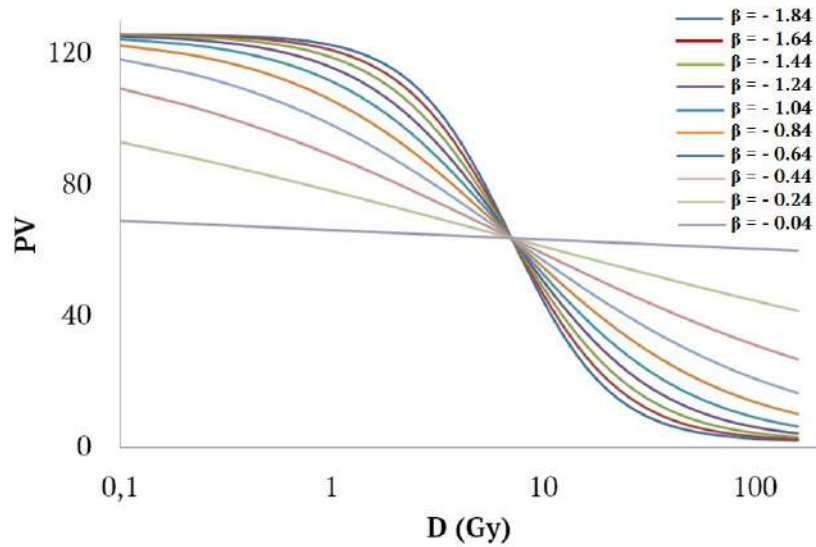


FIGURE 3.9: Green-Saunders equations with the change in β .

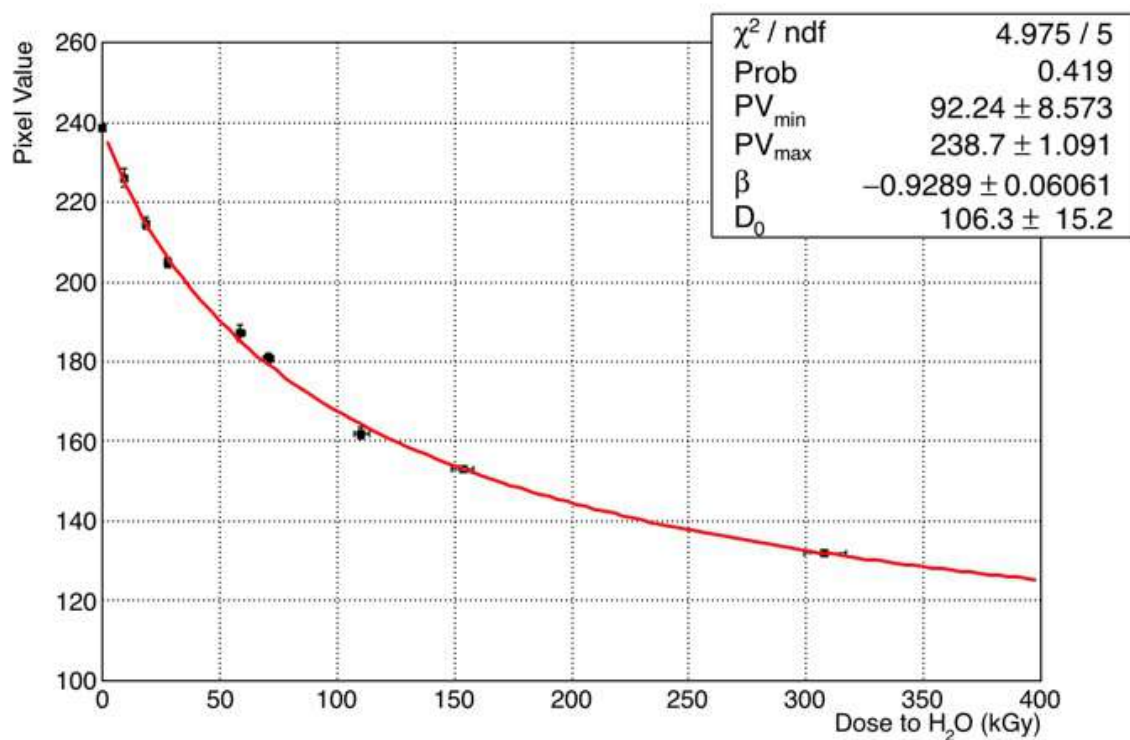


FIGURE 3.10: Calibration of a set of B3 films exposed to doses of hundreds of kGy with 1 MeV electrons at ILU-6 LINAC accelerator at Warsaw.

The data fit perfectly to the Green Saunders equation (red curve). The best estimates of the free parameters are shown in the inset of figure 3.10.

3.8 An innovative radiation source for TID tests

Calibrated EBT3 Gafchromic films were used for the dosimetry of a compact $^{90}\text{Sr}/^{90}\text{Y}$ beta source. The full characterization of such a radiation source aimed at validate it as alternative source to ^{60}Co gamma source for TID tests. The ^{60}Co is in fact the main source for these tests; the MIL-STD-883 standard proposes also the use of electrons from LINAC accelerator (table 2.1). Furthermore, X-ray sources and in some cases protons are used. However, the complex space radiation environment is composed by radiation of many types and energies; in particular long-term degradation of electronics is mainly determined by trapped particle belts (electrons and protons) and solar particle events (mostly protons and a relative contribution of electrons). The use of sources that better represent the space environment is preferable. Moreover, the use of a confined and directional radiation field, such as that of a beta source, has some practical advantages among which that of not using complex shielding of ancillary electronics. This usually helps in using typical System on Chip (SoC) modular evaluation boards during test setup providing cheaper and faster solutions. An additional advantage consists in the easy collimation of electrons from the beta decay. This allows accurate studies of specific and defined regions in large surface devices for investigating areas of the DUT more sensitive to TID damage.

The $^{90}\text{Sr}/^{90}\text{Y}$ beta source

The ^{90}Sr (half life: 28.74 years) isotope undergoes beta $^-$ decay with maximum energy of 546 keV. The decay energy is distributed to an electron, an anti-neutrino and the ^{90}Y isotope (half life: 28.74 years). This is in secular equilibrium with the ^{90}Sr undergoing a further beta $^-$ decay to the ground state of the ^{90}Zr with maximum energy of 2.28 MeV.

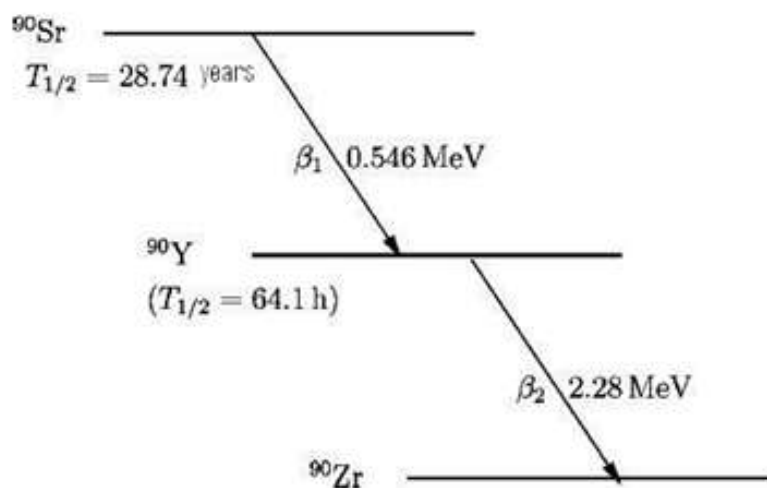


FIGURE 3.11: Decay scheme of the ^{90}Sr and ^{90}Y isotopes.

The energy spectrum of beta particles emitted from a 38 MBq $^{90}\text{Sr}/^{90}\text{Y}$ source was measured by means of a NaI scintillator. The energy spectrum is shown in figure 3.12.

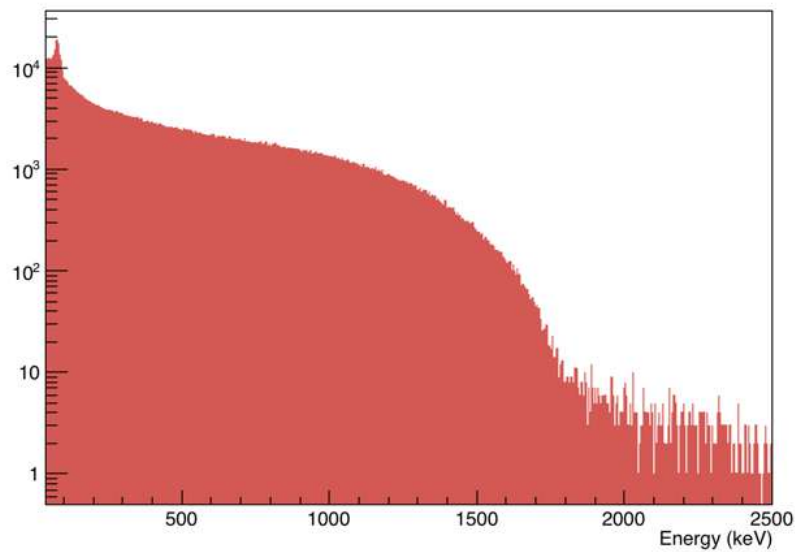


FIGURE 3.12: Energy spectrum of $^{90}\text{Sr}/^{90}\text{Y}$ beta source measured with a NaI scintillator.

It involves the contributions of beta decays of ^{90}Sr and ^{90}Y isotopes. The use of a lead shielding around the scintillator was necessary for avoiding pile-up effects caused by high intensity of the source. Since TID tests are usually performed with device with (plastic or ceramic) package, electron irradiation above few hundred keV can penetrate the package and ionize the DUT at die level. In order to consider these effects, the spectrum of the ^{90}Sr and ^{90}Y source was measured after 1 mm PMMA and aluminum absorbers, simulating package layers. Figure 3.13 shows the spectrum of the source (same as figure 3.12), the spectrum after 1 mm PMMA and after 1 mm aluminum. .

The effect of the package consists in an integral reduction of the intensity. For a low-Z material such as PMMA, the shape of the spectrum remains approximately the same, while an intermediate-Z material such as aluminum results in a modify of the shape in particular from 500 keV on.

Dosimetry of the beta source

In order to accurately measure the dose-rate of the 38 MBq ^{90}Sr and ^{90}Y source, EBT3 Gafchromic films and a Radcal ionization chamber (6 cm^3) have been employed. The size of ionization chamber does not permit dose rate measurements at short distances. In fact, only EBT3 films were used for this purpose, while dose rates at higher distances have been measured with the ionization chamber. The plot in figure 3.14 shows the dose rate as a function of the distance measured with a Radcal ionization chamber (6cm^3) and EBT3 Gafchromic films.

Measurements with the ionization chamber have been performed from 150 to 1.8 cm; EBT3 films have been used for short distances from 4.0 to 0.1 cm. It is noticeable the excellent agreement between dose measurements by two different dosimeters. The measured dose rate at 1.0 cm distance from the source has been found to be 346 rad/h, while the maximum dose rate at the shortest distance 8.160 krad/h. A

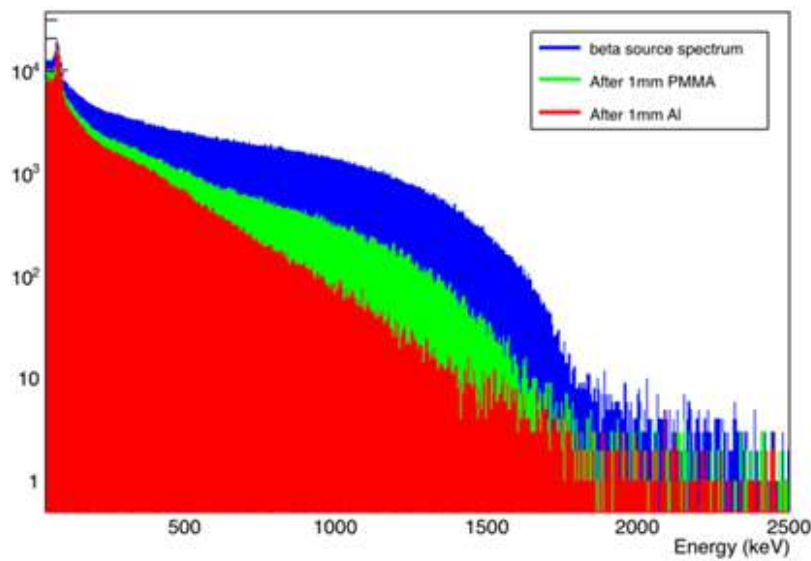


FIGURE 3.13: Comparison of spectra of the ^{90}Sr and ^{90}Y beta source (figure 3.12) with 1 mm PMMA and aluminum absorbers. These simulate the effects of the package.

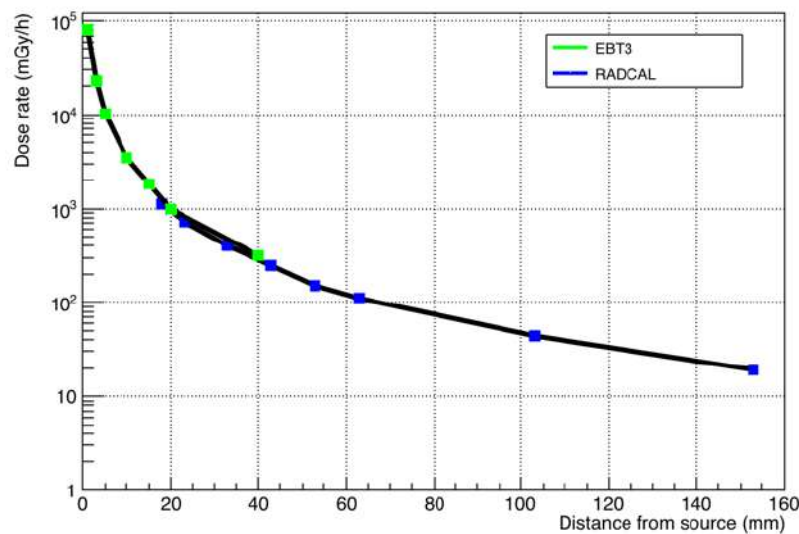


FIGURE 3.14: Dose rate of the of the $^{90}\text{Sr}/^{90}\text{Y}$ beta source as a function of the distance measured with Radcal ionization chamber (6cm^3) and EBT3 Gafchromic films.

measurement of the dose has also been performed with PMMA and Al absorbers as shown in figure 3.15.

The effect of the absorbers results in a reduction of the dose to 59% and 32% with respect to the case without shielding for 1 mm PMMA and 1 mm Al, respectively. The evaluation of dose at silicon die level is possible through simulation or by direct measurements for any complex package, once the composition is known. In addition, the availability of a part of package standalone makes possible dose measurements before the TID test is performed. The uniformity of the radiation field on

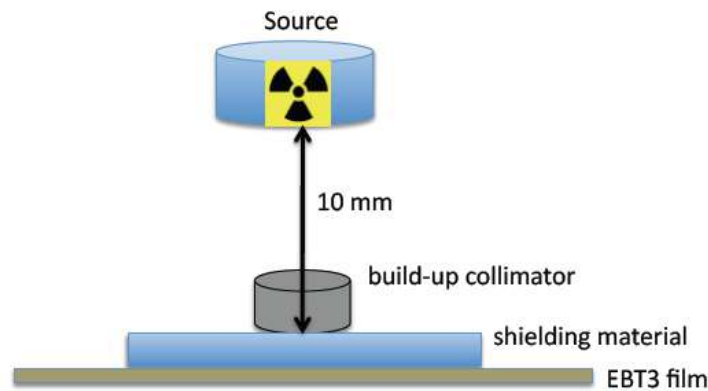


FIGURE 3.15: Layout of dose measurement with absorbers.

the DUT is one of the major requirements for a TID test, as pointed out in section 2.1. The dose profile can be precisely measured with EBT3 Gafchromic films. When the DUT is directly exposed to the source, the non-uniformity of dose profile is within 10% over a 10 mm field. In order to improve the level of uniformity, a collimator between the source and DUT is used. Figure 3.16 shows the spatial dose profile for the source with and without circular collimators of different sizes.

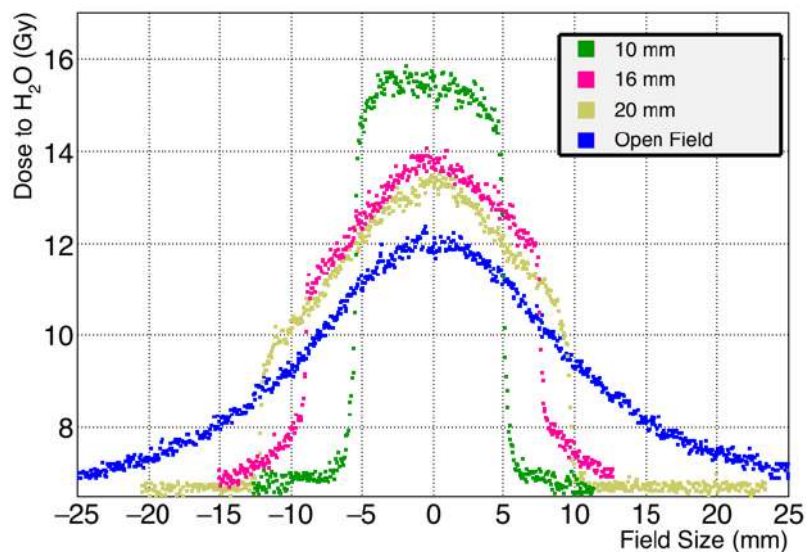


FIGURE 3.16: Radiation field profile with and without collimators. A non-uniformity less than 4% is obtained over 10 mm diameter (green points).

The results show that, by using a 10 mm collimator, a significant improvement is achieved. In these conditions, the maximum non-uniformity on the DUT surface is within 4%. The collimators also produce a build-up effect on the DUT. A dose enhancement of 30 % has been measured by using the 10 mm collimator. In the case of a larger device, the radiation field can be easily increased by varying the distance from the DUT. Figure 3.17 shows a picture of irradiation of an electronic device for TID tests.



FIGURE 3.17: The $^{90}\text{Sr}/^{90}\text{Y}$ beta source during a TID test.

Unlike as for ^{60}Co sources, the $^{90}\text{Sr}/^{90}\text{Y}$ beta source allows irradiations on chip, resulting in a sparing of other electronic components that are part of the DUT.

TID test with the $^{90}\text{Sr}/^{90}\text{Y}$ beta source

The full characterization of the $^{90}\text{Sr}/^{90}\text{Y}$ beta source was carried out aiming at using it as radiation source for TID tests alternative to the common sources (^{60}Co gamma source). A comparison of the performances of a electronic device under standard ^{60}Co gamma and under innovative $^{90}\text{Sr}/^{90}\text{Y}$ beta TID was carried out. An example of a potential target for the proposed TID method is the characterization of the complex COTS-based digital system such as the 90 nm device SPC56EL70L5 microcontroller from *ST-Microelectronics*. This device was already previously tested under radiation with protons and standard ^{60}Co source at ESA-ESTEC (Di Mascio et al., 2018). The beta source was position at distance 8 mm from the DUT. The corresponding dose rate was 538 rad(Si)/h. Figure 3.18 shows the SPC56EL70L5 microcontroller exposed to the $^{90}\text{Sr}/^{90}\text{Y}$ beta source during the TID test.



FIGURE 3.18: SPC56EL70L5 microcontroller during testing with the $^{90}\text{Sr}/^{90}\text{Y}$ beta source.

The results of irradiation with the $^{90}\text{Sr}/^{90}\text{Y}$ source showed a correlation with that of the ^{60}Co . The device failed the reprogramming at 25.8 krad in the first case and approximately 30 krad in the second one. A full description of the results and in particular of the electronic performances of the device are summarized in a work recently submitted as proceeding of NSREC conference (Menicucci et al., 2018).

Chapter 4

Real-time dosimetry with radiochromic films

In this chapter a new RCF reading method based on opto-electronic instrumentation is presented. It allows real-time measurements with RCFs overcoming therefore the intrinsic limitation of the off-line reading methods with commercial systems (densitometers and scanners). This new method, for which a patent was filed in January 2018, can be potentially used in any field of radiation physics where RCFs are employed. Section 4.1 introduces the scientific motivations, by comparing this work with others on the same subject. Section 4.2 shows the operating principle of the innovative reading method. Section 4.3 presents the results, in terms of calibration curves, of exposures of two types of films of different structure to ^{60}Co sources of two dose-rates. Finally, section 4.4 discusses the results and the future works that we intend to carry out on the basis of this work.

4.1 Motivations

In Chapter 3 the main characteristics of Radiochromic Films (RCFs) were widely discussed. RCFs have interesting features for applications in many fields of radiation physics. A kind of RCF, the EBT3 Gafchromic model, intensively used in applications of medical physics, was fully characterized. The calibration of a set of 70 EBT3 films exposed to many radiation types demonstrated the independence of the film response of type, energy and dose rate. The absolute dosimetry with radiochromic films was demonstrated by means of the theoretical approach based on logistic functions (Green-Saunders equation) which describe the physical phenomenon of the darkening of the films to radiation. Successively, the characterization of a $^{90}\text{Sr}/^{90}\text{Y}$ beta source as alternative to the standard ^{60}Co source was accomplished. For this purposes, RCFs were useful in particular for dose measurements at millimeter distances. The wide dose range, the independence RCF response to radiation type, the high accuracy and precision as well as the low cost and dimensions together with the absence of ancillary electronic make these films a very interesting dosimeter for measurements of dose delivered on devices in Radiation Hardness Assurance (RHA) tests. However, since current RCF reading techniques are based on the use of densitometers and scanners (that provide dose values only after the exposure of the films to radiation), to date it is not possible to perform real-time dose measurements with RCFs. In order to overcome this intrinsic limitation, an innovative methodology for RCF real-time reading is proposed. This new methodology is based on a

opto-electronic instrumentation by using an optical fiber probe for the determination of optical changes of the films induced by radiation. It allows measurements of dose with high degree of precision and accuracy. Previous works on this topic are reported by Mignani *et. al.* and Rink *et. al.* Mignani *et al.*, 1998; Rink, Vitkin, and Jaffray, 2005 together with a U.S. patent Rink *et al.*, 2015. The method proposed here has several new interesting features also compared to the existing RCF reading techniques. Because it makes direct use of commercial RCFs (cut in small pieces), it avoids carrying out complicated operations of deposition of radiochromic media on the tip of the fiber. Moreover, with respect to the above-quoted RCF real-time techniques, based on single-use probes, this method uses an optical fiber probe, in which the RCF is disposable and can be quickly replaced with other RCFs in order to make other measurements. This allows the preservation of the above-discussed characteristics of the films. The advantages of using an optical-fiber-based instrumentation instead of commercial RCF reading tools, not only allow the performance of the reading of the dose in real-time, but also the exploitation of most of the potential of the RCF dosimeters. In fact, as will be demonstrated in the following, the range of sensitivity of some types of films can be extended by several orders of magnitude, with respect to that declared by the manufacturer. The originality, the technological advances with respect to the existing RCF reading methods and the potential diffusion on the market made the invention patentable. For these reasons a National Patent was filed in 2018.

4.2 Optical-fiber-based setup

Figure 4.1 shows the schematics of the experimental apparatus employed for the real-time reading of RCFs.

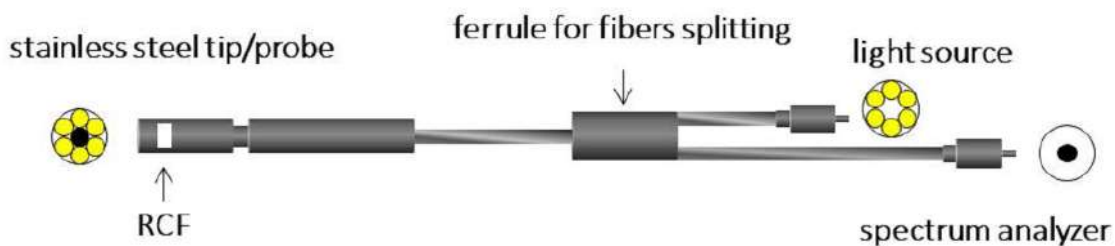


FIGURE 4.1: Schematic of the experimental apparatus for the real-time reading of RCFs.

It basically consists of an optical fiber bundle with six illuminating fibers positioned on the sides of the bundle and one light-collecting fiber in the centre, a RCF, a light source and a spectrum analyzer connected to a computer for data analysis. The six illuminating (core diameter: $100\ \mu\text{m}$) fibers transport the light from the source to the tip of the probe where the RCF is positioned. After passing into the RCF, the light is first backscattered by an appropriate material, then collected by the central fiber (core diameter: $200\ \mu\text{m}$) and therefore sent back to the spectrometer. Changes of optical properties of the film due to the darkening induced by ionizing radiation can be in this way detected in real-time. Figure 4.2 shows the picture of the experimental apparatus.

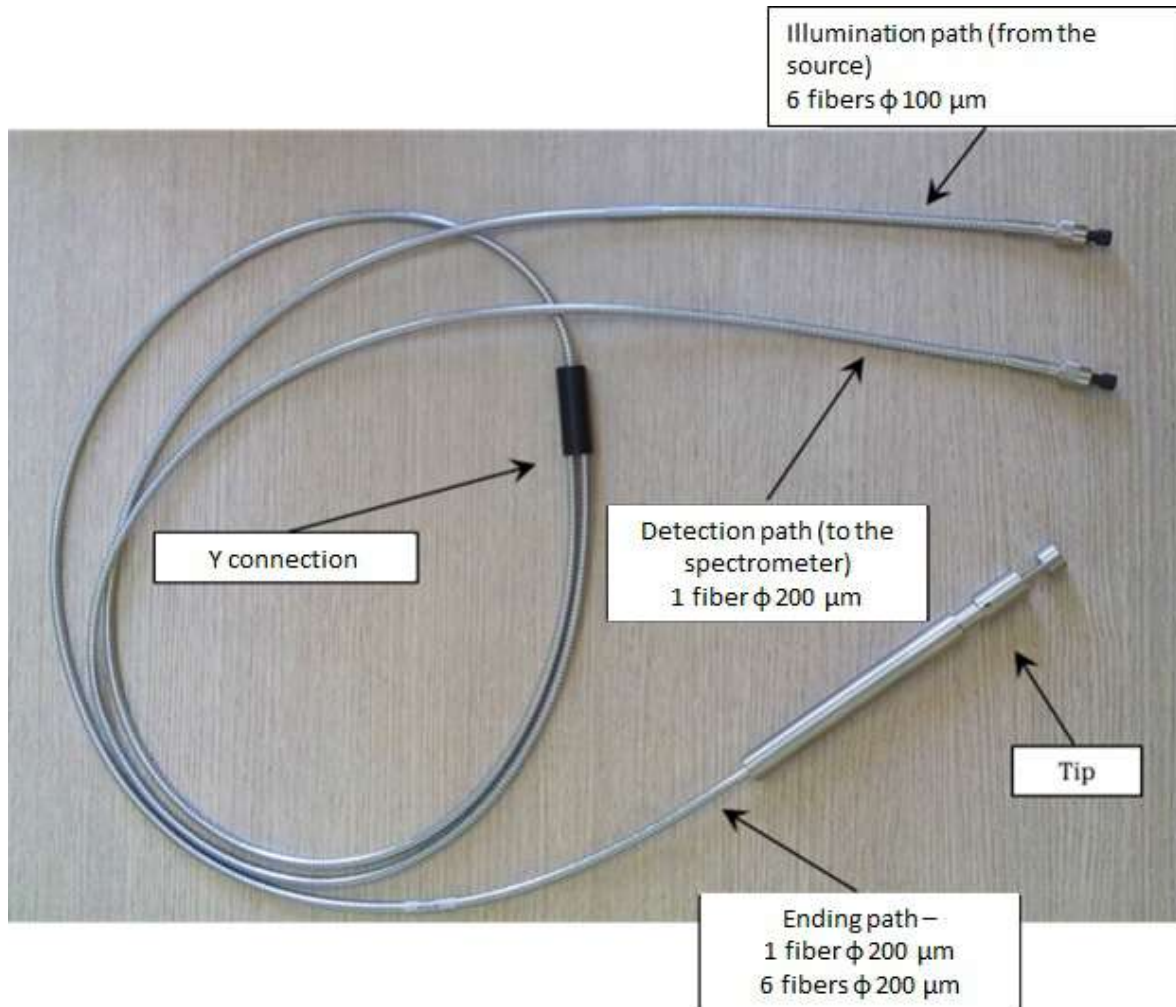


FIGURE 4.2: Picture of the experimental apparatus for the real-time reading of RCFs.

The choice of the backscattering material affects the integration-time of the spectrometer. This parameter is fundamental, being related to the sensitivity of the method: it determinates the minimum amount of time in which the spectrometer can detect sensitive changes of the light. Figure 4.3 shows the schematics of the elements of the terminating part of the innovative set-up. This part was designed and carried out with a twofold aim: to ensure the interaction of ionizing radiation with the RCF and to allow the backscattering of the light with enough intensity to be detected by the spectrometer. With reference to the nomenclature of Fig. 4.3, the element "2" is both a support for the optical fibers bundle and a holder for backscattering materials. These materials can be plastics such as ABS or Teflon, in the form of cylinders (height 1 mm and diameter 6 mm) or thin foils of Mylar (of thickness $1.5 \mu\text{m}$). It has to be noticed that the designed material-holder allows the use of the RCF itself as backscattering material, if needed. This is very useful if the RCF has an opaque layer; this is the case, e.g. of Gafchromic XR- models. The element "4" allows the hosting of the plastic cylinder. This can be screwed and fixed on the element "2". If the thin foils are used, the element "3" can be inserted in the material-holder "4". The bundle for the optical fibers can be made of different materials such as stainless

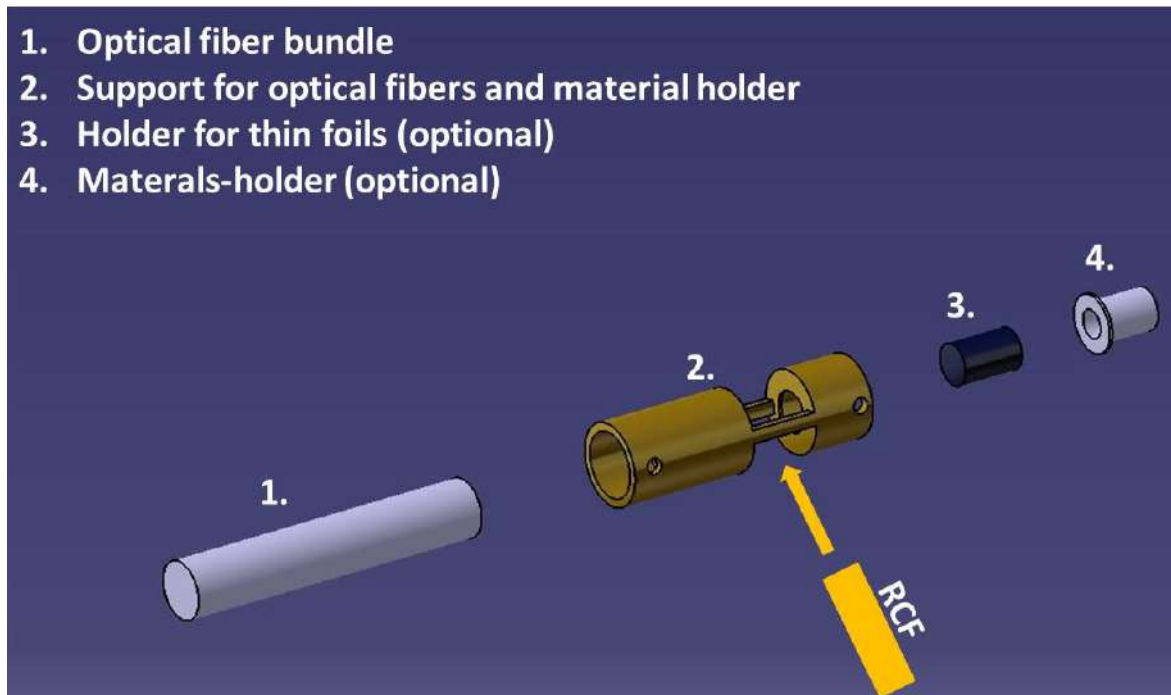


FIGURE 4.3: Design of mechanical elements for the support of the backscattering material.

steel, plastics (less interacting with ionizing radiation) or, if necessary, the single fibers can be used. During the operation, the whole apparatus is positioned in the irradiation area. The light source used for this prototype is the "AvaLight-DH-S-BAL Balanced Power" and the spectrometer "AvaSpec-ULS2048XL". The latter is controlled via computer. The RCF is positioned in the material holder as shown in Fig. 4.4.

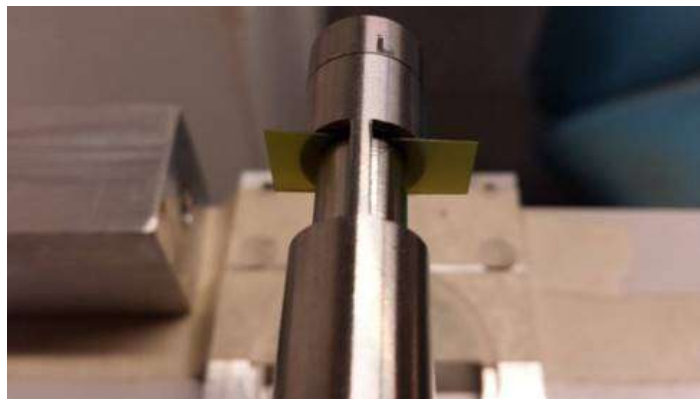


FIGURE 4.4: Picture of the terminating part of the optical fiber bundle with the RCF.

4.3 Dose calibration

The innovative dosimetry method was successfully tested with several types of RCFs. In order to demonstrate the operating principle of the method, the results, in terms of light spectra and dose calibration curves, of irradiations of EBT3 and XR-QA2 Gafchromic films with ^{60}Co gamma rays will be discussed in the following. Several physical observables can be exploited for the calibration of the films, depending on the dose range to be investigated. For example, there are wavelengths (e.g. $\lambda_{low}=633$ nm) for which the changes induced by low radiation doses are relatively high. The darkening at this wavelength saturates before than for another wavelength such (e.g. $\lambda_{high}=663$ nm). Furthermore, an average of the contributions of all wavelengths (e.g. the integral of the curve) has the advantage of being a trade-off between the different sensitivities of the wavelengths. The possibility of performing the data analysis in many ways gives a high level of versatility to this method, allowing the extension of the dynamic range of some types of films by more than one order of magnitude. EBT3 Gafchromic film samples were exposed to ^{60}Co -gamma rays from ISOF-CNR gamma facility at Bologna. The two Gamma-cell (discussed in section 2.2) provide a High Dose-Rate (HDR) of 3.33 Gy/min and a Low Dose-Rate (LDR) of 0.13 Gy/min from the decay of the ^{60}Co . During the irradiation, the fiber bundle and the film, i.e. the terminating part of the RCF reading set-up (Fig. 4.4), were positioned in the centre of the irradiator, while the light source and the spectrometer were remotely controlled.

Figure 4.5 shows the spectra corresponding to the exposure of an EBT3 Gafchromic film in the HDR-irradiator for ten minutes irradiation. In this first experiment the holder with the Teflon cylinder was used, implying an integration-time of the spectrometer of 1.3 s. The spectra are zoomed in the wavelength region 500-700 nm. The spectrometer acquires one spectrum for each integration-time (1.3 s). This amount of time corresponds to a dose on the film of 42 mGy. The effect of the ionizing radiation on the film consists in an integral reduction of the counts. As a consequence of this, the different curves represent the trend in time of the darkening of the film, that is the trend of the dose absorbed by the film. The first curve of Fig. 4.5 (blank) corresponds to 0 Gy on the film (no exposure to ionizing radiation). The second curve, with a reduced number of counts, corresponds to a dose of 0.3 Gy. The third curve (0.6 Gy) has a subsequent reduction of the counts and so on. The maximum dose achieved in this experiment was 32.6 Gy.

4.3.1 Uncertainty analysis

The counts recorded by the spectrometer are affected by experimental uncertainties mainly related to the temperature of the light source. The contribution of the uncertainty of the counts due to the reproducibility was estimated to be less than 0.1% for a 2 hour acquisition made after 40 minutes from the switching on of the light source (time needed for the warm-up). However, in order to take into account any source of uncertainty such as possible instabilities of the light source, the overall uncertainty on the counts was considered the square root of the counts, in agreement with the *Poisson* statistics. This conservative approach overestimates the uncertainties of the counts of all calibrations from now on, without affecting the precision of

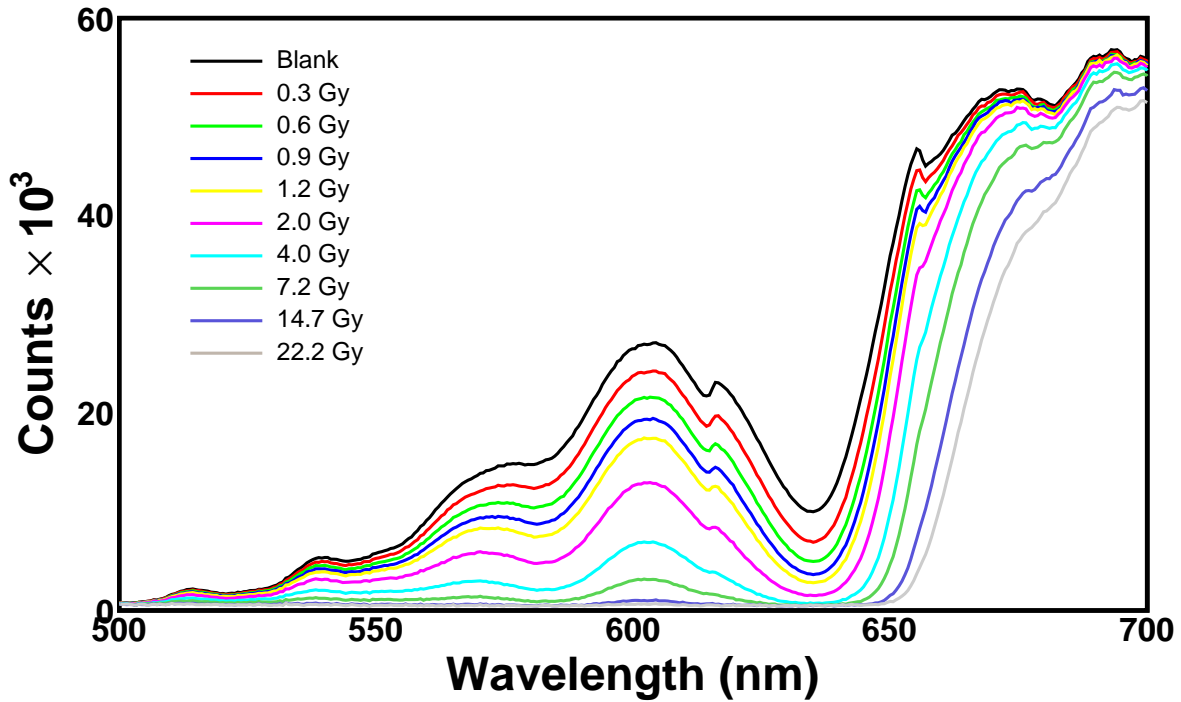


FIGURE 4.5: Spectra of an EBT3 Gafchromic film exposed to ^{60}Co gamma-rays from the HDR-irradiator. The integration-time is set to 1.3 s.

the method. In fact, the uncertainty of the counts was evaluated to be in any case less than 1%.

4.3.2 EBT3 Gafchromic films

The observation of the spectra of Fig. 4.5 suggests that the calibration can be performed by means of any reasonable physical observable. For example, the wavelength $\lambda_{low}=635$ nm, corresponding to the valley of the spectra of Fig. 4.5, can be used for an optimal discrimination of low doses.

Figure 4.6 shows the counts of the curves of Fig. 4.5 corresponding to the wavelength λ_{low} as a function of the dose. The uncertainty of dose values (evaluated to be less than 0.2% for all the calibration plots) was obtained by the propagation of the statistical uncertainties of the integration-time and dose-rate (both less than 0.1%). The observable λ_{low} is very sensitive up to about 3 Gy. In fact, with reference to Fig. 4.5, the gap of the counts between the first and second curve (blank and 0.3 Gy) is much bigger than that between the second and the third curve. This observable saturates above 6 Gy; beyond this value the determination of dose changes is not possible.

In order to get a good discrimination of higher doses, the wavelength $\lambda_{high}=663$ nm can be used for the calibration. Figure 4.7 shows the calibration of the film obtained by recording the counts of the curves of Fig. 4.5 corresponding to the wavelength λ_{high} . This observable allows very precise discrimination of dose in a wide dose range, from fractions of Gy to more than 30 Gy. The black curve is the polynomial that best fits to the experimental data. The goodness of the fit was quantified by

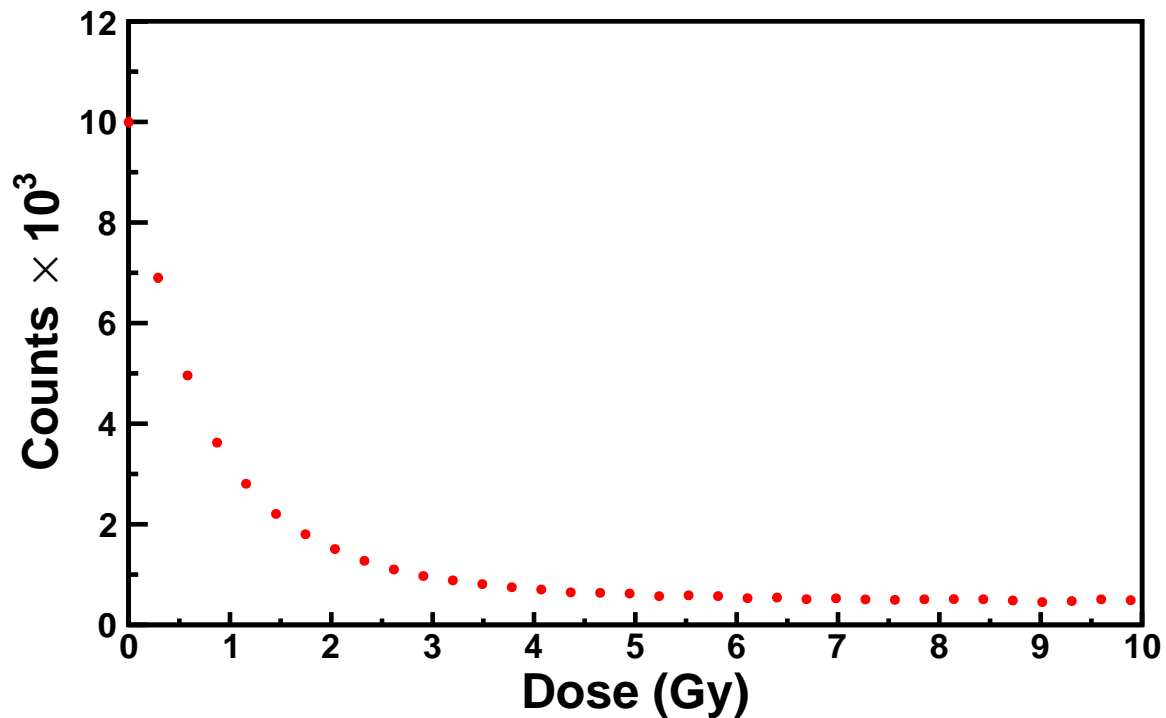


FIGURE 4.6: Counts corresponding to the wavelength $\lambda_{low}=635$ nm as a function of the dose. Above 6 Gy this observable is not useful for the calibration (saturation).

means of the chi-squared (χ^2) test. The values of the reduced chi-square (χ^2/ndf , where ndf is the number of degrees of freedom) and χ^2 -probability, respectively 0.3 and 1, of the calibration of Fig. 4.7 express the excellent agreement of the third-degree polynomial function with the experimental data. The inset of Fig. 4.7 reports the values of χ^2 , χ^2 -probability and the terms of the polynomial with the statistical uncertainties. It is noticeable that the value of the reduced chi-square less than 1 implies an overestimation of the variances, accordingly to the conservative hypothesis of the *Poisson* statistics.

The wavelength λ_{low} is not useful for the determination of doses greater than 3 Gy, although it is a very powerful observable for the discrimination of low doses. The minimum amount of dose detected by the spectrometer is determined by two factors: the dose-rate and the spectrometer integration-time (1.3 s). This value is fixed by the material employed for backscattering the light, i.e. the Teflon cylinder. With the aim of investigating a method for a better discrimination of low doses, an irradiation of an EBT3 Gafchromic film with the LDR-irradiator (dose-rate: 0.13 Gy/min) was carried out. Furthermore, in order to reduce the integration-time, the 1.5 μm Mylar foil was used as backscattering material. This set-up allowed the setting of the integration-time of the spectrometer to 260 ms. In this way, the spectrometer detects changes of the darkening of the film in a smaller time with respect to that with the Teflon cylinder.

Figure 4.8 shows the calibration of the EBT3 Gafchromic film obtained by recording the counts of the curves of the spectra corresponding to the wavelength λ_{low} as a function of the dose. The amount of dose absorbed by the film in one integration-

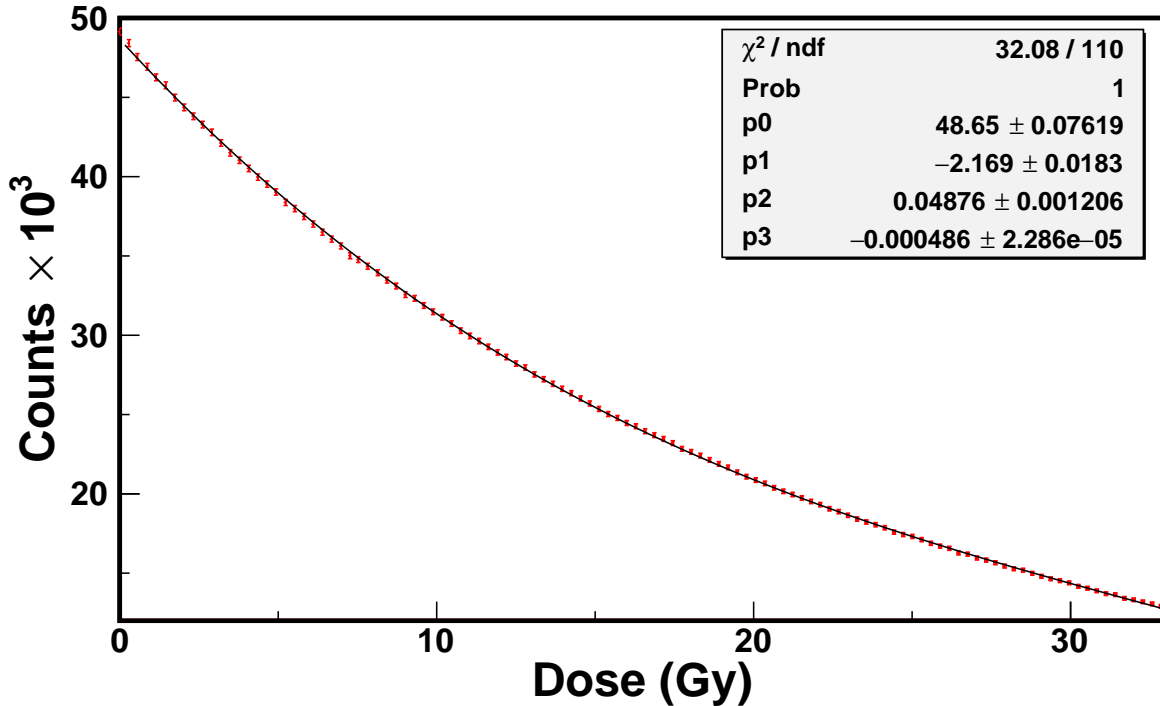


FIGURE 4.7: Calibration of an EBT3 Gafchromic film exposed to ^{60}Co -gamma rays of the HDR-irradiator. The counts corresponding to the wavelength $\lambda_{low}=663$ nm are used for the calibration. The black curve is the polynomial that best fits the data. The values of χ^2/ndf , χ^2 -probability and the terms of the polynomial are shown in the inset.

time is $560 \mu\text{Gy}$. The dose-trend of the experimental data of Fig. 4.8 is the same of Fig. 4.6 and Fig. 4.7, i.e. the data are very well represented (see values of χ^2/ndf and χ^2 -probability in the inset of 4.8) by a fifth-degree polynomial function (black curve in Fig. 4.8). The dose-axis goes from a few mGy to 1.2 Gy. The discrimination of such values of dose is a novelty for dose measurements with EBT3 Gafchromic films, defined by the manufacturer sensitive from tenths to dozens of Gy. Figure 4.8 shows also the zoom of the main plot in the dose-range from a few up to 30 mGy. It is noticeable that, in order to evaluate the minimum detectable dose obtained with this method, by preserving the statistical uncertainty, the integration-time must be reduced without causing unavoidable losses of the counts in the spectra. This could be achieved by means of thin high-reflecting materials. This point will be object of next studies.

4.3.3 XR-QA2 Gafchromic films

As already mentioned in the previous sections, some types of RCFs have a particular structure which is suitable for this innovative method. For example, XR-QA2 Gafchromic films have an opaque layer, allowing the use of the film itself as backscattering material. For this reason, an irradiation of an XR-QA2 Gafchromic film in the LDR-irradiator was carried out.

Figure 4.9 shows the spectra corresponding to the exposure of an XR-QA2 Gafchromic film in the LDR-irradiator for ten minutes irradiation. The spectra are zoomed in the

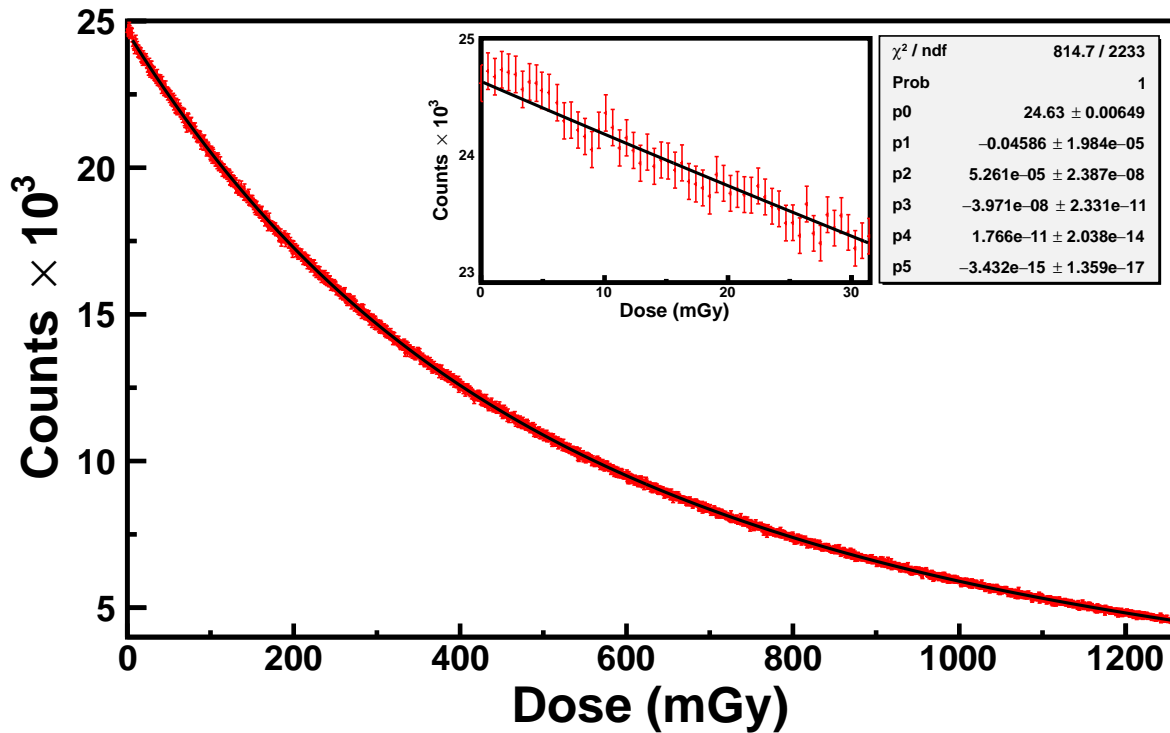


FIGURE 4.8: Calibration of an EBT3 Gafchromic film exposed to ^{60}Co -gamma rays of the LDR-irradiator. The counts corresponding to the wavelength $\lambda_{low}=635$ nm are used for the calibration. The black curve is the polynomial that best fits the data. The zoom of the main plot in the range of dose [0-30 mGy] is shown in the first inset. The values of χ^2/ndf , χ^2 -probability and the terms of the polynomial are shown in the second inset.

wavelength region 530-640 nm. The integration-time was set to 1.9 s. The dose absorbed by the film in one integration-time is therefore 4 mGy. Figure 4.10 shows the calibration of the XR-QA2 Gafchromic film obtained by recording the counts of the curves of Fig. 4.9 corresponding to the wavelength λ_{low} . It is noticeable that the Gafchromic film XR-QA2 shows characteristic spectra and calibration curves similar to that of the EBT3 model. In particular, the fifth-degree polynomial curve (the values of the terms are shown in Fig. 4.10) represents the best fit of the experimental data. The values of χ^2/ndf and χ^2 -probability are 0.8 and 1 respectively. This curve spans over a wide range of dose from some mGy to 3 Gy. The zoom of the main plot for the dose region 0-200 mGy is also shown in Fig. 4.10.

4.4 Discussion and outlook

The proposed RCF reading method is based on the use of optical fibers that transport the light from a source, such as a halogen or deuterium light source, up to the RCF. During the exposure to ionizing radiation, the optical changes of the film are real-time detected by a light-collecting fiber and sent back to a spectrometer for data analysis. A proper scattering material can be used, if needed, to increase the

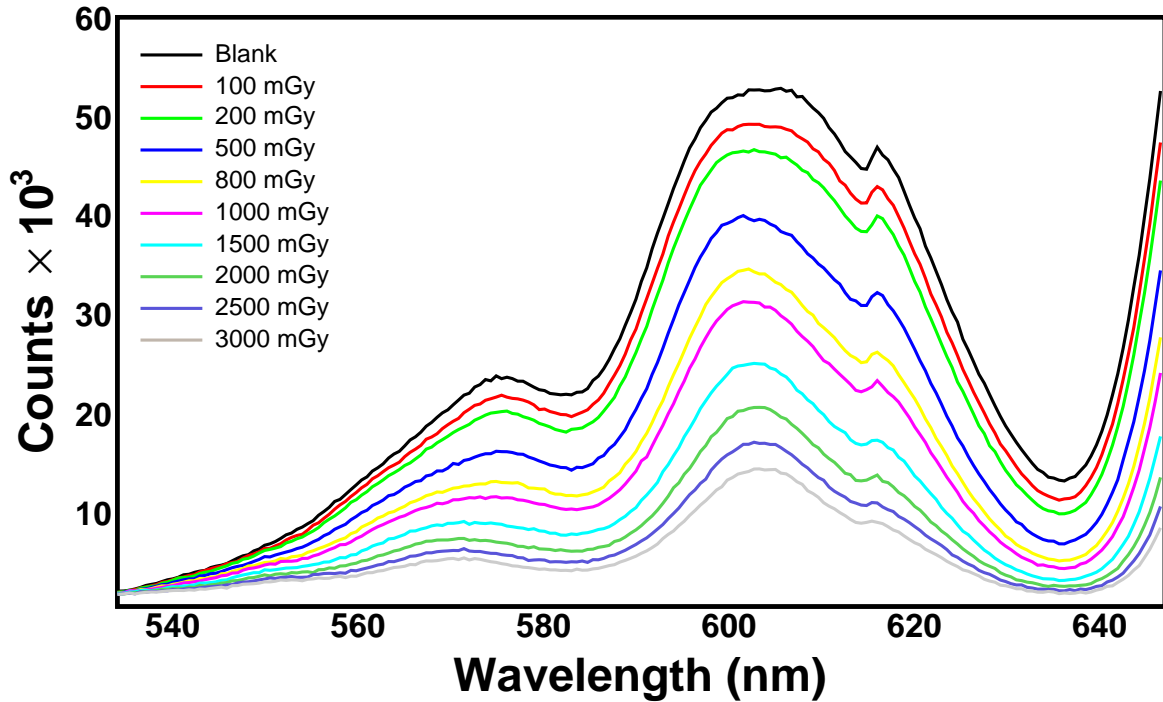


FIGURE 4.9: Spectra of an XR-QA2 Gafchromic film exposed to ^{60}Co gamma-rays from the LDR-irradiator. The integration-time is set to 1.9 s.

amount of light in the collecting fiber. This allows the reduction of the integration-time of the spectrometer, affecting ultimately the minimum detectable dose. The method was tested for several RCF types, showing excellent performances in terms of accuracy and precision. The results of exposures of two types of films (EBT3 and XR-QA2 Gafchromic model) to ^{60}Co -gamma rays at two dose-rates (3.33 and 0.13 Gy/min) are reported. The structures of these two types of films include all typologies of commercial RCFs. In fact EBT3 Gafchromic films have the active layer sandwiched between two polyester substrates and XRQA-2 Gafchromic films have the active layer deposited on an opaque polyester substrate. As far as the first typology, the employment of a backscattering material is needed for increasing the amount of light while for the second, the opaque layer can be itself the backscattering material. The versatility of the method relies on many factors, among which the capability of performing the dose calibration by means of more criteria of data analysis. For example, the counts corresponding to the characteristic valley of the spectra, i.e. the wavelength $\lambda_{low} = 635$ nm, can be put in relation to the dose on the RCF. The subsequent calibration, based on a proper choice of the backscattering material, shows that the dynamic range of some types of films is higher with respect to what declared by the manufacturer. In fact, EBT3 Gafchromic films are sensitive up to dozens of Gy by means of analysis with commercial reading instruments. The proposed dosimetry method clearly allows the detection of doses of mGy with EBT3 Gafchromic films. Different data analysis techniques can be exploited for the investigation of a specific dose range. For example, by recording the counts of the spectra corresponding to the wavelength $\lambda_{high} = 663$ nm, it is possible to perform a calibration for better discriminate the high doses. The evaluation of measurement

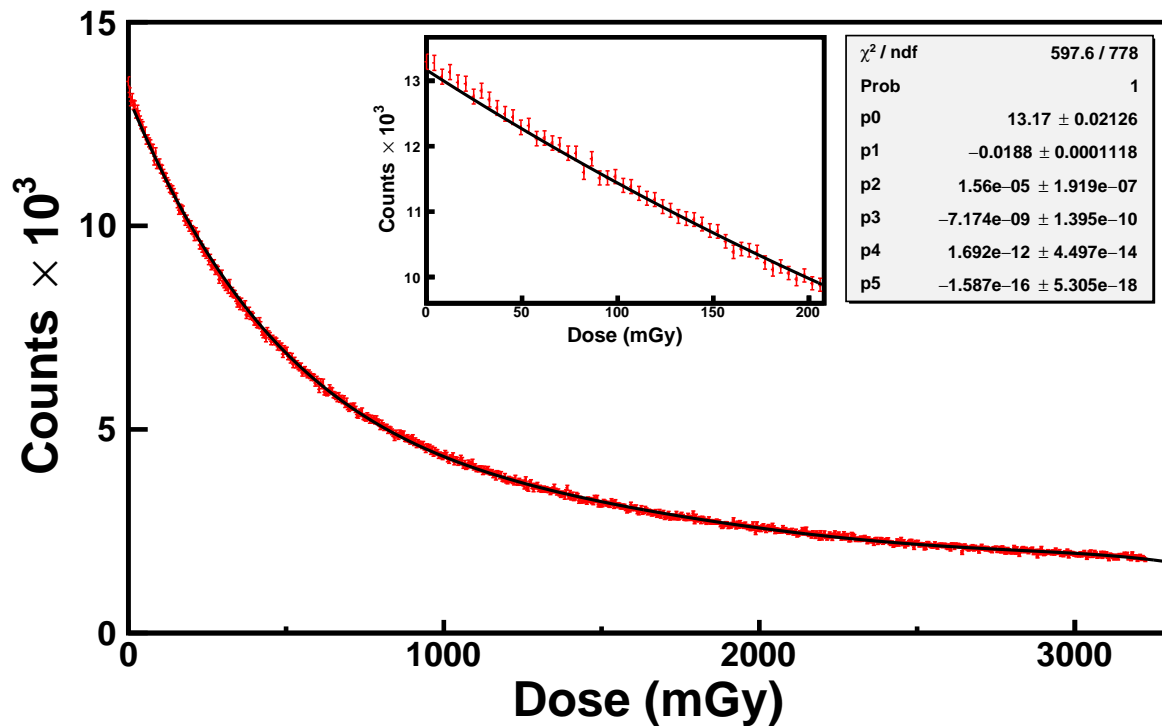


FIGURE 4.10: Calibration of an XR-QA2 Gafchromic film exposed to ^{60}Co -gamma rays of the LDR-irradiator. The counts corresponding to the wavelength $\lambda_{low}=635$ nm are used for the calibration. The black curve is the polynomial that best fits the data. The zoom of the main plot in the range of dose [0-200 mGy] is shown in the first inset. The values of χ^2 / ndf , χ^2 -probability and the terms of the polynomial are shown in the second inset.

uncertainties has been made by means of a precautionary approach, based on the *Poisson* statistics, allowing uncertainties within 1% for all the calibration plots (Fig. 4.7,4.8 and 4.9). The advantages of the proposed method with respect to the state of the art are manifold. Firstly, the real-time dosimetry with RCFs can be performed by monitoring the dose from a remote position with an optical fiber probe, exploiting all the potential of optical fibers such as micrometric thickness, low attenuation coefficient and no interaction with electromagnetic fields. The irradiation of small areas (less than 1 mm^2) of commercial RCF allows multiple exposures and readings of the same RCF up to the saturation. This dosimetry method finds applications in all fields of radiation physics where RCFs are employed (figure 3.2). For example, in radiation hardness applications, the dose can be real-time monitored on the device. This allows also to consider any beam instabilities at particle accelerators (spatial divergence or changes in the flux). Other applications are the on-line monitoring (in-vivo) of dose delivered on patients in photon and ion therapy. Each application has its own specific requirement in terms of sensitivity, dynamic range, accuracy as well as physical dimensions of the instruments employed and their cost. On this line, next studies are aimed at studying the miniaturization of the present dosimeter and the improvement of the stability of optical signals at distances of the order of 2-3 meters. This work will be carried in 2019 within the framework of the INFN

OPTORAD project.

Chapter 5

Innovative neutron detector

In chapters 3 and chapter 4 we discussed innovative detection systems for electromagnetic X/gamma and charged particles radiation. Neutrons are of primary interest in many areas of applied and fundamental physics. The applications of neutrons range from the determination of elemental composition using Neutron Activation Analysis (NAA) to neutron radiography, neutron scattering in the characterization of materials and minerals (in particular oil exploration). There is also a high interest to neutrons in medical physics applications. The Boron Neutron Capture Therapy (BNCT) and Fast Neutron Therapy (FNT) use neutrons as primary particles to damage the cancer cells. In addition, both in photon and ion therapy, the production of secondary neutrons is unavoidable and an accurate knowledge of their characteristics is needed. Furthermore, in nuclear physics experiments, in particular with radioactive neutron-rich ion beams, measurements of neutron spectra are fundamental for assessing properties of nuclei. These demands prompted the researchers in the last few years to study and develop new kinds of neutron detectors. Polysiloxane-based scintillators are innovative detectors recently developed at Laboratori Nazionali di Legnaro (LNL). These detectors belong to the class of plastic scintillators like polyviniltoluene and polystyrene with the advantage respect to the latter of being non-toxic and more resistance to radiations. For such reasons these detectors are promising for work in harsh environment. This chapter presents the full characterization that we performed of one sample of polysiloxane-based scintillator. Since the performances of this detector were unknown, we started our work by comparing the response of the new detector to that of a well-established inorganic scintillator such as the NaI scintillator. The response of the new detector to mono-energetic gamma radiation is the typical response function of organic scintillator. The calibration of this scintillator can be accomplished by analyzing the Compton Edge of single gamma energies. On this line we performed the calibration with the Compton Edges of radionuclides as the ^{137}Cs , ^{22}Na and ^{60}Co . The gamma characterization is discussed in sections 5.2, 5.3 and 5.4. Section 5.1 discusses the promising characteristics of this new type of scintillators. Successively the pulse height spectra to incident charged particles are analyzed in section 5.5. The Pulse Shape Discrimination capabilities of the polysiloxane detector to many radiation (gamma, alpha, neutrons) are studied and results are reported. In particular the Charge Comparison Method (CCM) was employed for discriminating several incident radiation. Methods and results are reported in section 5.6.

5.1 Introduction

Polysiloxane (PS) based scintillators belong to the class of organic plastic scintillators which operating principle has been discussed in section 2.9. This kind of scintillator has been developed in the recent years at INFN-Laboratori Nazionale di Legnaro (LNL) within the framework of the INFN project ORIONE (ORganic scIntillatros fOr NEutrons) (Quaranta et al., 2011). The main advantage of PS scintillators over traditional plastics, among which polyvinyltoluene and polystyrene, relies in the high resistance and thermal properties (Carturan et al., 2010). In particular, the low toxicity and flammability together with chemical inertness are the main characteristics allowing the employment of these detectors in several geometries and configurations. For such reasons, PS scintillators are promising for employment in harsh environments. The low cost is a not less important factor in particular for apparatuses of experiments of nuclear physics where significant large volumes of detectors are typically needed (Jaworski et al., 2012). The plastic scintillators are usually made up of a polymer matrix in which a suitable scintillating material, a dye, is dissolved in fractions of the order of some percent. The detection mechanism consists in the interaction of the incident radiation with the scintillating the matrix and subsequent energy transfer to the dyes. Since the sensitivity of photomultiplier tubes (PMTs) depends on the wavelength, a second dye, called wavelength shifter, is dissolved in the scintillating matrix.

5.2 Preliminary characterization and measurements

The PS sample that we have fully characterized is shown in the picture of figure 5.1.



FIGURE 5.1: Polysiloxane-based detector with 8% PPO.

It uses the 2,5-diphenyloxazole (PPO) as primary dye in concentration of 8% added to the PS matrix. The scintillator was coupled to the Hamamatsu PMT model R6233. The optical coupling between the detector and the photocathode was accomplished by using the optical grease Viscasil which allows excellent optical performances and minimal losses of light. The PS scintillator and PMT were covered

by commercial Teflon and by a $1.5 \mu\text{m}$ Al-Mylar foil. Finally, aiming to reduce the dark counts as much as possible, a thermo-shrinkable polystyrene was used for covering the whole scintillator-PMT system (figure 5.1). The operating bias was found to be -1400 V . The PMT was fed into a CAEN Desktop Digitizer (model DT5720C, ADC: 12 bit, 250 MS/s) connected to a computer for data analysis. This digitizer is suitable for measurements of Pulse Shape Analysis (PSA) necessary for neutron detection. In fact, an FPGA dedicated for these purposes allows the management of a real time Digital Pulse Processing (DPP) consisting in a Charge Integration (DPP-CI) and Pulse Shape Discrimination (DPP-PSD) software for PSA. Figure 5.2 shows the schematics for the measurement with the PS scintillator that described in next sections.

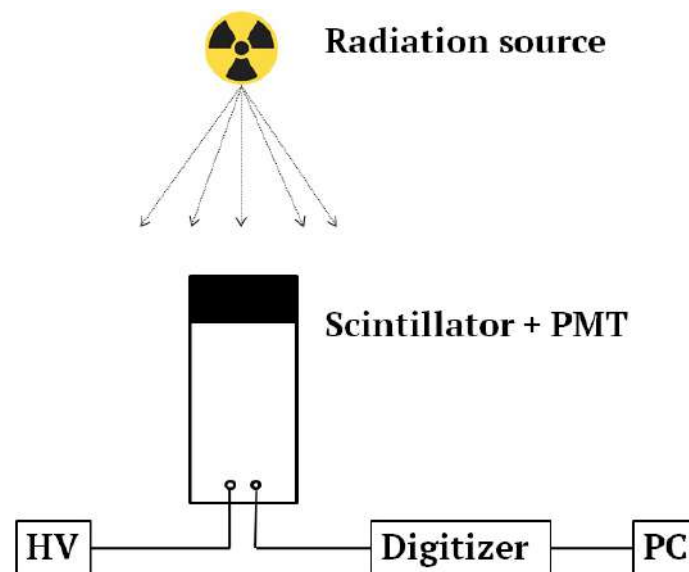


FIGURE 5.2: Scheme of electronic setup for the measurements with the poly-siloxane scintillator.

5.3 Characterization with gamma radiation

Before performing neutron measurements, the full characterization of the PS scintillator to common laboratory radioactive sources (gamma and alpha) is necessary. In this section the method exploited for the calibration are discussed. Since the performances of this detector were unknown, we compared its response function to that of common inorganic scintillator as the NaI. We measured the spectra of gamma emitters to single energy as ^{137}Cs , ^{22}Na and ^{60}Co radioisotopes. Table 5.1 shows the full energy peaks and Compton energies of these radionuclides.

Figure 5.3 shows the spectra (of the radionuclides reported in table 5.1) measured with the NaI scintillator.

The NaI scintillator is an inorganic scintillator with high density and atomic number and suited dimensions; therefore both the full energy peaks and Compton edges are clearly visible. Figure 5.4 shows the pulse height spectrum for gamma exposure to ^{137}Cs source.

TABLE 5.1: Full energy peaks and Compton energies of the radionuclides used for the calibration of the PS scintillator.

Radionuclide	Full energy peak (keV)	Compton Edge (keV)
^{137}Cs	662	478
^{60}Co	1173	963
^{60}Co	1332	1118
^{22}Na	511	341
^{22}Na	1274	1061

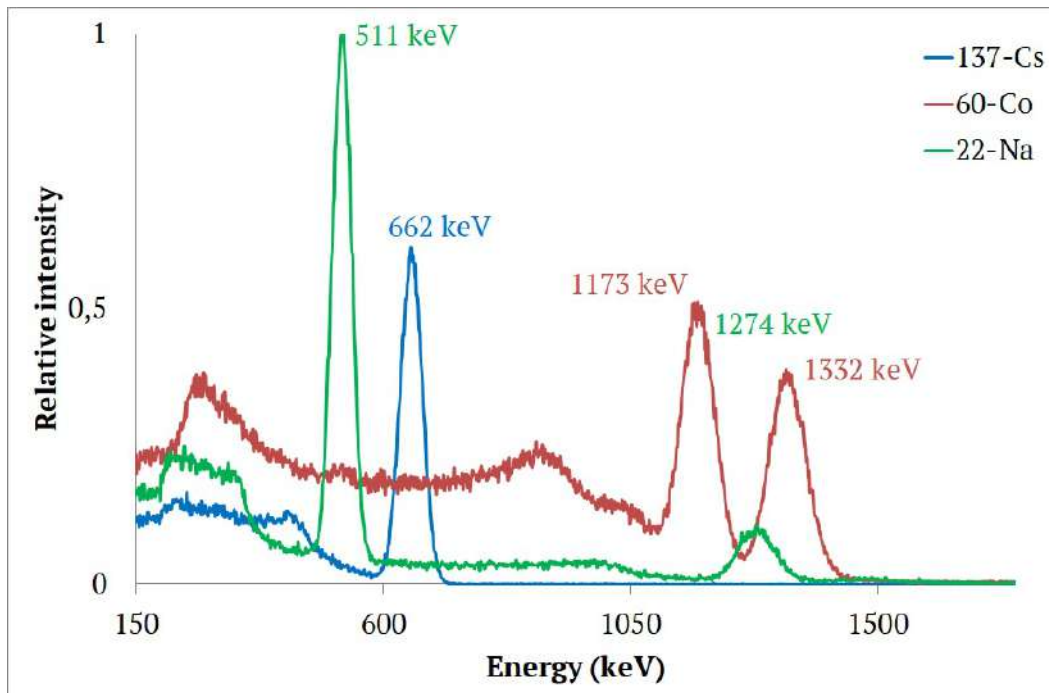


FIGURE 5.3: Spectra of ^{137}Cs , ^{60}Co and ^{22}Na radio-nuclides measured with a NaI scintillator.

Owing to the low density and atomic number of the PS matrix and to the relative small detection volumes, the full energy peak is non visible. The secondary electrons produced by interaction of gamma rays with the scintillator generate only the Compton Edge, which is therefore the only representative of the incident gamma energy. Figure 5.5 shows the pulse height spectrum of the silicon scintillator to gamma from ^{22}Na .

Since the ^{22}Na has two main peaks at the energy of 511 and 1274 keV, this results in the observation in figure 5.5 of two Compton Edges. The low intensity of the source employed results in a bad definition of the Compton Edges compared to the spectrum of figure 5.4. However, these are clearly observable. Figure 5.6 shows the pulse height spectrum of the silicon detector to gamma from ^{60}Co source.

Since the two peaks of ^{60}Co have near energies, the main peak of figure 5.6 corresponds to the first Compton Edge which is superimposed to the flat part of the

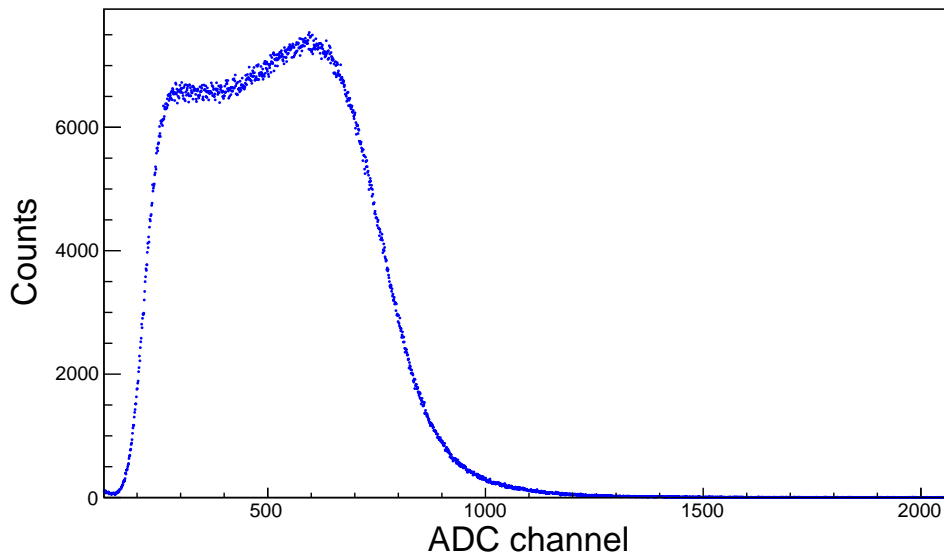


FIGURE 5.4: Pulse height spectrum of ^{137}Cs gamma (662 keV).

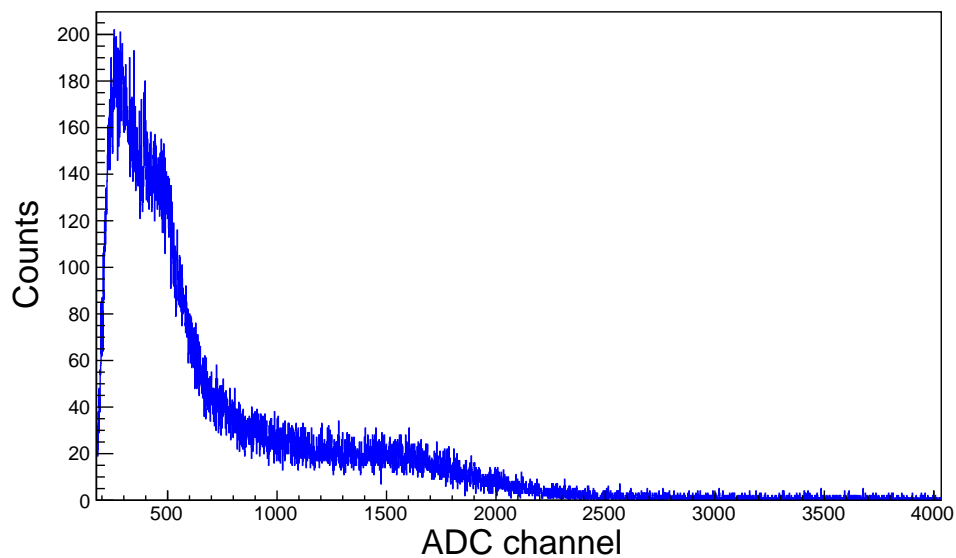


FIGURE 5.5: Pulse height spectrum of ^{22}Na gamma (511 and 1227 keV).

higher energy, while the Compton Edge relative to the 1.33 MeV photons is not visible. This is due to the energy resolution of the detector. For some organic scintillators, in fact also the second ^{60}Co peak is visible as shoulders at higher channels (Dalla Palma et al., 2015).

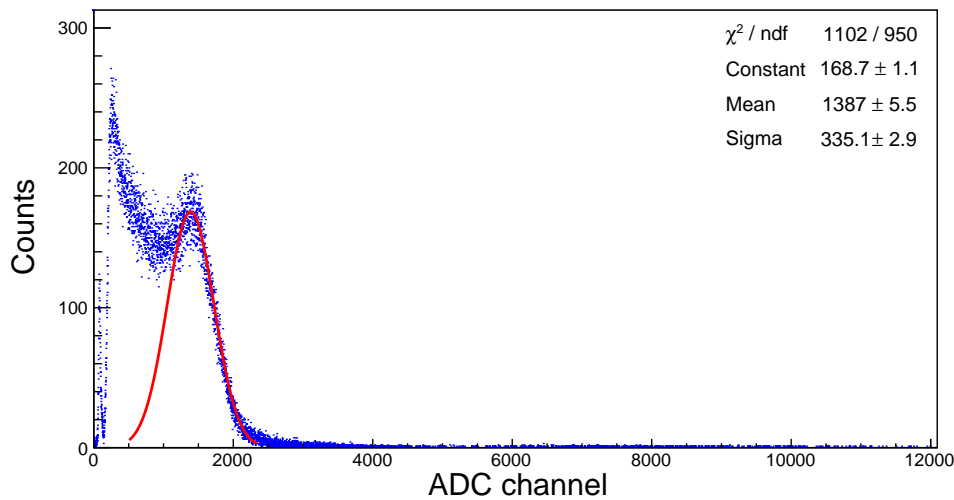


FIGURE 5.6: Pulse height spectrum of ^{60}Co gamma (1173 and 1332 keV).

5.4 Calibration of the PS scintillator

The spectra of figure 5.4, 5.5 and 5.6 show the characteristic response function of organic scintillators. In order to perform the calibration of the PS scintillator, the position of the Compton energy has to be determined. Since the position of Compton energy in the spectra can be in principle at a channel between the Compton Edge and its tail at higher channels, its determination is not trivial. Several criteria can be followed for the determination of the Compton energy in organic scintillators and there is no general approach (Batchelor et al., 1961; Cherubini et al., 1988; Flynn et al., 1964). For example, the following criteria can be used (see figure 5.7): 1) the Compton Energy corresponds to the channel E_m , 2) to the channel $E_{1/2}$ and 3) to the channel at half way between E_m and $E_{1/2}$.

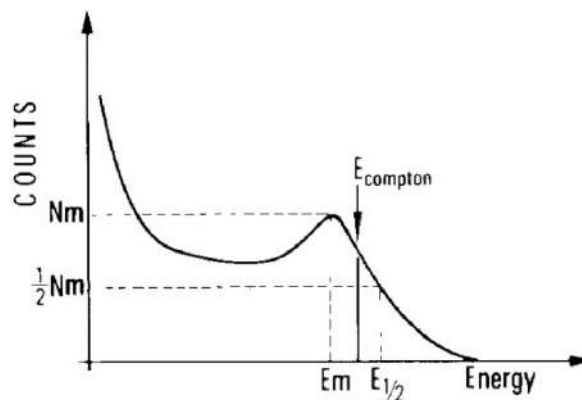


FIGURE 5.7: Methods for the determination of the Compton energy.

The choice of one method rather than another depends on the type and characteristics of the detector and in particular on the energy resolution. Here we compared these three methods for the PS scintillator. The first step consists in determining the

position of the Compton Edges E_m . To do this a gaussian fit has been performed. As an example, the red curve in figure 5.6 represents the gaussian best fit of the ^{60}Co Compton Edges; the fitting parameters (centroid, sigma and full width half maximum) are reported in the inset of figure 5.6. Figure 5.8 shows the calibration of the PS scintillator with the three methods above discussed for the determination of the Compton energy.

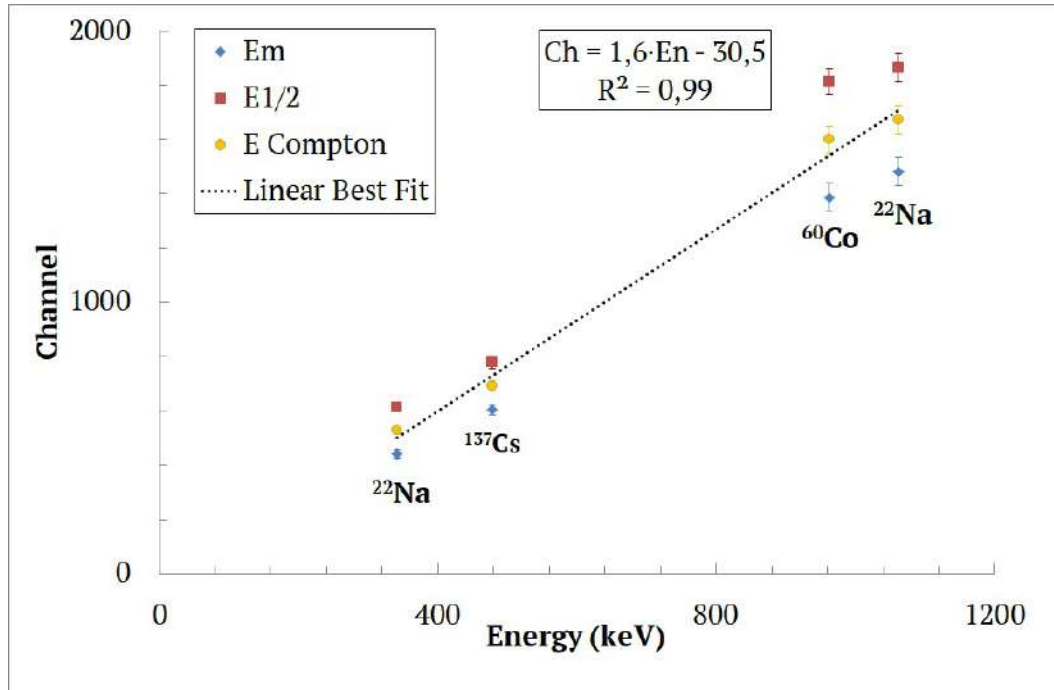


FIGURE 5.8: Calibration of the silicon detector.

In the case of the PS scintillator, the Compton energy was found to be the channel at half way between E_m and $E_{1/2}$, namely E_{Compton} in figure 5.7 and figure 5.8. The equation of the straight line that best fit to experimental data (calibration) was found to be:

$$E_{\text{gamma}}(\text{keV}) = 19.1 + 0.6 \cdot \text{Channel} \quad (5.1)$$

5.5 Pulse height spectra for charged particles

Neutron scintillators are strongly radiation-type dependent. In order to characterize the response of the detector to several incident radiation, exposures of PS scintillators to alpha particles from common laboratory sources such as ^{241}Am were carried out. Figure 5.9 shows the pulse height distribution of the PS scintillator to alpha particles from ^{241}Am source.

The calibration found in the previous section (eq. 5.1) is valid only for photons and electrons (the signals from photons are in fact due to secondary electrons). The peak at channel 275 in figure 5.9 corresponds to the energy of incident alpha particles that is 5.48 MeV. The application of the calibration found in the previous section would result in an energy for alpha particles of 184 keV. It is therefore convenient to

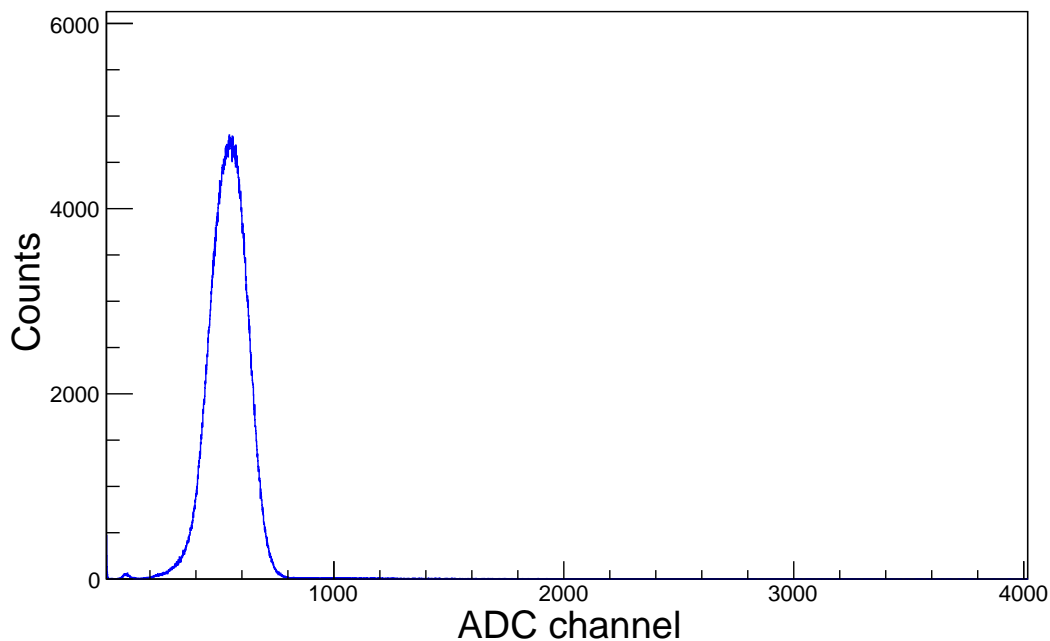


FIGURE 5.9: Response of the silicon detector to ^{241}Am alpha particles.

refer to the energy of a neutron scintillator in units of electron-Volt electron equivalent (eVee).

5.6 Charge comparison method

Careful studies of the signals of the PS scintillator allow the discrimination of the incident radiation type by means of techniques of Pulse Shape Discrimination (PSD). These topics have been introduced in section 2.9 for organic scintillators. Here we focus on Charge Comparison Method (CCM) (Cester et al., 2014; Wolski et al., 1995), the PSD technique used in this work. In order to discuss the principle of the CCM, let us consider the typical output signals from CAEN digitizer, shown in figure 5.10.

The signals representing gamma (black) and neutron (red) radiation have similar shape with a small difference in the tail (see inset in figure 5.10). The Digital Pulse Processing (DPP) allows PSD with the generation of two additional gates. With reference to figure 5.10 the short gate is highlighted in green and the long gate in blue.

The PSD parameter is defined as:

$$PSD = \frac{Q_{tot} - Q_{tail}}{Q_{tot}} = 1 - \frac{Q_{tail}}{Q_{tot}} \quad (5.2)$$

where Q_{tot} is the area of the signals under the long gate and Q_{tail} is that under the short gate. Gamma signals have a PSD parameter lower than that of neutrons. The typical representation of the PSD is a two-dimensional scatter plot in which the PSD parameter is on y-axis, the channel or energy is on the x-axis and the number

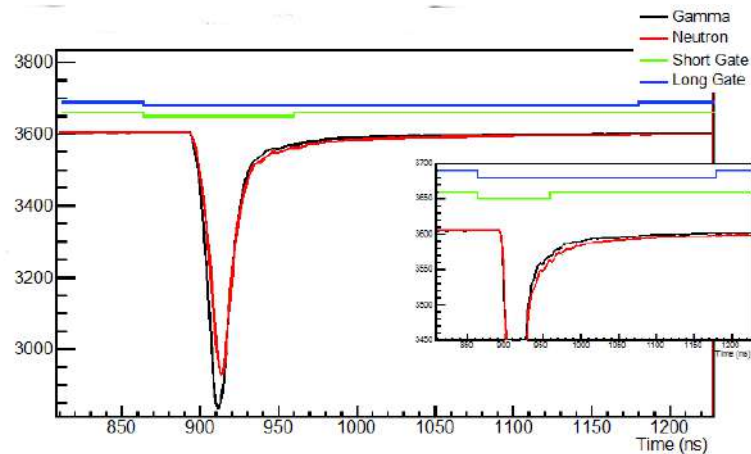


FIGURE 5.10: Neutron and gamma signals from CAEN digitizer. Differences of pulse shape are visible in the tail of the signals.

of events in the two-dimensional bin is on the z-axis. Figure 5.11 shows the measured scatter plot (PSD vs. energy) relative to the exposure of the PS scintillator to alpha from ^{241}Am and gamma from ^{137}Cs sources. The PSD parameter is calculated accordingly to eq. 5.2 and the energy is expressed in units of keVee.

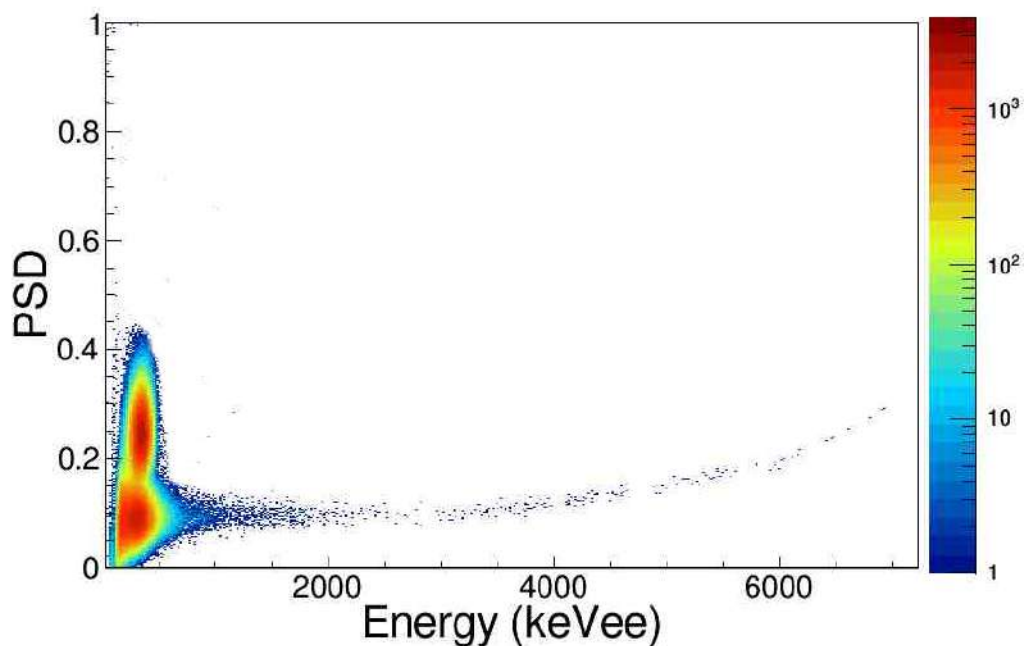


FIGURE 5.11: 2D scatter plot. The main spots represent gamma and alpha particles.

The main spots represent gamma (PSD parameter ~ 0.09) and alpha particles (PSD parameter ~ 0.25). The PSD capabilities of a neutron scintillator are expressed in terms of the Figure of Merit (FOM).

Figure of Merit

The Figure of Merit (FOM) is defined as:

$$FOM = \frac{s}{\Gamma_{\lambda} + \Gamma_x} \quad (5.3)$$

where s is the difference between the centroids of the peaks of gamma and the radiation type "x" (it can be alpha, protons, neutron etc.) and Γ is the FWHM of the corresponding gaussian peak. It should be noted that this parameter gives an information of the PSD capabilities of a scintillator but it is not an absolute indicator. As an example, figure 5.12 shows three different distributions giving rise to the same value of 0.85 to the FOM.

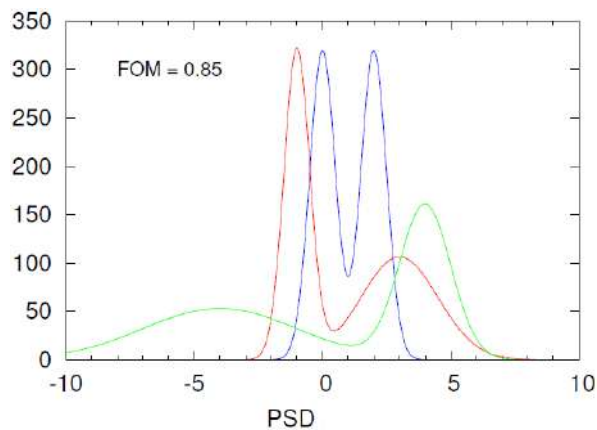


FIGURE 5.12: Three different distribution that give rise to the same value of FOM, in this case 0.85

Evaluation of the FOM

Figure 5.13 shows the 1D projection on the PSD axis of the scatter plot of figure 5.11.

The two peaks at PSD parameter of ~ 0.09 and ~ 0.25 represent gamma and alpha incident radiation respectively. The red curve in figure 5.11 is the best fit of the experimental data. The number of entries, the chi-squared, the chi-squared probability and the fitting parameter (constant, centroid and FWHM of the two gaussian) are shown in the inset of figure 5.13. The best fit of these data gives rise to a value of FOM of 1.2. The calculated uncertainty of the FOM is negligible. The parameter of the total FOM does not take into account that the separation between gamma and alpha radiation depends on the incident energy. 1D projections of the 2D scatter plot of figure 5.11 are represented in figure 5.14 at energies of 239, 297, 355, 412, 470 and 527 keVee (± 20 keVee).

The FOM was evaluated for each plot of figure 5.14. The results are reported in 5.15.

The PS scintillator allows a good discrimination with a maximum total FOM=1.2 for photons and alpha particles. The uncertainty is negligible.

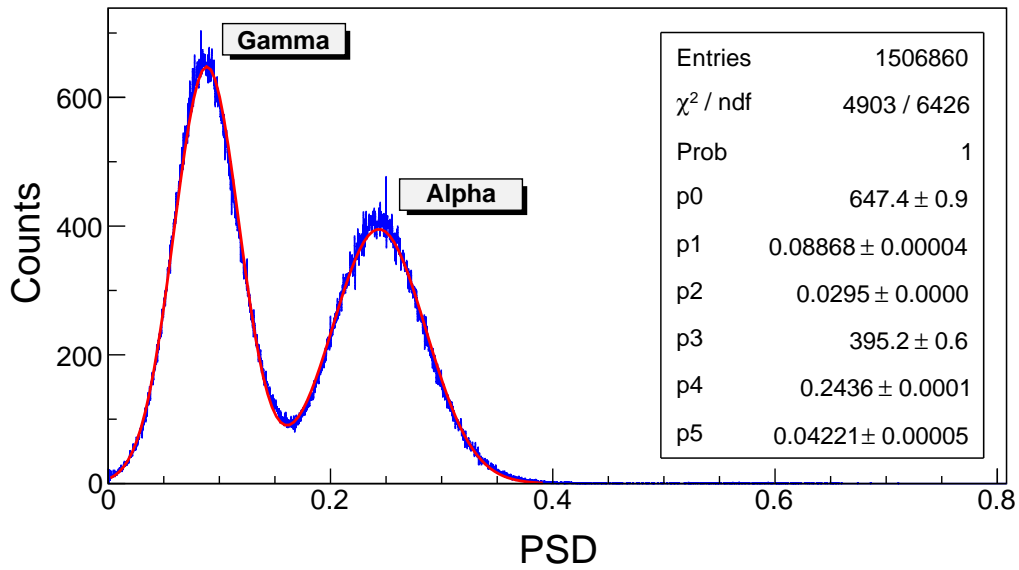


FIGURE 5.13: 1D projection on the PSD axis of the scatter plot of figure 5.11 .

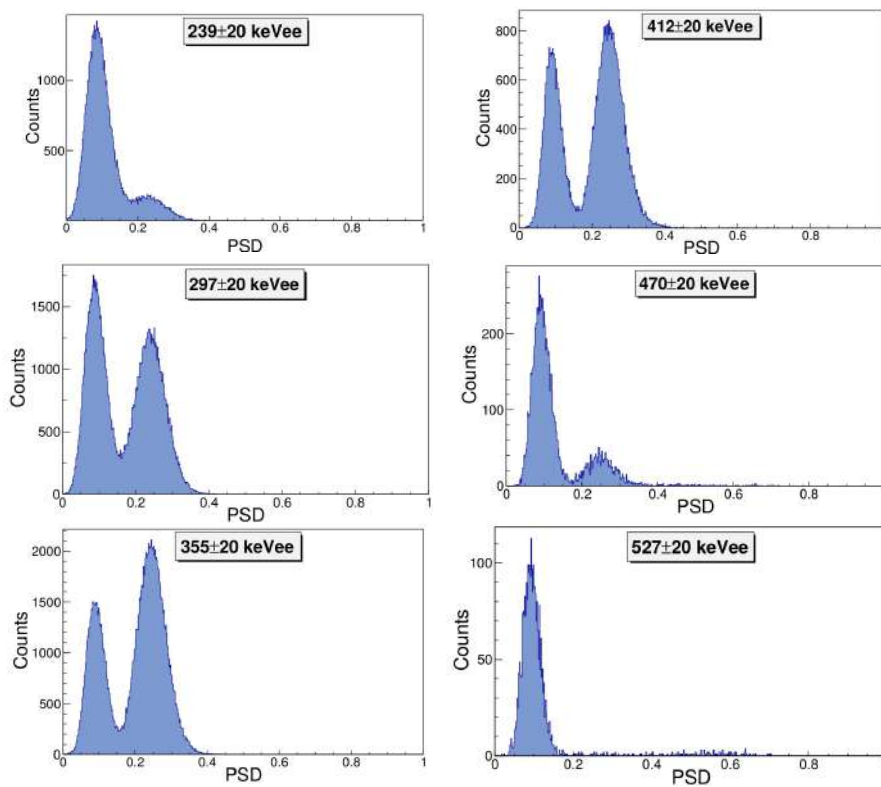


FIGURE 5.14: 1D projection on the PSD axis of the 2D scatter plot of figure 5.11 for different energies.

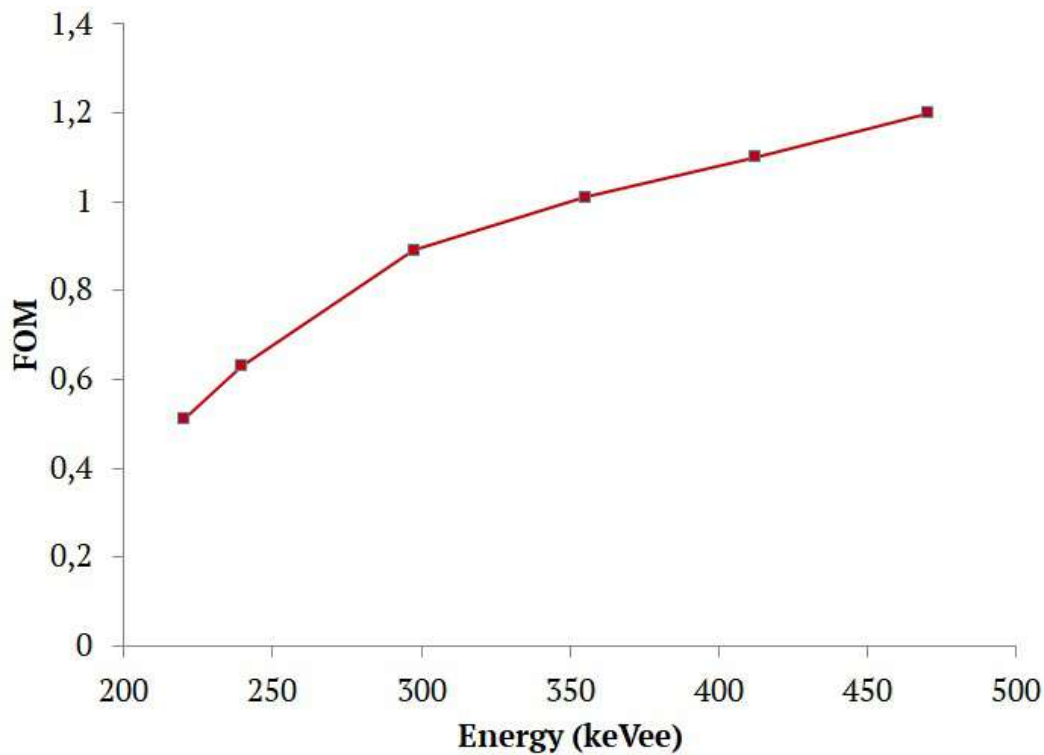


FIGURE 5.15: FOM at different energies.

5.7 Test with Am-Be neutron source

In order to test the response function of the PS scintillator to neutrons, a measurement was performed with an Am-Be source. In section 2.8 the main sources of neutrons obtainable with radioactive alpha sources were discussed. The Am-Be is very used in the applications and provide a neutron spectrum (reported in figure 2.18) with two main energy peaks around 4 and 5 MeV and extends up to 11 MeV. The source employed emits 2000 neutrons per second over the solid angle. Figure 5.16 shows the 2D scatter plot representing the response of the PS scintillator to neutrons from Am-Be source.

Since the number of neutrons emitted by the source was known with high precision, a first estimation of the PS efficiency ϵ was performed. It was found to be $\epsilon = 15.1 \pm 0.2$. Since the efficiency of a scintillator strongly depends on the energy of incident radiation, more accurate measurements have to be done. Such a measurement will be performed at LNS tandem within the framework of the experiment INSPIRED (*Investigation of Neutron Search for Production Reactions and Detection*) approved by the PAC of LNS. Other estimates of the efficiency of the PS scintillator have been already performed at LNS tandem accelerator and the results are discussed in section 6.2.

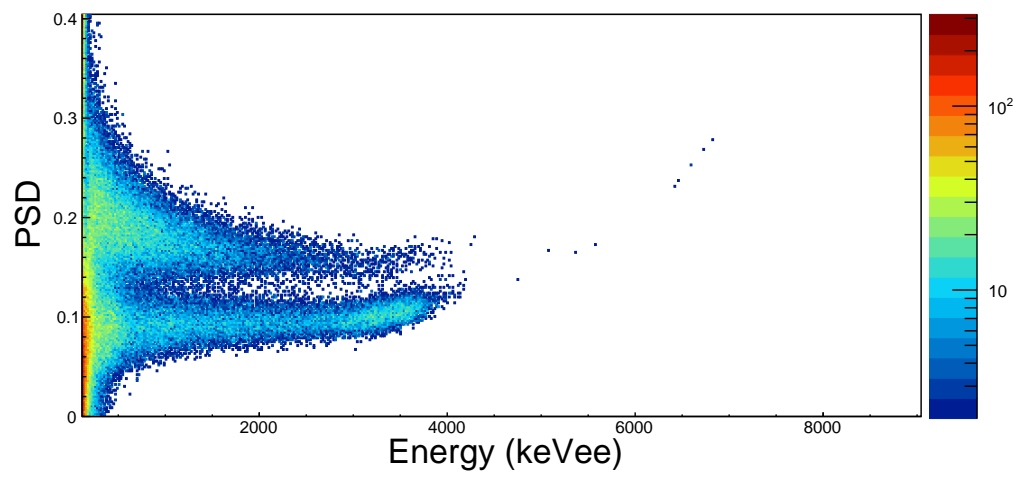


FIGURE 5.16: 2D scatter plot of measurements with AmBe source.

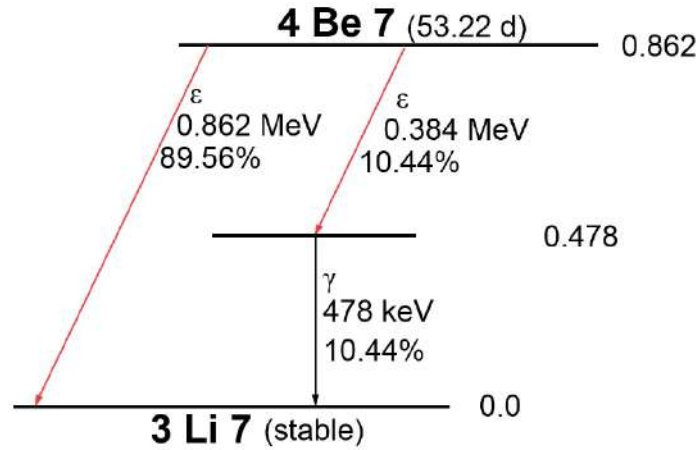
Chapter 6

Fast neutron production

The availability of well-characterized fast neutron beams is fundamental for radiation tests of electronic devices for terrestrial and avionic radiation hardness applications. Currently there are facilities that produce neutron beams for these applications. The most important were described in section 2.8. Owing to the increasing demand in the applications involving fast neutrons (discussed in the introduction of chapter 5), it is of great interest to exploit the existing particle beam facilities to accelerator-based neutron sources. In this chapter we discuss the nuclear reactions and methods that we employed for the production of quasi-monoenergetic and polychromatic neutrons at two charged-particle accelerators. In particular, we implemented for the first time a neutron beam line at the IBA 18/18 medical cyclotron of University of Bern; in addition we produced fast neutron beams at the tandem accelerator of Laboratori Nazionali del Sud (LNS) in Catania. The ${}^7\text{Li}(p,n){}^7\text{Be}$ reaction, used in both experiments, is one of the most interesting reactions (mentioned in section 2.8) for the production of mono- and quasi-monoenergetic neutrons. The incident proton energy and the thickness of the lithium target are essential factors to be considered for the quality of neutron spectra. In particular, a continuous neutron spectrum can be produced by means of an "infinite thickness" i.e. a thickness greater than the range of protons in lithium. Thin targets are used for the production of mono- and/or quasi-monoenergetic fast neutrons. Since the ${}^7\text{Be}$ is an unstable nucleus decaying by emission of a 478 keV gamma ray ($\tau = 53\text{d}$), it is possible to accurately measure the number of ${}^7\text{Be}$ nuclei produced. This is in direct relation to the number of neutrons produced by the reaction ${}^7\text{Li}(p,n){}^7\text{Be}$. The polysiloxane neutron scintillator was used for the evaluation of the number of neutron produced.

6.1 The ${}^7\text{Li}(p,n){}^7\text{Be}$ reaction

In this section the physical characteristics of the ${}^7\text{Li}(p,n){}^7\text{Be}$ reaction are pointed out. We employed this reaction as source of quasi-monoenergetic neutrons and neutrons with a continuous spectrum both at the IBA 18/18 medical cyclotron of University of Bern and at the LNS tandem accelerator. In particular the thickness of the lithium and the incident proton energy play a fundamental role on the quality of the neutron spectrum. The ${}^7\text{Li}(p,n){}^7\text{Be}$ reaction ($Q=-1.64$ MeV and energy threshold $E_t=1.88$ MeV) has the property that the number of ${}^7\text{Be}$ nuclei produced is equal to the number of mono-energetic peak neutrons released in the 4π direction (Uwamino et al., 1997). To explain this important property let's first refer to the decay scheme of the ${}^7\text{Be}$ nucleus shown in figure 6.1.

FIGURE 6.1: Decay scheme of the ${}^7\text{Be}$.

The ${}^7\text{Be}$ nucleus decays by electronic capture to the ${}^7\text{Li}$ with half-life of 53 days. In particular, it decays to the ground state of ${}^7\text{Li}$ with a branching ratio of 89.45% and to its first excited state with a branching ratio of 10.44%. The last in turn decays to the ground state of ${}^7\text{Li}$ with emission of a 478 keV gamma ray of half life 73 fs (prompt gamma). Since the number of neutrons produced is equal to the number of ${}^7\text{Be}$ nuclei produced, absolute measurements of neutron flux can be easily carried out with gamma ray spectrometry of the target. For such reasons this reaction fits perfectly the purposes of production of well-characterized fast neutrons. It has to be noticed that this reaction refers to the case that the ${}^7\text{Be}$ is produced in its ground state. Depending on the incident proton energy, the ${}^7\text{Be}$ can be produced also in its excited states. For each excited state there is a corresponding binary reaction ${}^7\text{Li}(p,n){}^7\text{Be}^*$. Table 6.1 shows the excited states up to 20 MeV of the ${}^7\text{Be}$, the spin-parity J^π , the decay time and the energy threshold of the corresponding ${}^7\text{Li}(p,n){}^7\text{Be}^*$.

TABLE 6.1: Energy levels, spin-parity and half-life of the states of the ${}^7\text{Be}$. The fourth column of the table is the energy threshold of the corresponding ${}^7\text{Li}(p,n){}^7\text{Be}^*$ reaction.

Energy level (keV)	J^π	$T_{1/2}$	E_t (MeV)
0	$3/2^-$	53.22 d	1.87
429	$1/2^-$	133 fs	2.37
4570	$7/2^-$	133 fs	7.11
6730	$5/2^-$	-	9.57
7210	$5/2^-$	0.4 MeV	10.12
11010	$3/2^-$	320 keV	14.63

The excited states of the ${}^7\text{Be}^*$ shown in table 6.1 are the ones that can be populated by the ${}^7\text{Li}(p,n){}^7\text{Be}$ channel. If the incident proton energy is high enough to populate the states of table 6.1, the neutron production is not more mono-energetic. For such reasons, the ${}^7\text{Li}(p,n){}^7\text{Be}$ is purely mono-energetic in the proton energy range defined by $E_t=1.88$ MeV and 2.37 MeV (energy threshold of the reaction ${}^7\text{Li}(p,n){}^7\text{Be}^*$,

where ${}^7\text{Be}^*$ refers to the first excited state). In addition, when incident MeV energy protons interact with ${}^7\text{Li}$ other reactions take place. For example, the three-body break-up reaction ${}^7\text{Li}(p,n^3\text{He}){}^4\text{He}$ has relatively high cross-section and low energy threshold ($E_t=3.7$ MeV); the three-body reaction ${}^7\text{Li}(p,n^6\text{Li})p$ has a threshold energy $E_t=8.3$ MeV and the four-body reaction ${}^7\text{Li}(p,n^2\text{Dp})p$ has a threshold energy $E_t=9.9$ MeV. The cross-section of these processes as a function of the proton energy is shown in the plot of figure 6.2.

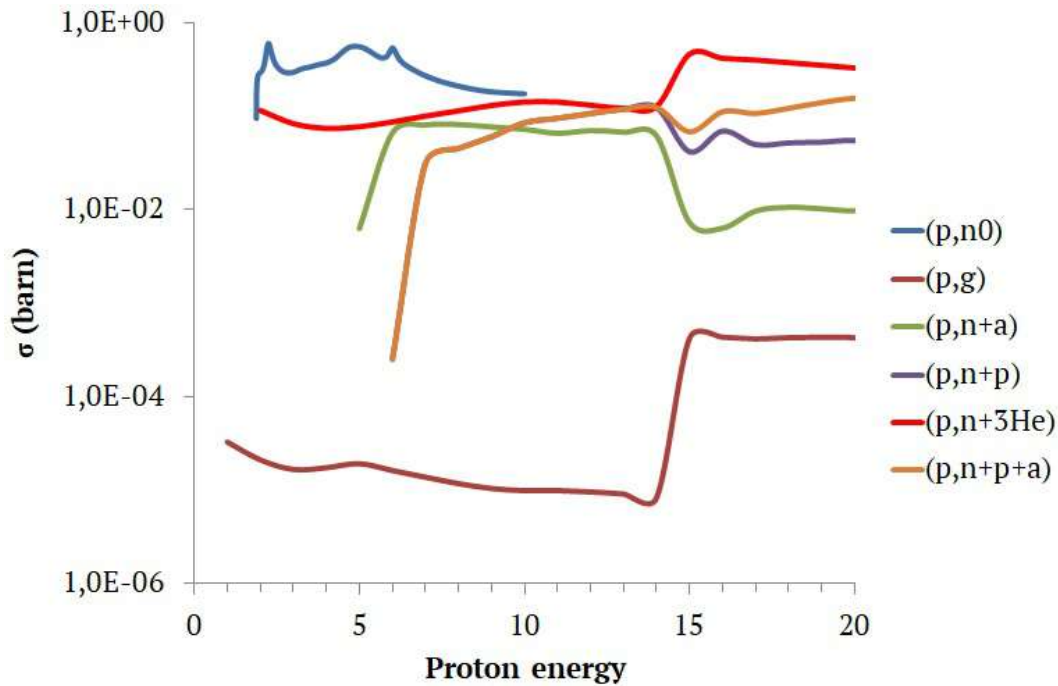


FIGURE 6.2: Cross section as a function of energy of the main nuclear reactions from interaction of MeV energy protons with lithium.

These data are taken from the TENDL2015 and Evaluated Nuclear Data File (ENDF) database (Rochman and Koning, 2012; Tuli, 1996) which include simulated data and previous measurements. The binary reactions result in energy peaks in the neutron spectrum while the non-binary channels result in a continuum at low energies. Finally, another key feature of the ${}^7\text{Li}(p,n){}^7\text{Be}$ reaction is the relatively low gamma production by radiative capture. Figure 6.2 shows that the cross section of proton-induced radiative capture on lithium is lower by more than one order of magnitude compared to the other reactions. Since the neutron scintillators are sensitive both to gamma and neutrons, this aspect is very important to take into account for measurements in mixed n/gamma field.

The simulation of neutron spectra were performed with FLUKA (Böhlen et al., 2014; Ferrari et al., 2005). As an example, figure 6.3 shows the forward (0 degrees) neutron spectrum obtained for interaction of 50 MeV protons on a lithium target of 2 mm.

The peak at 47.4 MeV corresponds to mono-energetic neutrons from the ${}^7\text{Li}(p,n){}^7\text{Be}$ reaction. All the other reactions previously discussed are present in the spectrum of figure 6.3 as continuous at lower energies. Similar spectra were obtained for incident protons of 100, 150 and 200 MeV for which are produced mono-energetic peak neutrons of 98, 147 and 196 MeV respectively.

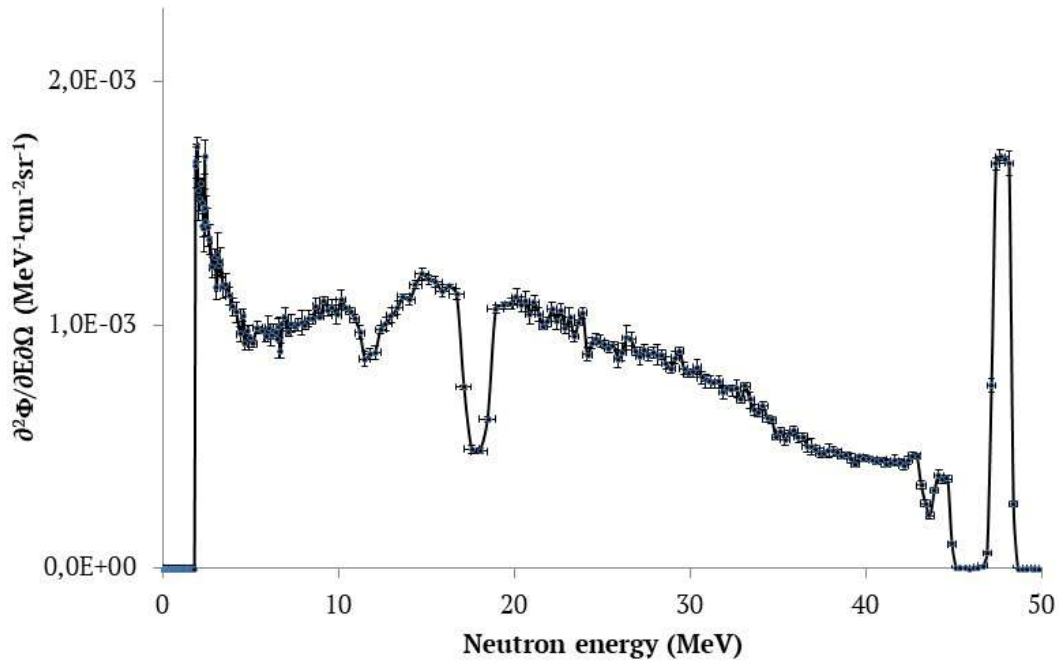


FIGURE 6.3: Simulated neutron spectrum for incident 50 MeV protons on a 2 mm lithium target.

6.2 Neutron production at LNS tandem accelerator

At the LNS tandem accelerator we produced neutron beams with incident protons of energy 20, 10 and 5 MeV. The lithium target, designed and built in collaboration with the LNS mechanical workshop, consisted in a natural lithium (${}^7\text{Li}$: 92.5%; ${}^6\text{Li}$: 7.5%) target of thickness 2 mm. The neutron production due to the component of ${}^6\text{Li}$ is negligible. Since the lithium oxides in air, the target was sandwiched between two $1.5\ \mu\text{m}$ mylar foils. Figure 6.4 shows the experimental setup.

The beam was extracted in air through a $50\ \mu\text{m}$ kapton window. Just before the kapton window a Faraday Cup (FC) provided measurements of proton current. The PS scintillator was placed at 60 cm from the lithium target. This distance was enough to stop 5 and 10 MeV protons. A 1 cm polyethylene slab was used for the run of 20 MeV incident proton energy. An NaI detector was used for measurements of gamma produced. The proton energy on the lithium target were evaluated by subtracting the proton energy loss in kapton, air and mylar. The final energies were 19.2 MeV, 9.0 and 4.4 MeV respectively. Figure 6.5 shows the simulated neutron spectrum and the corresponding measured 2D scatter plot for the three incident proton energies.

During all the acquisitions, the gamma spectrum measured with the NaI detector showed two significant energy peaks: the 478 keV gamma corresponding to the decay of the ground state of ${}^7\text{Be}$ and the 430 keV gamma corresponding to the decay of the first excited state of ${}^7\text{Be}$. Figure 6.6 shows the gamma spectrum measured with the NaI detector.

The number of measured neutrons was evaluated by considering the neutron contribution in the 2D scatter plots. The number of neutrons per incident proton

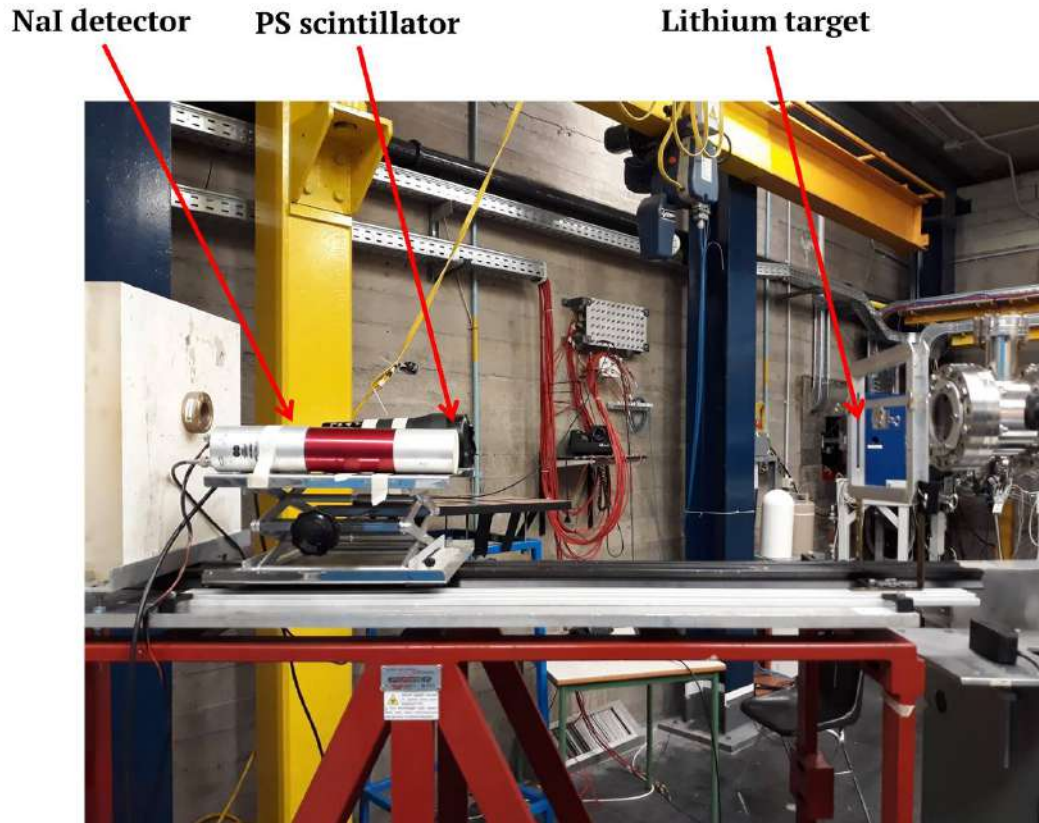


FIGURE 6.4: Experimental setup for neutron production and detection at LNS.

(yield) was compared to the yield calculated by FLUKA simulation for the three acquisition runs at the incident proton energies E_p , current I_p and acquisition time Δt . These results are summarized in table 6.2.

TABLE 6.2: Comparison between the measured and simulated yield for three incident proton energies. The estimation of the PS scintillator efficiency is reported in the last column.

E_p (MeV)	Δt (min)	I_p (pA)	Measured yield	Simulated yield	Efficiency (%)
19.2	6.0	1020	$1.1 \cdot 10^{-7}$	$1.3 \cdot 10^{-6}$	9
9.0	9.0	4750	$1.3 \cdot 10^{-7}$	$6.7 \cdot 10^{-7}$	20
4.4	6.0	240	$5.2 \cdot 10^{-9}$	$1.2 \cdot 10^{-7}$	4

The simulated yield reported in table 6.2 is considered over 4π . In order to have the yield in the PS scintillator such a number was scaled by the ratio of the solid angles. It is noteworthy that the efficiency of the PS was unknown and never measured before. The values of efficiency reported in table 6.2 are the first estimation of the PS efficiency for various energies. These results match with the efficiency values obtained with the AmBe source discussed in section 5.7.

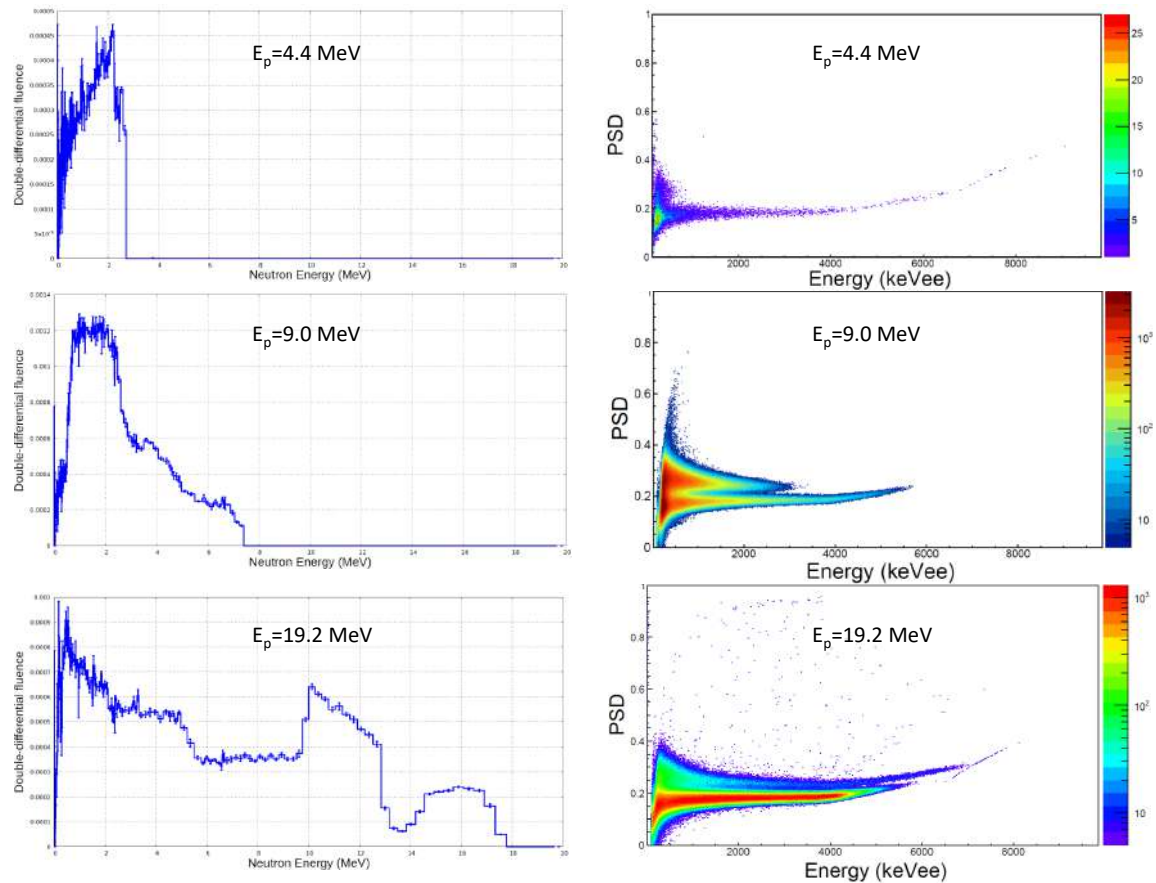


FIGURE 6.5: Simulated neutron spectrum and measured PSD scatter plot for the three runs at the energies (on the target) of 19.2, 9.0 and 4.4 MeV respectively.

6.3 Neutron production at IBA 18/18 medical cyclotron

In the previous section, we described the neutron production at LNS tandem accelerator. Owing to the high proton currents available, cyclotron accelerators such as the IBA 18/18 medical cyclotron of University of Bern, have the advantage of a larger neutron production. In this section, we describe the experiment performed at the Bern cyclotron for the production of a continuous high intensity neutron spectrum based on the ${}^7\text{Li}(p,n){}^7\text{Be}$ reaction. The principal elements of the Bern cyclotron have been discussed in section 2.4. This cyclotron is equipped with an external 6.5 m long beam transport line (BTL) which is dedicated to research activities. A schematic of the cyclotron, the BTL and the devices installed on the BTL for the beam control and transport is shown in figure 6.7. In particular, there are two quadrupole doublets, two beam stoppers, a neutron shutter, a collimator and X/Y steerers. Beam profile measurements are fundamental for research studies as well as for optimizing production yield on beam targets. Beam diagnostics methods at the Bern cyclotron consist in the use of 1) phosphor screens, collimators and beam viewers by which to read the proton current and visualize the beam spot. The beam viewers are copper disks on which a scintillating material is deposited. The beam viewers and phosphor screens are remotely controlled. Finally, a monitor detector (named UniBEaM)

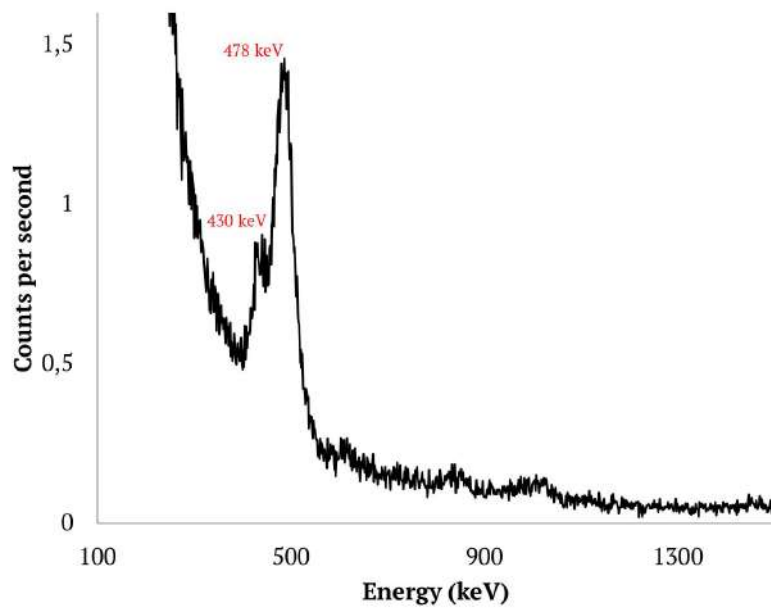


FIGURE 6.6: Gamma spectrum measured with the NaI detector.

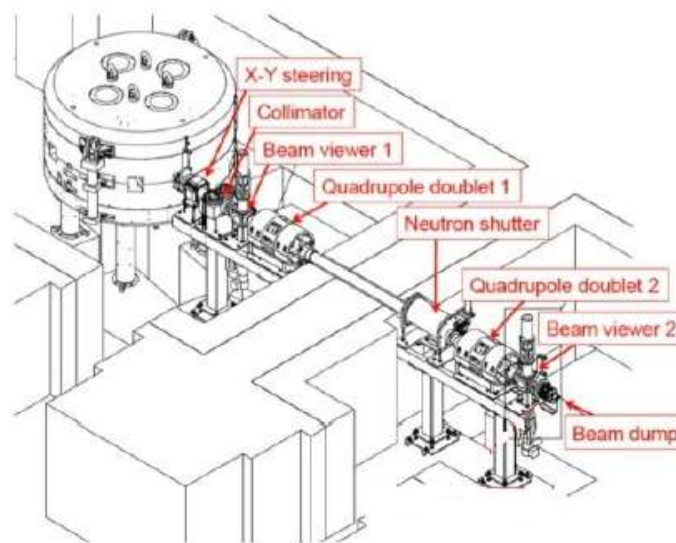


FIGURE 6.7: Schematic of the Bern cyclotron.

designed and constructed by the AEC-LHEP group is available to visualize the two-dimensional beam profile (Nesteruk et al., 2018). These systems are necessary for performing the beam focusing, necessary for ensuring a "clean" neutron production. Neutron beams were produced at the Bern cyclotron with 18.2 MeV protons on a 1 cm natural lithium target. This energy value was obtained by means of suited measurements designed and performed by our research group. In particular, for the first time we carried out a direct measurement of the energy of a medical cyclotron through the *Rutherford Backscattering Spectroscopy* technique (Campajola et al., 2018). The 1 cm thickness lithium target allows the full stopping of the 18.2 MeV protons

in the target. As a result, the spectrum is not mono- and/or quasi-monoenergetic, being a continuous spectrum up to 18.2 MeV. Such a spectrum can be used for the testing of electronic devices, as discussed in section 2.8. Figure 6.8 shows the simulated neutron spectrum obtained for interaction of 18.2 MeV on a 1 cm lithium target.

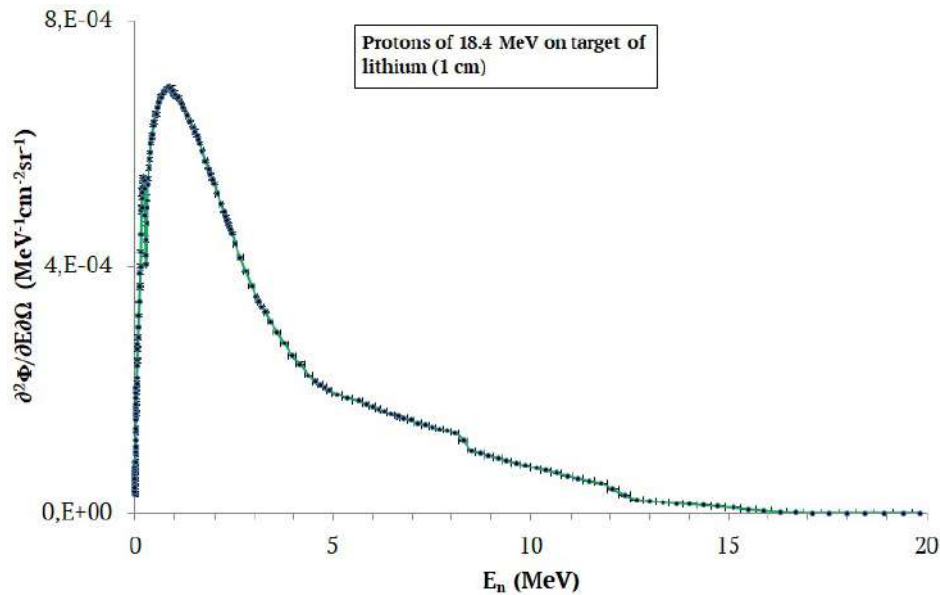


FIGURE 6.8: Simulated neutron spectrum for incident 18.2 MeV protons on a 1 cm lithium target.

This simulation was obtained with FLUKA. Figure 6.9 shows the experimental setup used for neutron production at the Bern cyclotron.

The lithium target was installed in a target-holder movable with a remotely controlled pneumatic actuator. The last was properly designed by us for these measurements and built by the mechanical workshop of University of Bern. Figure 6.10 shows the pneumatic actuator with the lithium target sandwiched between mylar foils necessary for avoiding the oxidation of the lithium in air.

After passing into the quadrupole doublets, the beam was focused thanks to the beam viewers and the UniBeam. The procedure was completed by visualizing the beam with the phosphor screen and by reading the current on a graphite beam dumper. Figure 6.11 shows an image of the output the phosphor screens after the beam focusing.

The PS scintillator was placed at 100 cm from the position of the Li-target. In this experiment the proton current was 100 nA. This value, although higher compared to the currents employed for the experiment at LNS tandem accelerator, can be in principle increased up to 3 order of magnitudes allowing a very intense characterized neutron source. Figure 6.12 shows the PSD 2D scatter plot measured with the PS scintillator for an acquisition of 30 seconds.

The evaluation of neutron produced was performed by means of spectroscopy measurements of the target with an High Purity Germanium (HPGe) detector available at the laboratory of the cyclotron. Figure 6.13 shows the spectrum of the lithium target following the exposure to 18.2 MeV protons.

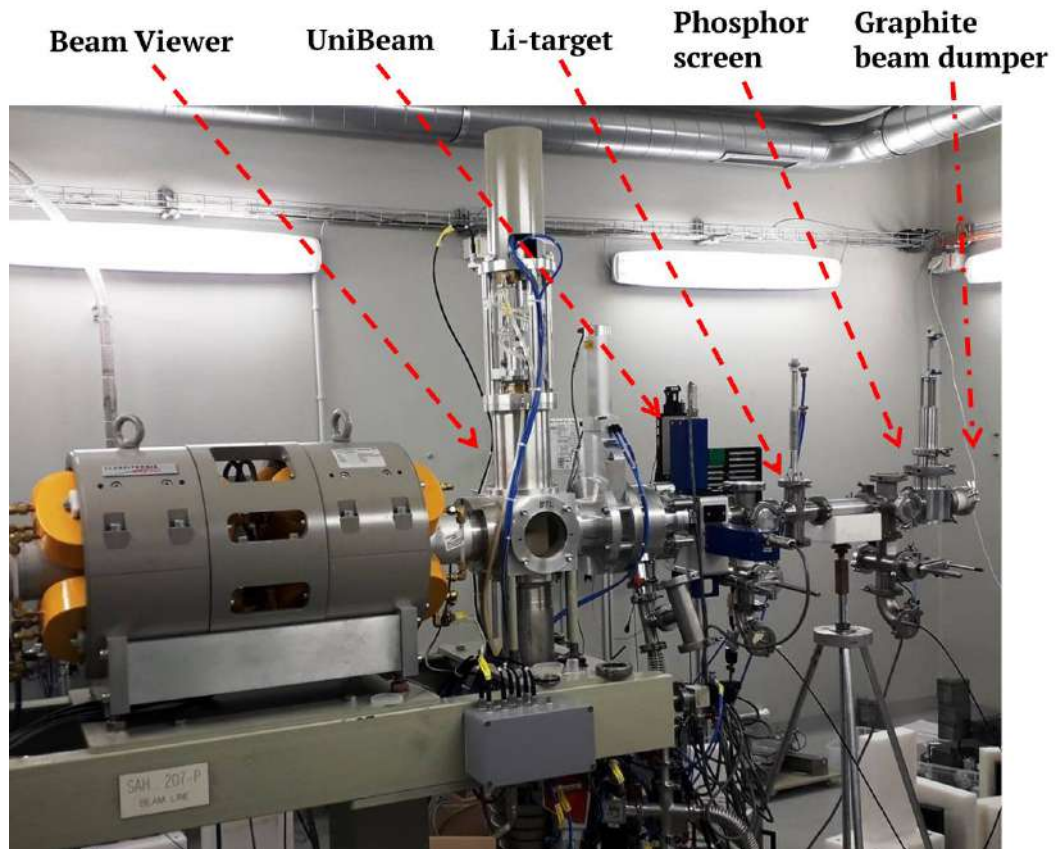


FIGURE 6.9: BTL of the Bern cyclotron for neutron production



FIGURE 6.10: Picture of the pneumatic actuator with the lithium target.

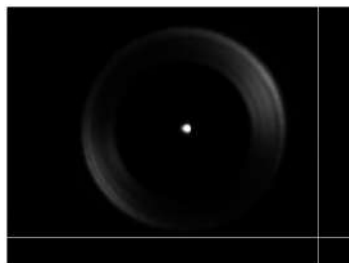


FIGURE 6.11: Image of the proton beam spot with the phosphor screen.

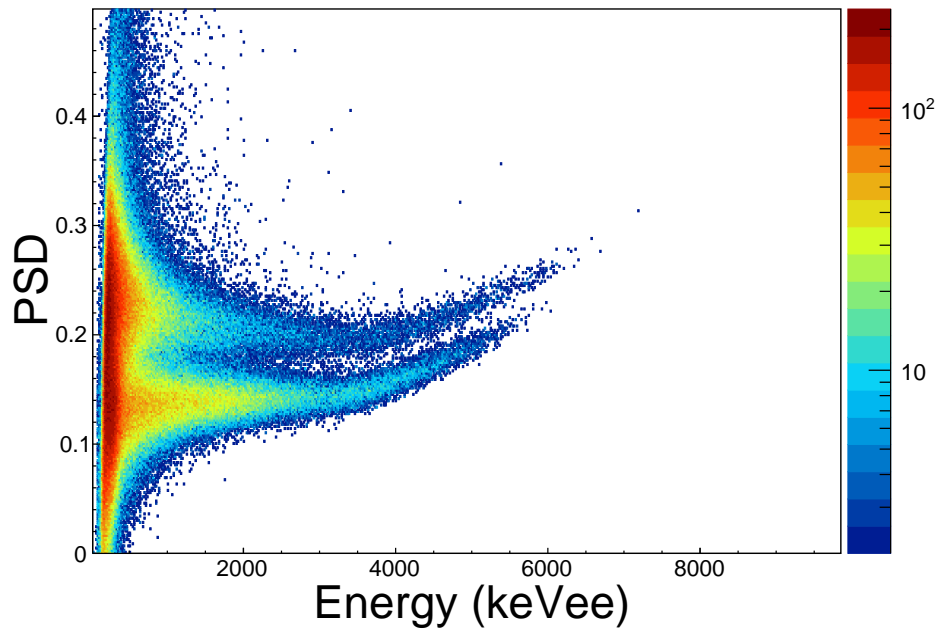


FIGURE 6.12: Measured PSD scatter plot for incident protons of 18.2 MeV on 1 cm lithium target.

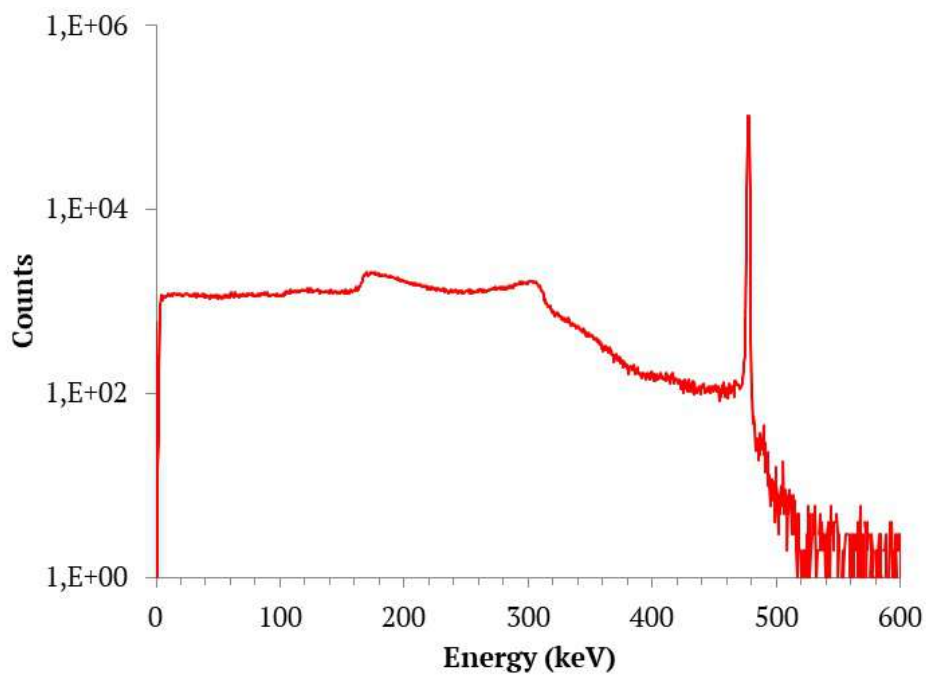


FIGURE 6.13: Spectroscopy measurements of the lithium target following the exposure to 18.2 MeV protons.

The energy peak at 478 keV is the energy corresponding to the decay of the ^7Be . Since the decay has an half-life of 53 days measurements of the number of ^7Be nuclei

was performed for one month following the exposure. In this way it was possible to precisely estimate the contribution to the total number of neutrons due to neutrons produced by the ${}^7\text{Li}(p,n){}^7\text{Be}$ reaction. Figure 6.14 shows the measurements with the HPGe detector.

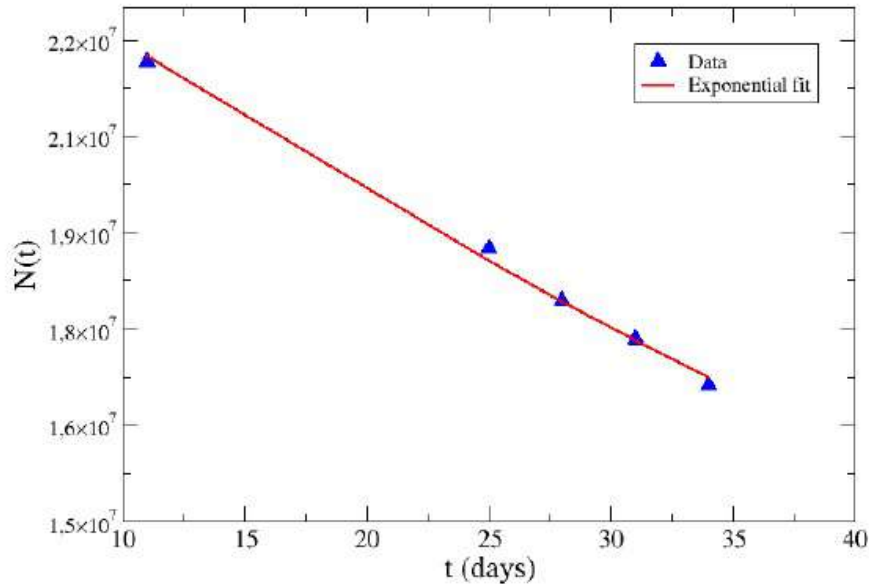


FIGURE 6.14: Measurements (blue triangles) of the activity of the ${}^7\text{Be}$. The red line is the exponential best fit.

The intercept with the y-axis gives the number of neutrons produced just after the irradiation. This number, calculated net to the branching ratio and detector efficiency, was estimated to be $2.0 \cdot 10^7$ neutrons/s for an irradiation of 100 seconds at 100 nA.

Further developments of the implemented neutron beam-line provide the design of a water-cooled target of lithium. This will allow irradiation for a longer time and at higher values of current.

Conclusion

This thesis focuses on development of new radiation detection methods for radiation hardness applications. The radiation tolerance of electronic devices is evaluated at facilities by exposing the device under test to radiation. In order to reproduce the effects of radiation on electronics, the tests at facilities are performed with radiation of different type, dose, energy, fluence etc. Electrons, protons, gamma-rays, heavy ions as well as neutrons are the main types employed for these purposes. On this line, this work proposes several new techniques of radiation detection. In particular, for charged particles, X and gamma radiation the radiochromic film dosimetry, a technique widely employed in medical physics, was found to be suitable for radiation hardness applications. The key features are the wide dynamic range, ease of use and data analysis, high spatial resolution, low dimensions and cost. The study of the response to radiation of interest in radiation hardness (e.g. 250 kV_p X-, ⁶⁰Co gamma- and ⁹⁰Sr/⁹⁰Y beta-rays, 1 MeV electrons and 23, 50 and 200 MeV protons) allowed a deep knowledge of their properties. The response of radiochromic films to these radiation is independent of incident type, energy and dose rate. Moreover, the calibration of the films was done with the law that describe the phenomenon of the kinetics of chemical reactions and more specifically the phenomenon of film darkening. This is an absolute novelty in this field. These new results, published in dedicated papers, presented at several conferences and here in chapter 3 and 4 add an important contribution to such a widespread dosimetry technique. In addition, these results were crucial for the full dosimetry characterization of a ⁹⁰Sr/⁹⁰Y beta source. This source was recently proposed by our group as irradiation source for TID tests as alternative to the well-established ⁶⁰Co source. Finally, on the same topic, the design and development of a new radiochromic film reading method based on opto-electronic instrumentation was carried out. This technique allows real-time dosimetry with radiochromic films, not possible with standard techniques. The validation of this radiochromic film reader (object of a Patent filed in January 2018) is the first step towards the development of miniaturized prototypes addressed to some specific application such as the radiation hardness. Beyond the study of radiochromic film dosimetry, other new radiation techniques for charged particle irradiations were carried on and results presented in this thesis. In particular, a technique designed and set-up by our group has been performed for the first time at tandem accelerator of University of Napoli. This high-precision technique, based on *Rutherford Backscattering Spectroscopy* (RBS) allows real-time monitoring of the fluence on the device under test.

Neutron irradiation are necessary for avionics and terrestrial radiation hardness applications. The development of new techniques for these purposes demands dedicated studies. Firstly, since the difficulties of the interaction of neutrons with matter, their detection is complicated; secondarily, the problem of neutron detection is strictly related to that of neutron production. Owing to the increasing demand in

neutron applications, among which the neutron irradiation of electronics, the set-up of techniques devoted to the exploitation of existing particle beam facilities such as accelerator-based neutron sources is an interesting line to carry on. On this line, a new neutron detector such as the polysiloxane scintillator was used for the characterization of neutron beams produced at tandem accelerator of LNS and at Bern medical cyclotron. The reaction ${}^7\text{Li}(p,n){}^7\text{Be}$ has been employed for fast neutron production as it allows production of purely mono-energetic, quasi-monoenergetic and continuous spectrum beams. The neutron beam line implemented for the first time at the Bern medical cyclotron allows production of characterized neutrons of at least 10^7 fast neutrons per second. Further insights will be devoted to the design of a water cooled lithium target for the set-up of a neutron irradiation beam line.

Bibliography

- Akkerman, A et al. (2001). "Updated NIEL calculations for estimating the damage induced by particles and γ -rays in Si and GaAs". In: *Radiation Physics and Chemistry* 62.4, pp. 301–310.
- Allen, J A Van (1958). "Observation of high intensity radiation by satellites 1958 Alpha and Gamma". In: *Journal of Jet Propulsion* 28.9, pp. 588–592.
- Anders, John et al. (2018). "A facility for radiation hardness studies based on the Bern medical cyclotron". In: *arXiv preprint arXiv:1803.01939*.
- Auger, Martin et al. (2016a). "A detector based on silica fibers for ion beam monitoring in a wide current range". In: *Journal of instrumentation* 11.03, P03027.
- Auger, Martin et al. (2016b). "Accelerator and detector physics at the Bern medical cyclotron and its beam transport line". In: *Nukleonika* 61.1, pp. 11–14.
- Autran, Jean-Luc et al. (2012). "Soft-error rate induced by thermal and low energy neutrons in 40 nm SRAMs". In: *IEEE Transactions on Nuclear Science* 59.6, p. 2658.
- Avila-Rodriguez, MA, JS Wilson, and SA McQuarrie (2009). "The use of radiochromic films to measure and analyze the beam profile of charged particle accelerators". In: *Applied Radiation and Isotopes* 67.11, pp. 2025–2028.
- Bannach, B et al. (1987). "Facility for neutron induced few body reactions at Bochum University". In: *Nuclear Instruments and Methods in Physics Research Section A: Accelerators, Spectrometers, Detectors and Associated Equipment* 254.2, pp. 373–381.
- Barrett, JH et al. (1990). "A high-dose intercomparison study involving red 4034 perspex and FWT-60-00 radiochromic dye films". In: *International Journal of Radiation Applications and Instrumentation. Part C. Radiation Physics and Chemistry* 36.3, pp. 505–507.
- Batchelor, R et al. (1961). "The response of organic scintillators to fast neutrons". In: *Nuclear Instruments and Methods* 13, pp. 70–82.
- Baumann, Robert C and Eric B Smith (2000). "Neutron-induced boron fission as a major source of soft errors in deep submicron SRAM devices". In: *Reliability Physics Symposium, 2000. Proceedings. 38th Annual 2000 IEEE International*. IEEE, pp. 152–157.
- Bazioglou, M and J Kalef-Ezra (2001). "Dosimetry with radiochromic films: a document scanner technique, neutron response, applications". In: *Applied Radiation and Isotopes* 55.3, pp. 339–345.
- Berger, Martin J (1992). "ESTAR, PSTAR, and ASTAR: Computer programs for calculating stopping-power and range tables for electrons, protons, and helium ions". In: *Unknown*.
- Bilge, Hatice et al. (2009). "Surface dose measurements with GafChromic EBT film for 6 and 18 MV photon beams". In: *Physica Medica* 25.2, pp. 101–104.
- Bimbot, R et al. (1978). "Stopping power measurements for 4–5 MeV/nucleon ^{16}O , ^{40}Ar , ^{63}Cu and ^{84}Kr in C, Al, Ni, Ag and Au". In: *Nuclear Instruments and Methods* 153.1, pp. 161–169.

- Böhlen, TT et al. (2014). "The FLUKA code: developments and challenges for high energy and medical applications". In: *Nuclear data sheets* 120, pp. 211–214.
- Braccini, Saverio (2017). "Compact Medical Cyclotrons and their use for Radioisotope Production and Multi-disciplinary Research". In: *Hospital* 200.250, pp. 10–3.
- Brand, K (1995). "The MeV-implantation facility at Bochum". In: *Proc. IIT'94*, pp. 458–461.
- Buenfil, AE et al. (2002). "Response of radiochromic dye films to low energy heavy charged particles". In: *Nuclear Instruments and Methods in Physics Research Section B: Beam Interactions with Materials and Atoms* 197.3-4, pp. 317–322.
- Butson, Martin J, Tsang Cheung, and Peter KN Yu (2004). "Radiochromic film: the new x-ray dosimetry and imaging tool". In: *Australasian Physical & Engineering Science in Medicine* 27.4, pp. 230–230.
- Butson, Martin J et al. (2003). "Radiochromic film for medical radiation dosimetry". In: *Materials Science and Engineering: R: Reports* 41.3-5, pp. 61–120.
- Campajola, L, P Casolaro, and F Di Capua (2017). "Absolute dose calibration of EBT3 Gafchromic films". In: *Journal of Instrumentation* 12.08, P08015.
- Campajola, L et al. (2005). "The 3 MV tandem accelerator of the "Laboratorio dell'Acceleratore" in Naples". In: *Recent Achievements and Perspectives in Nuclear Physics*. World Scientific, pp. 515–520.
- Campajola, L et al. (2018). "Measurement of the proton beam energy of a medical cyclotron based on Rutherford Back-scattering Analysis". In: *Nuclear Inst. and Methods in Physics Research, B*. In press.
- Campajola, Luigi and A Brondi (2013). "The Naples University 3 MV tandem accelerator". In: *AIP Conference Proceedings*. Vol. 1530. 1. AIP, pp. 58–65.
- Campajola, Luigi and Francesco Di Capua (2017). "Applications of Accelerators and Radiation Sources in the Field of Space Research and Industry". In: *Applications of Radiation Chemistry in the Fields of Industry, Biotechnology and Environment*. Springer, pp. 269–297.
- Carturan, S et al. (2010). "Novel polysiloxane-based scintillators for neutron detection". In: *Radiation protection dosimetry* 143.2-4, pp. 471–476.
- Carzaniga, Tommaso Stefano et al. (2017). "Measurement of ^{43}Sc and ^{44}Sc production cross-section with an 18 MeV medical PET cyclotron". In: *Applied radiation and isotopes* 129, pp. 96–102.
- Casolaro, P et al. (2018). "Educational activities with a tandem accelerator". In: *European Journal of Physics* 39.3, p. 035801.
- Castriconi, Roberta et al. (2016). "Dose–response of EBT3 radiochromic films to proton and carbon ion clinical beams". In: *Physics in Medicine & Biology* 62.2, p. 377.
- Cester, D et al. (2014). "Experimental tests of the new plastic scintillator with pulse shape discrimination capabilities EJ-299-33". In: *Nuclear Instruments and Methods in Physics Research Section A: Accelerators, Spectrometers, Detectors and Associated Equipment* 735, pp. 202–206.
- Chadwick, MB et al. (2011). "ENDF/B-VII. 1 nuclear data for science and technology: cross sections, covariances, fission product yields and decay data". In: *Nuclear data sheets* 112.12, pp. 2887–2996.
- Cherubini, R et al. (1988). "Absolute neutron detection efficiency calibration of a stilbene organic scintillator in the energy range 2 to 20 MeV with the associated

- particle technique". In: *Nuclear Instruments and Methods in Physics Research Section A: Accelerators, Spectrometers, Detectors and Associated Equipment* 269.3, pp. 623–633.
- Cirrone, GAP et al. (2006). "The INFN experience in the hadron therapy field". In: *Polish J Environ Stud* 15.4A, pp. 171–3.
- Dale, CJ et al. (1989). "Displacement damage equivalent to dose in silicon devices". In: *Applied Physics Letters* 54.5, pp. 451–453.
- Dalla Palma, M et al. (2015). "Non-toxic liquid scintillators with high light output based on phenyl-substituted siloxanes". In: *Optical Materials* 42, pp. 111–117.
- Daly, EJ et al. (1996). "Problems with models of the radiation belts". In: *IEEE Transactions on Nuclear Science* 43.2, pp. 403–415.
- Davidson, C Donovan, Ewart W Blackmore, and John I Hess (2004). "Failures of MOSFETs in terrestrial power electronics due to single event burnout". In: *Telecommunications Energy Conference, 2004. INTELEC 2004. 26th Annual International*. IEEE, pp. 503–507.
- Devic, Slobodan (2011). "Radiochromic film dosimetry: past, present, and future". In: *Physica medica* 27.3, pp. 122–134.
- Devic, Slobodan, Nada Tomic, and David Lewis (2016). "Reference radiochromic film dosimetry: review of technical aspects". In: *Physica Medica* 32.4, pp. 541–556.
- Di Mascio, Stefano et al. (2018). "Towards defining a simplified procedure for COTS system-on-chip TID testing". In: *Nuclear Engineering and Technology*.
- Drosg, M (1999). "Monoenergetic neutron production by two-body reactions in the energy range from 0.0001 to 500 MeV". In: *An overview. TCM-Meeting of IAEA, Debrecen, Hungary*.
- Durante, Marco and Francis A Cucinotta (2011). "Physical basis of radiation protection in space travel". In: *Reviews of Modern Physics* 83.4, p. 1245.
- Durante, Marco and Harald Paganetti (2016). "Nuclear physics in particle therapy: a review". In: *Reports on Progress in Physics* 79.9, p. 096702.
- Ferrari, Alfredo et al. (2005). *FLUKA: A multi-particle transport code (Program version 2005)*. Tech. rep.
- Fiandra, Christian et al. (2006). "Clinical use of EBT model Gafchromic™ film in radiotherapy". In: *Medical physics* 33.11, pp. 4314–4319.
- Fletcher, Claire Lesley and John A Mills (2008). "An assessment of GafChromic film for measuring 50 kV and 100 kV percentage depth dose curves". In: *Physics in Medicine & Biology* 53.11, N209.
- Flynn, KF et al. (1964). "Pulse height-energy relations for electrons and alpha particles in a liquid scintillator". In: *Nuclear Instruments and Methods* 27.1, pp. 13–17.
- Glaser, Maurice, Federico Ravotti, and Michael Moll (2005). "Dosimetry assessments in the irradiation facilities at the CERN-PS accelerator". In: *Radiation and Its Effects on Components and Systems, 2005. RADECS 2005. 8th European Conference on*. IEEE, PI5–1.
- Hartmann, Frank (2011). "Semiconductor sensors". In: *Nuclear Instruments and Methods in Physics Research Section A: Accelerators, Spectrometers, Detectors and Associated Equipment* 628.1, pp. 40–49.

- Humphreys, J. C. (1989). "NIST high-dose calibration services". In: *Nuclear Instruments and Methods in Physics Research Section B: Beam Interactions with Materials and Atoms* 40, pp. 1173–1177.
- Jaworski, G et al. (2012). "Monte Carlo simulation of a single detector unit for the neutron detector array NEDA". In: *Nuclear Instruments and Methods in Physics Research Section A: Accelerators, Spectrometers, Detectors and Associated Equipment* 673, pp. 64–72.
- Johnston, AH, GM Swift, and BG Rax (1994). "Total dose effects in conventional bipolar transistors and linear integrated circuits". In: *IEEE transactions on nuclear science* 41.6, pp. 2427–2436.
- Jun, Insoo et al. (2003). "Proton nonionizing energy loss (NIEL) for device applications". In: *IEEE Transactions on Nuclear Science* 50.6, pp. 1924–1928.
- Kirby, Daniel et al. (2009). "LET dependence of GafChromic films and an ion chamber in low-energy proton dosimetry". In: *Physics in Medicine & Biology* 55.2, p. 417.
- Knoll, Glenn F (2010). *Radiation detection and measurement*. John Wiley & Sons.
- Lee, Hsien-Che (2005). *Introduction to color imaging science*. Cambridge University Press.
- Leray, JL (2007). "Effects of atmospheric neutrons on devices, at sea level and in avionics embedded systems". In: *Microelectronics Reliability* 47.9-11, pp. 1827–1835.
- Manti, L et al. (2012). "Development of a low-energy particle irradiation facility for the study of the biological effectiveness of the ion track end". In: *Journal of Physics: Conference Series*. Vol. 373. 1. IOP Publishing, p. 012019.
- Martone, M, M Angelone, and M Pillon (1994). "The 14 MeV frascati neutron generator". In: *Journal of nuclear materials* 212, pp. 1661–1664.
- McLaughlin, W. L. and others al (1996). "Novel radiochromic films for clinical dosimetry". In: *Radiation protection dosimetry* 66.1-4, pp. 263–268.
- McLaughlin, W. L. and L. Chalkley (1965). "Measurement of radiation dose distributions with photochromic materials". In: *Radiology* 84.1, pp. 124–125.
- McLaughlin, William L et al. (1996). "Radiochromic solid-state polymerization reaction". In: *ACS Symposium Series*. Vol. 620. American Chemical Society, pp. 151–166.
- McLaughlin, WL et al. (1988). "Radiochromic dosimetry for validation and commissioning of industrial radiation processes". In: *International Journal of Radiation Applications and Instrumentation. Part C. Radiation Physics and Chemistry* 31.4-6, pp. 505–514.
- Menicucci, Alessandra et al. (2018). "Simplified procedures for COTS TID testing: a comparison between 90-Sr and 60-Co". In: *Proceedings NSREC*.
- Micke, Andre, David F Lewis, and Xiang Yu (2011). "Multichannel film dosimetry with nonuniformity correction". In: *Medical physics* 38.5, pp. 2523–2534.
- Mignani, Anna Grazia et al. (1998). "Radiation dosimetry in radiotherapy: a model for an extrinsic optical fiber sensor". In: *European Workshop on Optical Fibre Sensors*. Vol. 3483. International Society for Optics and Photonics, pp. 99–103.
- Morilla, Yolanda et al. (2014). "New gamma-radiation facility for device testing in Spain". In: *Radiation Effects Data Workshop (REDW), 2014 IEEE*. IEEE, pp. 1–5.

- Nesteruk, Konrad Pawel et al. (2018). "A system for online beam emittance measurements and proton beam characterization". In: *Journal of instrumentation* 13.01, P01011.
- Nicholas, Joyce S et al. (1998). "Cosmic radiation and magnetic field exposure to airline flight crews". In: *American journal of industrial medicine* 34.6, pp. 574–580.
- Nolte, Ralf and David J Thomas (2011). "Monoenergetic fast neutron reference fields: II. Field characterization". In: *Metrologia* 48.6, S274.
- Nowicki, Suzanne F, Stephen A Wender, and Michael Mocko (2017). "The Los Alamos Neutron Science Center Spallation Neutron Sources". In: *Physics Procedia* 90, pp. 374–380.
- Palmer, AL, A Nisbet, and DA Bradley (2013a). "Semi-3D dosimetry of high dose rate brachytherapy using a novel Gafchromic EBT3 film-array water phantom". In: *Journal of Physics: Conference Series*. Vol. 444. 1. IOP Publishing, p. 012101.
- Palmer, Antony L, Andrew Nisbet, and David Bradley (2013b). "Verification of high dose rate brachytherapy dose distributions with EBT3 Gafchromic film quality control techniques". In: *Physics in medicine & biology* 58.3, p. 497.
- Palmer, Antony L et al. (2013). "Design and implementation of a film dosimetry audit tool for comparison of planned and delivered dose distributions in high dose rate (HDR) brachytherapy". In: *Physics in Medicine & Biology* 58.19, p. 6623.
- Paul, H and A Schinner (2004). "Does the Result of a Stopping Power Measurement Depend on the Method Used?" In: *Physica Scripta* 69.6, p. C41.
- Paul, Helmut (2010). "Recent results in stopping power for positive ions, and some critical comments". In: *Nuclear Instruments and Methods in Physics Research Section B: Beam Interactions with Materials and Atoms* 268.22, pp. 3421–3425.
- Paul, Helmut and Daniel Sánchez-Parcerisa (2013). "A critical overview of recent stopping power programs for positive ions in solid elements". In: *Nuclear Instruments and Methods in Physics Research Section B: Beam Interactions with Materials and Atoms* 312, pp. 110–117.
- Poivey, Christian and John H Day (2002). "Radiation hardness assurance for space systems". In:
- Poivey, Christian and Gordon Hopkinson (2009). "Displacement damage mechanism and effects". In: *Proc. ESA—EPFL Space Center Workshop*. Vol. 9.
- Poizat, Marc (2009). *Total Ionizing Dose Mechanisms and Effects*. Tech. rep. Technical Report. Space Center EPFL and European Space Agency. http://space.epfl.ch/webdav/site/space/shared/industry_media/03EPFL_TID_Basic-Mech.pdf.
- Quaranta, A et al. (2011). "Doped polysiloxane scintillators for thermal neutrons detection". In: *Journal of Non-Crystalline Solids* 357.8-9, pp. 1921–1925.
- Ranucci, Gioacchino (1995). "An analytical approach to the evaluation of the pulse shape discrimination properties of scintillators". In: *Nuclear Instruments and Methods in Physics Research Section A: Accelerators, Spectrometers, Detectors and Associated Equipment* 354.2-3, pp. 389–399.
- Raulo, A et al. (2012). "Pt-CdTe detectors spectroscopic performances and RBS and XRF interface composition analysis". In: *IEEE Transactions on Nuclear Science* 59.4, p. 1491.
- Reinhardt, S et al. (2015). "SU-E-T-533: LET Dependence Correction of Radiochromic Films for Application in Low Energy Proton Irradiation". In: *Medical physics* 42.6Part20, pp. 3458–3458.

- Rink, Alexandra, I Alex Vitkin, and David A Jaffray (2005). "Suitability of radiochromic medium for real-time optical measurements of ionizing radiation dose". In: *Medical physics* 32.4, pp. 1140–1155.
- Rink, Alexandra et al. (2015). *Fiber optic radiochromic dosimeter probe and method to make the same*. US Patent 9,000,401.
- Rochman, D and AJ Koning (2012). "TENDL-2011: TALYS-based Evaluated Nuclear Data Library". In: *Nuclear Research and Consultancy Group (NRG): Petten, The Netherlands*.
- Sato, Tatsuhiko (2015). "Analytical model for estimating terrestrial cosmic ray fluxes nearly anytime and anywhere in the world: Extension of PARMA/EXPACS". In: *PloS one* 10.12, e0144679.
- Sawyer, Donald M and James I Vette (1976). "AP-8 trapped proton environment for solar maximum and solar minimum". In: *NASA STI/Recon Technical Report N 77*.
- Soares, Christopher G (2006). "Radiochromic film dosimetry". In: *Radiation measurements* 41, S100–S116.
- Sorriaux, Jefferson et al. (2013). "Evaluation of Gafchromic® EBT3 films characteristics in therapy photon, electron and proton beams". In: *Physica Medica* 29.6, pp. 599–606.
- Srour, JR, Cheryl J Marshall, and Paul W Marshall (2003). "Review of displacement damage effects in silicon devices". In: *IEEE Transactions on Nuclear Science* 50.3, pp. 653–670.
- Sturesson, F (2009). "Single event effects (SEE) mechanism and effects". In: *Space Radiation and its Effects on EEE Components* 6.
- Summers, Geoffrey P et al. (1993). "Damage correlations in semiconductors exposed to gamma, electron and proton radiations". In: *IEEE Transactions on Nuclear Science* 40.6, pp. 1372–1379.
- Takaku, D, T Oishi, M Baba, et al. (2011). "Development of neutron-gamma discrimination technique using pattern-recognition method with digital signal processing". In: *Progress in Nuclear Science and Technology* 1, pp. 210–213.
- Tomic, Nada et al. (2014). "Characterization of calibration curves and energy dependence GafChromic™ XR-QA2 model based radiochromic film dosimetry system". In: *Medical physics* 41.6Part1, p. 062105.
- Tuli, Jag K (1996). "Evaluated nuclear structure data file". In: *Nuclear Instruments and Methods in Physics Research Section A: Accelerators, Spectrometers, Detectors and Associated Equipment* 369.2-3, pp. 506–510.
- Uwamino, Yoshitomo et al. (1997). "High-energy p-Li neutron field for activation experiment". In: *Nuclear Instruments and Methods in Physics Research Section A: Accelerators, Spectrometers, Detectors and Associated Equipment* 389.3, pp. 463–473.
- Vardaci, E et al. (2016). "PRIN-A Facility for neutron production using Accelerator". In: *DAE Symp. Nucl. Phys.* Vol. 61, pp. 952–953.
- Vasilescu, Angela and Gunnar Lindström (2000). "Notes on the fluence normalisation based on the NIEL scaling hypothesis". In: *ROSE/TN* 2.
- Vatnitsky, Stanislav M (1997). "Radiochromic film dosimetry for clinical proton beams". In: *Applied radiation and isotopes* 48.5, pp. 643–651.
- Vette, James I (1991). "The AE-8 trapped electron model environment". In:

- Wegner, G (1972). "Topochemical polymerization of monomers with conjugated triple bonds". In: *Die Makromolekulare Chemie: Macromolecular Chemistry and Physics* 154.1, pp. 35–48.
- Weller, Robert A et al. (2010). "Monte Carlo simulation of single event effects". In: *IEEE Transactions on Nuclear Science* 57.4, pp. 1726–1746.
- Wie, Brian S et al. (2015). "Evaluation and Application of US Medical Proton Facilities for Single Event Effects Test". In: *IEEE Transactions on Nuclear Science* 62.6, pp. 2490–2497.
- Williams, M. and P. Metcalfe (2011). "Radiochromic film dosimetry and its applications in radiotherapy". In: *AIP Conference Proceedings*. Vol. 1345. 1. AIP, pp. 75–99.
- Wolski, D et al. (1995). "Comparison of n- γ discrimination by zero-crossing and digital charge comparison methods". In: *Nuclear Instruments and Methods in Physics Research Section A: Accelerators, Spectrometers, Detectors and Associated Equipment* 360.3, pp. 584–592.
- Xapsos, MA et al. (2000). "Probability model for cumulative solar proton event fluences". In: *IEEE Transactions on Nuclear Science* 47.3, pp. 486–490.
- Xapsos, Michael (2018). "A Brief History of Space Climatology: From the Big Bang to the Present". In:
- Zaitseva, Natalia et al. (2011). "Pulse shape discrimination in impure and mixed single-crystal organic scintillators". In: *IEEE Transactions on Nuclear Science* 58.6, pp. 3411–3420.
- Ziegler, James F, Matthias D Ziegler, and Jochen P Biersack (2010). "SRIM—The stopping and range of ions in matter (2010)". In: *Nuclear Instruments and Methods in Physics Research Section B: Beam Interactions with Materials and Atoms* 268.11-12, pp. 1818–1823.